DESIGN, FABRICATION AND CHARACTERIZATION OF GUIDED-MODE

RESONANCE TRANSMISSION FILTERS

by

MOHAMMAD SHYIQ AMIN

Presented to the Faculty of the Graduate School of

The University of Texas at Arlington in Partial Fulfillment

of the Requirements

for the Degree of

DOCTOR OF PHILOSOPHY

THE UNIVERSITY OF TEXAS AT ARLINGTON

April 2014

Acknowledgements

I wish to express my utmost gratitude to the almighty Allah (swt.) for everything and I am highly indebted to my supervisor Dr. Robert Magnusson for giving me this opportunity and his constant guidance and supervision during my doctoral program. I would also like to thank my graduate committee members Dr. Kambiz Alavi, Dr. Weidong Zhou and Dr. Michael Vasilyev. I especially thank Dr. Jae Woong Yoon and Dr. Nader Hozhabri for giving me their valuable suggestions, time and motivation.

My thanks and appreciations also go to all my colleagues in developing the projects and people who have willingly helped me out with their abilities and valuable discussion.

I also thank Kristin Bergfield for her continuous help and support. I would like to acknowledge the financial support by my supervisor's funding agencies and department of electrical engineering.

Finally, I would like to express my warmest appreciation to my parents, my wife and my son for their support and understanding during the pursuit of this doctoral program.

April 16, 2014

Abstract

DESIGN, FABRICATION AND CHARACTERIZATION OF GUIDED-MODE

RESONANCE TRANSMISSION FILTERS

Mohammad Shyiq Amin, PhD

The University of Texas at Arlington, 2014

Supervising Professor: Robert Magnusson

This dissertation addresses photonic devices enabled by the guided-mode resonance (GMR) effect. As periodic phototonic structures can become highly reflective or transmissive at resonance, this effect has been utilized to design suites of optical elements including reflection filters, transmission filters, broadband mirrors, polarizers, and absorbers with a plethora of possible deployment venues. Even though there has been considerable research on the reflection type GMR elements, attendant transmission filters have less explored experimentally, as there is material limitation to design this kind of filters with simple architecture and they also may require coupling to multiple resonances simultaneously. Apart from the design issues, experimental realization of these filters is challenging. There have not been any experimental reports on optical transmission filters with narrow transmission band and high efficiency and well defined low sidebands. In this Dissertation, we design, fabricate and characterize narrow band guided-mode resonance transmission filters.

Initially we study a way to engineer the optical constants of amorphous silicon (a-Si) suitable for different applications. Rapid thermal annealing is applied to induce crystallization of sputtered amorphous silicon deposited on thermally grown oxide layers. The influence of annealing temperatures in the range of 600°C–980°C is systematically

investigated. Using scanning-electron microscopy, ellipsometry and x-ray diffraction techniques, the structural and optical properties of the films are determined. An order-of-magnitude reduction of the extinction coefficient is achieved. We show that the optical constants can be tuned for different design requirements by controlling the process parameters. For example, we obtain a refractive index of ~3.66 and an extinction coefficient of ~0.0012 at the 1550-nm wavelength as suitable for GMR transmission filter applications where a high refractive index and low extinction coefficient is desired.

We design transmission filters for both transverse electric (TE) and transverse magnetic (TM) polarizations and experimentally demonstrate a simple and geometrically tunable narrowband transmission filter for TM polarization using a one-dimensional silicon grating. We interpret the response in terms of symmetry of the guided modes in a dielectric slab waveguide, with numerical analysis and experimental results. The filter exhibits a 50-nm wide transmission peak with 60% efficiency at off-normal incidence in the telecommunication wavelength region. We can achieve higher efficiency with broader linewidths from larger incidence angles. We also explain the challenges that the experimental realization of these devices entail such as susceptibility to extinction coefficient, mode confinement, and surface irregularities.

Moreover, we provide a new principle for optical transmission filters based on the GMR effect cooperating with the Rayleigh anomaly in a subwavelength nanograting. We theoretically and experimentally show that the onset of higher diffraction orders at the Rayleigh anomaly can dramatically sharpen a GMR transmission peak in both spectral and angular domains. There results a unique transmission spectrum that is tightly delimited in angle and wavelength as demonstrated with a precisely fabricated device.

Finally, we report experimental research on GMR transmission filters based on a Fabry-Perot cavity. We achieve a resonance linewidth of close to 3 nm

with attendant free spectral range (FSR) of 7 nm. Even though the efficiency of the resonance peak is not high, we can improve the results by applying low-loss materials and generate broad low sidebands by decreasing the cavity length with a micro-control translation stage.

Table of Contents

List of Illustrations

List of Tables

Chapter 1

Introduction

1.1 Introduction and Background

Rapid spectral variations associated with zero-order dielectric waveguide gratings, also known as guided-mode resonance (GMR) effects, have become increasingly appealing due to their diverse spectral properties enabling such as reflection filters[1,2,3,4,5], transmission filter [6,7,8,9], polarizers [10], sensors [11], display elements such as color filters [7], dispersive elements [12] like buffers, delay lines and myriads of other applications. GMRs are a category of diffraction grating resonances referred as grating anomalies. Diffraction grating resonance has undergone a rich history of study since its discovery in 1902, when Robert Wood reported abrupt discontinuities in the reflectivity spectra of metallic diffraction gratings but could not explain it using the scalar diffraction theory. [13,14,15]. These "Wood's anomalies" were first theoretically explained by Lord Rayleigh [16], until it was finally pointed out as one of two main types of dielectric grating anomalies: Rayleigh anomaly which is the classical Wood's anomaly and resonance anomaly by Hessel and Oliner in 1965 [17, 18]. The Wood's anomaly is a salient feature that manifests on periodic surfaces illuminated by incident electromagnetic waves. It refers to the rapid energy redistribution of diffraction orders alternating from evanescent to propagating waves or vice versa and a resonance type anomaly, which is caused by the guided mode allowed in the grating or at its interface [16,17].

Theoretical and experimental research on these kinds of resonance structures has peaked since 1980s especially after the implementation of Rigorous coupled wave analysis (RCWA) by Moharam and Gaylord [19]. Resonance on surface relief grating

1

couplers has been analyzed by Neviere *et al.* [20]. Zhang and Tamir presented the effect of Wood's anomaly with diffracted Gaussian beam on reflective period structure using Hessel-Oliner theory [21]. There has numerous other early theoretical research on transmission gratings with square wave profile [22,23], anisotropic gratings [24], reflection gratings in high power applications [25] etc. Wang and Magnusson described an estimation formula to locate the guided-mode resonances using waveguide equations for weakly modulated diffraction gratings [1]. In this method, the prediction of the GMR location is only accurate for the small modulation strength of the structure. Rosenblatt *et al*. provided a simplified ray model to derive a formula for diffraction efficiency [26].

With the advent of fast computational analysis tools, along came the interest for different potential application of these kinds of resonance structures. Gale *et al.* first proposed to use GMR structures in security application [27].Magnusson *et al.* demonstrated different applications of GMR devices such as reflection and transmission filters [1-3,6-9], polarizers[10,28], biosensors [11],laser mirrors [29] etc. Recently a lot of other application such as MEMS tunable filters [30], Rayleigh anomaly enabled transmission filters [31], photovoltaic application [32], color filter arrays [33] etc. have been reported by the nanophotonics devices group led by Magnusson.

Even though, most theoretical and experimental research has been reported on GMR filters operating in reflection regime, not much exploration has been done on the experimental analysis of narrow band GMR transmission filter. Transmission, or bandpass, GMR filters were first presented in 1995 and were designed with multilayer structures [11]. Tibuleac *et al.* provided numerical transmission filter designs in the optical region and experimentally verified their performance in the microwave region [8,9]. Kanamori *et al.* reported transmission color filters with broad bandwidths [7]. Key attributes of high-performance GMR transmission filters include a narrow transmission

peak, high efficiency, and low sidebands, which are otherwise difficult to obtain using the GMR effect. Also an issue related to the design and the fabrication of single layer grating narrow band transmission filters in the communication band is that, it is difficult to have low sidebands with high transmission efficiency [34].

1.2 Overview of the Dissertation

In this dissertation, we develop a theoretical and experimental analysis of narrow band guided-mode resonance (GMR) transmission filter with high transmission efficiency and flat low-transmission sidebands.

Chapter 2 discusses about the basic theoretical analysis and design optimization of guided mode resonance filters. We show the effects of variation in structural and optical parameters such as grating period, thickness, fill factor , extinction coefficient etc. we provided 2D maps of these variation and it's relation to the diffraction efficiency.

Chapter 3 addresses a technique to engineer the optical constants of sputtered amorphous silicon films by crystallization with rapid thermal annealing which can counter the effect of extinction coefficient in realizing transmission filters. Rapid thermal annealing is applied to induce crystallization of sputtered amorphous silicon deposited on thermally-grown oxide layers. The influence of annealing temperatures in the range of 600°C-980°C is systematically investigated. Using scanning-electron microscopy, ellipsometry and x-ray diffraction techniques, the structural and optical properties of the films are determined. An order-of-magnitude reduction of the extinction coefficient is achieved. We show that the optical constants can be tuned for different design requirements by controlling the process parameters. For example, we obtain a refractive index of ~3.66 and an extinction coefficient of ~0.0012 at the 1550-nm wavelength as suitable for a

particular optical filter application where a high refractive index and low extinction coefficient is desired.

In chapter 4 we delve more into the details of the design, optimization, fabrication and the challenges of GMR transmission filters. We present filters for both TE and TM polarization operated at non-normal incidence where we show TE design is more susceptible to extinction coefficient and mode confinement. We also provide a design for a transmission filter operated at normal incidence enabled by the symmetric mode.

Chapter 5 presents a new principle for optical transmission filters based on the guided-mode resonance (GMR) effect cooperating with the Rayleigh anomaly in a subwavelength nanograting. We theoretically and experimentally show that the onset of higher diffraction orders at the Rayleigh anomaly can dramatically sharpen a GMR transmission peak in both spectral and angular domains. There results a unique transmission spectrum that is tightly delimited in angle and wavelength as demonstrated with a precisely fabricated device.

Chapter 6 investigates the design, fabricate and characterization of transmission filters based on wideband guided-mode resonance (GMR) reflectors acting as Fabry-Perot cavity.

Finally in chapter 7 the potential future research direction is discussed.

Chapter 2 Theoretical Background of Guided-Mode Resonance Filters

2.1 Basic Theory

A GMR element typically consists of a subwavelength periodic grating and/or a waveguide over a substrate as shown in Figure 2-1 with period Λ, grating depth d_g, fill factor F which is defined as the fraction of the period containing the high refractive index material, incident beam I, reflected beam R, and transmitted beam T. The grating layer consists of a high-index material n_H and a low-index material n_L, n_C and n_S are the refractive index of cover (medium containing the incident and the reflected waves) and substrate (medium containing the transmitted waves) respectively. The modulation of the grating is calculated by the change of the refractive index within a grating period as, $\Delta n = n_H - n_L$. The grating layer can also act as the coupling as well as waveguide layer. For the grating structure to work as a waveguide, its average refractive index, n_{avg} has to be greater than that of the cover and substrate. The average refractive index can be expressed as

$$n_{avg} = \sqrt{n_L^2 + f(n_H^2 - n_L^2)} \tag{2.1}$$
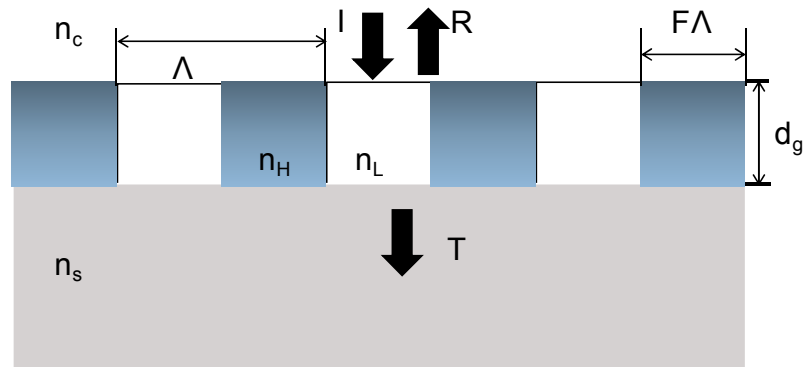
Figure 2-1 Single layer GMR structure with period Λ, grating thickness d_g, Fill Factor F, refractive index of the cover and substrate is n_C and n_S respectively.

For TE polarization (Electric field vector normal to the plane of incidence), the coupled wave equations conducting the wave propagation in the waveguide grating can be expressed [1,19,35,36] as

$$\frac{d^2 E_i(z)}{dz^2} + \left[k^2 n_{avg}^2 - k^2(n_{avg} sin\theta - i\frac{\lambda}{\Lambda})^2\right] E_i(z) + \frac{1}{2} k_0^2 \Delta n^2 [E_{i+1}(z) + E_{i-1}(z)] = 0$$

(2.2)

where, E_i (z) is the y-component of the electric field amplitude of the i-th space harmonic, k=$2\pi/\lambda$, λ is the free space wavelength, θ is the incident angle, Δn is the modulation of index. With Δn close to zero, this equation approaches to the case of an unmodulated dielectric waveguide simplified as

$$\frac{d^2 E_i(z)}{dz^2} + \left[k^2 n_{avg}^2 - \beta^2\right] E_i(z) = 0$$

(2.3)

where, β is the propagation constant. The condition for the guided wave to exist in the grating structure can be represented [1] as

$$max\ (n_C, n_S) \leq n_{avg} sin\theta - i\frac{\lambda}{\Lambda} < n_{avg}$$

(2.5)

So by making Δn very small we can estimate the propagation constant of the waveguide grating as

$$\beta \rightarrow \beta_i = k(n_{avg} sin\theta - i\frac{\lambda}{\Lambda})$$

(2.4)

For a typical single layer zero order grating ($\Lambda < \lambda$), at specific wavelengths, incident angles or polarization, the diffracted light gets coupled with the waveguide modes supported by the structure. Due the periodic modulation, the structure becomes leaky [34] and re-radiate the waves to the cover and the substrate. These reradiated waves make interference with the directly reflected and transmitted waves and can have a complete energy transfer towards the reflection side or transmission side depending on the parameters. Reflection data for these guided-mode resonances typically show a asymmetric line shape consisting a high peak associated with the high reflection followed

6

by a dip associated with the transmission peak. By selecting proper parameters and/or incorporating multilayer thin films, we can select the position of the reflection or transmission peak with high efficiency and low sidebands [34]. Depending on the device parameters, wavelength, incident angle designed by RCWA methods, the spectral bands of these resonant leaky-mode elements can be engineered for various photonic device applications.

Figure 2-2(a) presents the schematic diagram of a partially etched Si grating GMR device for TE polarization. Figure 2-2(b) shows spectral response of the GMR structure along with the spectrum for unpatterned case calculated with effective medium theory.
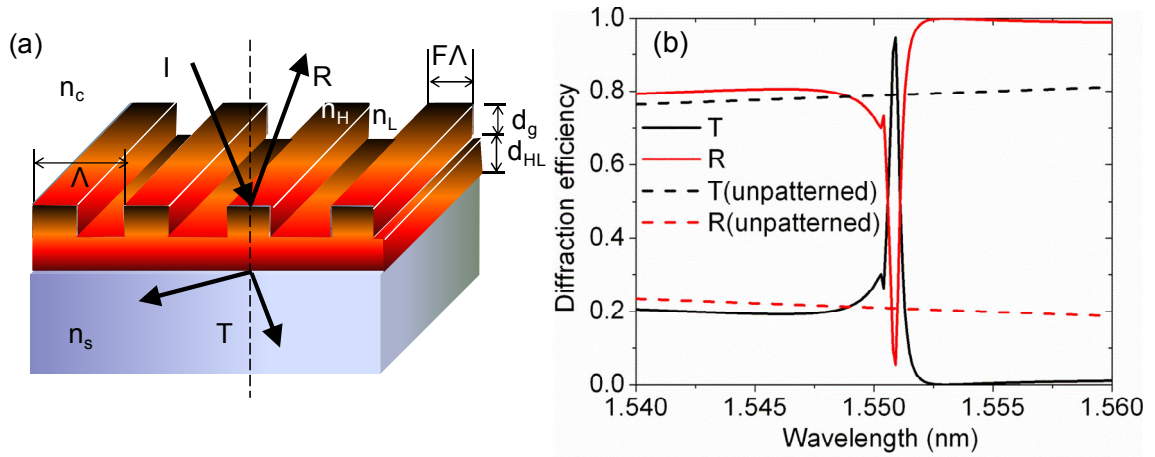
Figure 2-2 (a) Schematic view of a generic GMR element and (b) Spectral response. Parameters period Λ = 1020 nm, grating layer thickness d_g=280 nm, Fill Factor F = 0.31, homogeneous Si layer thickness d_{HL}=290 nm, normal incidence, TE polarization.

Exact spectral response and the designs of these kinds of structures are calculated using RCWA method but this numerical method does not provide any analytical solution for the diffraction efficiency hence does not offer detailed information about the physical phenomena happening inside the structure.

7

2.2 Effects of Variation in Structural Parameters
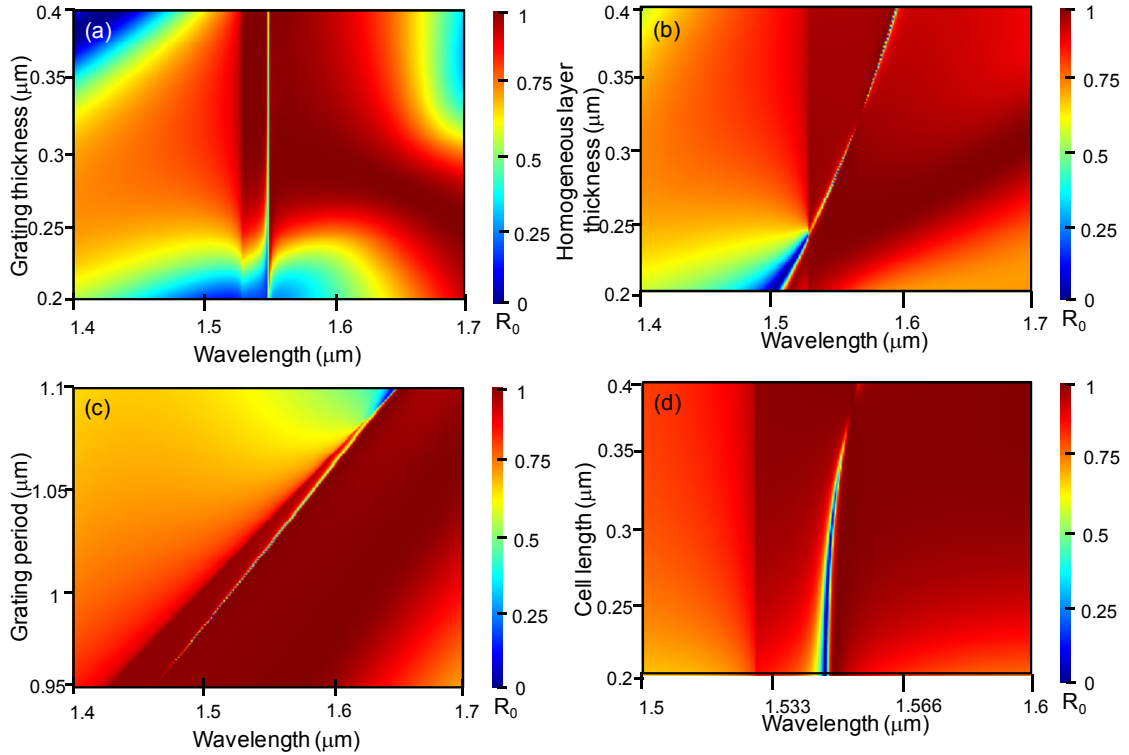
Figure 2-3 Effects of variation in structural parameters (a) variation in grating thickness, (b) variation in homogeneous layer thickness, (c) variation in grating period, (d) variation in the cell length (grating fill factor).Parameters shown in Figure 2-2.

We can design guided-mode resonance (GMR) transmission filters for both transverse magnetic (TM) and transverse electric (TE) polarization by using an inverse numerical technique known as particle swarm optimization (PSO) [37]. We use rigorous coupled-wave analysis (RCWA) [38] for numerical evaluation of GMR filter performance in our PSO code. Also to compute the field excitation and the effects of extinction coefficienct, we use MCgrating and our own software RMsolver. These guided-mode

resonance devices highly depends on the variation in the structural parameters such as grating thicknesses, period, fill factor etc. Figures 2-3 shows the effect of variation in the structural parameters for the device shown in figure 2-2.

From the Figure 2-3 (a) we see that for the grating thickness of 250 or lower, the spectrum follows an asymmetric fano profile but as the thickness is increased the line shape resembles a symmetric lorentzian profile. Also we find that for this device, the narrow transmission peak position does not shift much with the change in the grating depth but the change in the homogeneous layer and period affects the resonance efficiency and position significantly. With only 3% fabrication error in these parameters, efficiency can drop from 100% to 30% or even lower. Figure 2-3(b) illustrates some interesting spectral behavior before and after the Rayleigh wavelength for the homogeneous layer thickness of around 280 nm and it also shows the possibility of ultra narrow resonance spectra for thickness of around 330 nm. Cell length beyond 350 nm can also lower the reflection efficiency significantly. From the 2-D contour maps we can show the possibility of different research interest with these kinds of GMR devices

2.3 Effect of Extinction Coefficient and Surface Roughness

Optical properties naming the refractive index and the extinction coefficient strongly affect the diffraction efficiency of the narrow band resonances especially the transmission resonance. Figure 2-4 depict the effect of the extinction coefficient on the transmission efficiency for the device mentioned in Figure 2-2(a). We see that by having material loss due to absorption or surface roughness, the transmission efficiency can be significantly affected for a narrow band resonance. So it is very important to have low loss material for achieving high efficiency narrow band resonances.
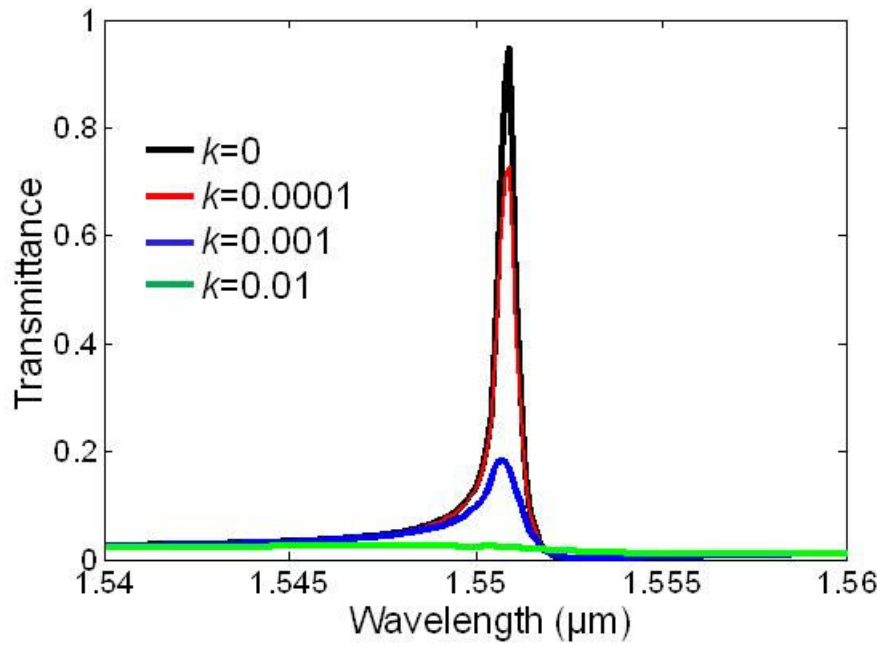
Figure 2-4 Effect of variation in extinction coefficient

Later we discuss a technique to engineer the optical constants of sputtered amorphous silicon films by crystallization with rapid thermal annealing which can counter the effect of extinction coefficient on narrow band resonance.

Chapter 3

Engineering the Optical Constants of Sputtered Amorphous Silicon Films by

Crystallization with Rapid Thermal Annealing

3.1 Introduction

Polycrystalline silicon (poly-Si) has been widely investigated for use in thin-film transistors, solar cells, and various optical and thermal devices [39,40,41,42]. The performance of these devices relies on material qualities such as grain size, in-grain defect densities, level of surface roughness, and porosity of the film. Solid-phase crystallization (SPC) of amorphous Si (a-Si) upon low-pressure chemical vapor deposition (LPCVD) is a common method for growing poly-Si due to its simplicity and low cost as well as its capability to produce uniform and smooth surfaces with high reproducibility [43,44,45]. The SPC process, however, has limitations as it requires a long annealing time of ~20–60 hours to transform to the polycrystalline phase with a large grain size and the attendant formation of in-grain defects [46,47,48,49]. As an alternative method, rapid thermal annealing (RTA) can be used for the crystallization of a-Si; the results are similar to those obtained by furnace annealing [50,51,52]. The particular heat treatment used affects the optical constants of the deposited material. Even though the crystallographic changes effected upon annealing of the Si films using chemical vapor deposition (CVD) techniques such as LPCVD and plasma-enhanced CVD have been widely studied, the influence of RTA with sputtered a-Si samples on the optical constants, i.e., the refractive index and especially the extinction coefficient of the film, has received less attention. Accordingly, in this study we present an alternative technique applying direct sputtering and RTA to obtain thin a-Si films with favorable optical properties.

To provide context, we note that Modreanu *et al.* reported microstructures and refractive indices of as-deposited LPCVD Si films applying temperatures up to 650°C [53]. Lioudakis *et al.* presented parametric analysis of ellipsometric angles (Ψ and Δ) of ion-implanted polycrystalline Si films annealed at various temperatures [54]. In the present work, we study the deposition and crystallization of a-Si thin films grown using sputtering and subsequent RTA. We explore the changes in the optical constants, i.e., the refractive index, n, and the extinction coefficient, k, as functions of annealing temperature and time. We report a significant order-of-magnitude improvement of the extinction coefficient relative to the as-deposited film. Our aim is to develop a method to produce high-quality a-Si film with a high refractive index and low loss for applications in photonics and optoelectronic devices. Therefore, we provide herein a systematic way to tune the optical constants according to different criteria.

3.2 Experimental Details

All experiments were completed with 4-inch n-type Si (100) substrates. First we deposit a-Si on a (100) Si substrate then measure the n, k and d to have a base record. Then we apply annealing and measure the samples again to report the changes on the surface, crystal and optical properties of the film. The experimental steps can be summarized by the Figure 3-1.
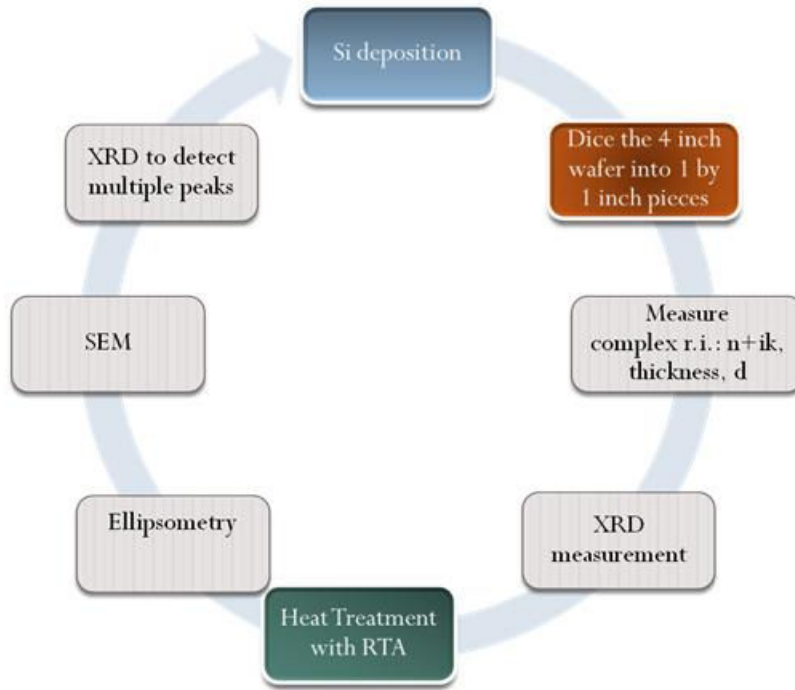
Figure 3-1 Basic experimental steps

Upon annealing, the crystalline grain growth of a-Si depends on the as-deposited films. Hence, we performed numerous depositions under different sputter conditions set by the deposition parameters. The optimized process parameters are presented in Table 3-1.

Table 3-1 Process parameters for a-Si deposition by sputter.

Parameters	Strike	Pre-sputter	Sputter
Pressure (mTorr)	35	5	5
Gas Flow (SCCM)	30	30	30
Power (W)	60	150	150
Time (s)	60	120	18000

Prior to a-Si deposition, the wafer went through a wet cleaning process; then a spin-rinse dryer removed the water from its surface. Wet thermal oxidation was conducted in a Tystar oxidation furnace for 600 seconds at 1100°C yielding a layer of SiO_2 with a thickness of ~360 nm. Then we used an AJA ATC Orion Series UHV Sputtering System to deposit a ~1034-nm thick a-Si film on that 4-inch oxidized Si wafer, with a deposition rate of 2.65 nm / min. We performed a-Si depositions by sputtering at chamber pressures of 10 mTorr, 7 mTorr, and 5 mTorr and used a Woollam VAS ellipsometer with a 75 W light source including a high speed monochromator system to measure the refractive index of each film obtaining n ~3.09, ~3.481, and ~3.71, respectively, at the 1550-nm wavelength. The main chamber was pumped down to the base vacuum of ~8 ×10^{-8} Torr, applying no substrate heating. The correlation between the lower pressure as well as the lower deposition rate of the a-Si film and the increase in refractive indices indicates denser a-Si films [53]. For pressures lower than 5 mTorr, the refractive index is found to decrease again. This data suggests that the near-optimum process condition is at 5 mTorr with an Argon gas flow of 30 SCCM and a power of 150 W. We conducted nine-point ellipsometry measurements of the films to establish consistency in thickness d, n, and k, where n+ik denotes the complex index of refraction. A standard ellipsometric measurement technique is used to extract n, k, and d for our films. We use a function-based model layer (Cauchy layer) expressing n by a slowly varying polynomial function of wavelength as $n(\lambda)=A+B/\lambda^2+ C/\lambda^4$ and k as an exponential absorption tail as $k(\lambda)=\alpha e^{\beta(12400(1/\lambda-1/\gamma))}$ [55, 56, 57]. In the dispersion model, the six fitting parameters are weights A, B, and C; the extinction coefficient amplitude α; the exponent factor β; and the band edge γ. Our ellipsometer applies the Levenberg-Marquardt multivariate regression algorithm for data fitting whereby the optical constants and

thickness are determined. Figure 3-2 illustrates the results on a wafer map. The data set was taken from the center of the wafer in 10 mm increments.

d:365.2nm
n:3.71, k:0.01167

d:365.3nm
n:3.71, k:0.01167

d:365.5nm d:365.3nm d:365.2nm d:365.2nm d:365.3nm
n:3.71   n:3.71   n:3.71   n:3.71   n:3.71
k :0.01164 k :0.01168 k :0.01167 k :0.01167 k :0.01167

d:365.5nm
n:3.71, k:0.01165

d:365.5nm
n:3.71, k:0.01164
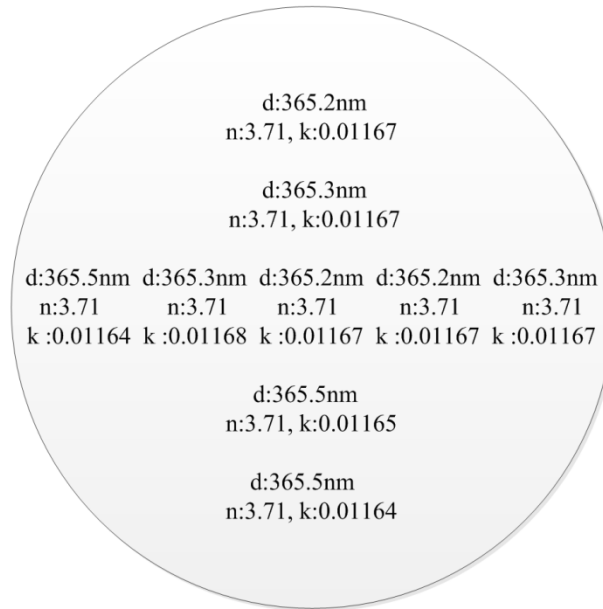
Figure 3-2 Graphical presentation of uniformity of thickness d and values of n and k for an example a-Si film deposited on a 4-inch (100) Si wafer.

After completing the a-Si film deposition and ellipsometry measurements, we diced the 4-inch wafer into 1 × 1-inch sample pieces using a Disco saw and cleaned them for further characterization. The samples were examined with x-ray diffraction (XRD) and scanning electron microscope (SEM) for base comparison prior to RTA heat treatment. The samples were subjected to RTA treatment with a matrix of different temperatures ranging from 600°C to 980°C for 10 minutes in an Argon ambient with a flow rate of 1000 SCCM. The RTA equipment (JetFirst-150 RTA by Jipelec) was used for this annealing process at 23% power. After RTA, each sample was characterized by a Siemens D-500 XRD system and a Woollam VAS ellipsometer to determine changes in structural

15

properties and optical constants. The ellipsometry measurements were taken in reflection at angles of 65°, 70°, and 75° in the spectral range of 900 nm to 1700 nm. We measured the preferred crystallographic orientation of the films by XRD in reflection from 10° to 90° with a step size of 0.02^{o} and a duration of 2 seconds at each step. The system uses Cu K-alpha radiation with a wavelength of 0.15418 nm. The XRD system is controlled by MDI datascan software and analyzed by JADE XRD pattern processing software. We operated the JEOL JSM 7600 SEM at 1keV–2 keV with images at 80,000x zoom in LEI mode.

3.3 Results and Discussion

To understand the effect of the annealing process on the a-Si in more detail, we examined the samples with SEM and ellipsometry for changes in surface roughness and for possible noticeable grain formation. The results for surface roughness are shown in Figure 3-3.
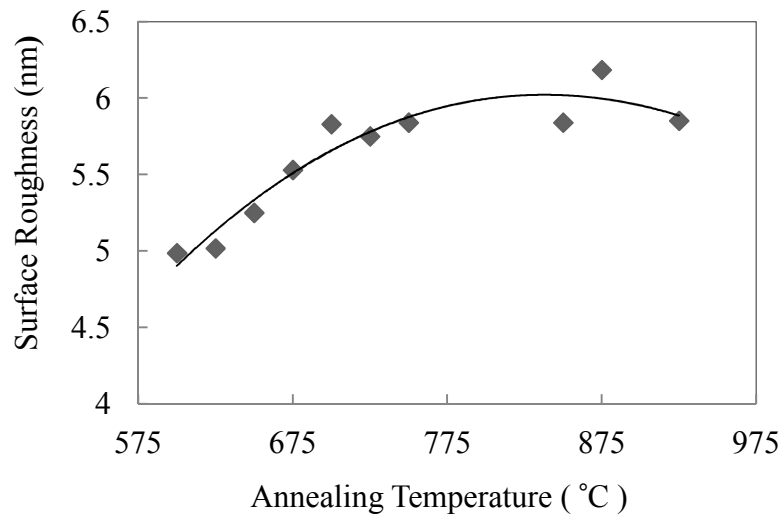
Figure 3-3 Surface roughness data as a function of annealing temperature. The solid line acts as a visual aid.

The surface roughness increases linearly with the annealing temperature of 600°C to ~700°C and saturates at higher temperatures. For the ellipsometry measurement, our model for the desired structure contains an effective medium approximation (EMA) layer that simulates the surface roughness layer [56-58]; it has 50% air and 50% top-layer Si. SEM results for selected annealing temperatures are presented in Figure 3-4.
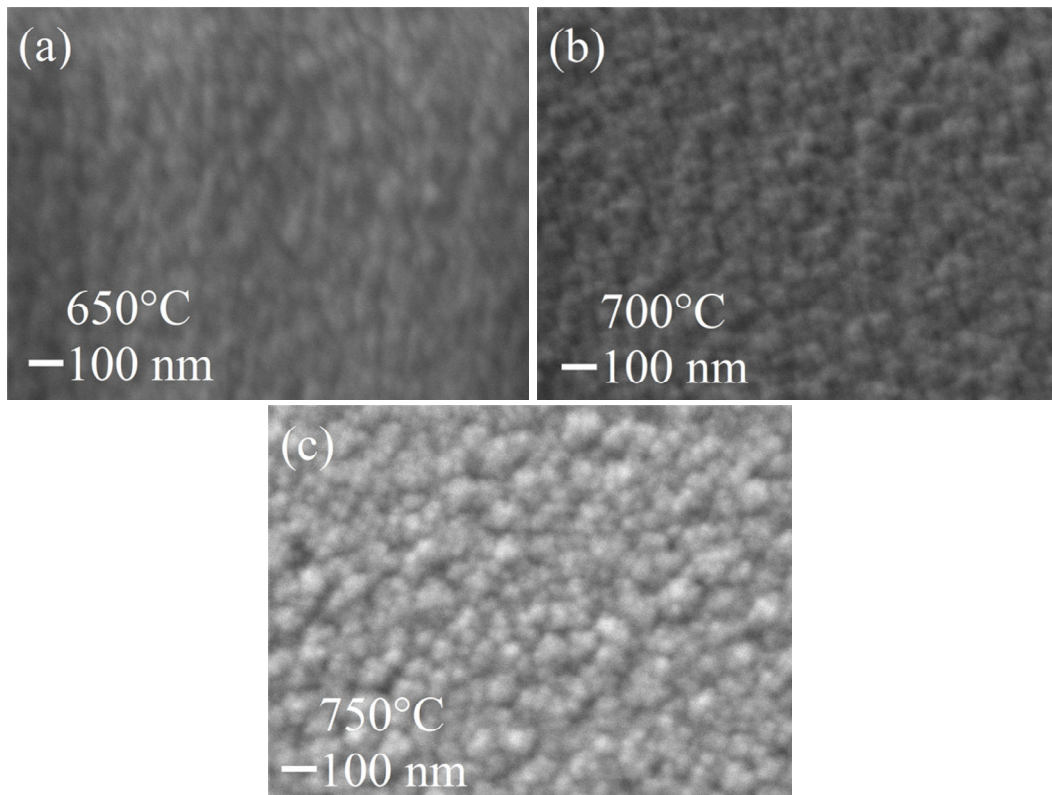
Figure 3-4 SEM images of the annealed samples at (a) 650°C, (b) 700°C, and (c) 750°C.

The XRD results for the annealed samples are shown in Figure 3-5. The data clearly show that the a-Si evolves to poly-Si as a function of temperature. Crystallization

starts with a (211) peak at annealing temperature of 650°C increasing with temperature up to 800°C at which point the (211) orientation signature begins to decrease. This coincides with the emergence of (111), (220), and (311) orientations with (111) domination. This trend continues for higher annealing temperatures, up to the limit of our RTA equipment of 950°C. The (211) peak completely disappears at 950°C. On the other hand, the (111) peak intensity increases sharply while the intensities of the other two peaks, (220), and (311), increase slowly [53-55,58]. The preferred crystal growth in the (111) orientation at higher temperatures is due to the strong anisotropic growth rate of the grains, which acts as an orientation filter that in turn is due to growth competition of various possible orientations as explained in [49]. For the (111) orientation, we observe that the speed of growth is the highest after 800°C. These results indicate that the faster growth of the (111) orientation at higher temperatures results in domination of the (111) orientation, which is due to the preferred free-energy minima of the film during heat treatment.
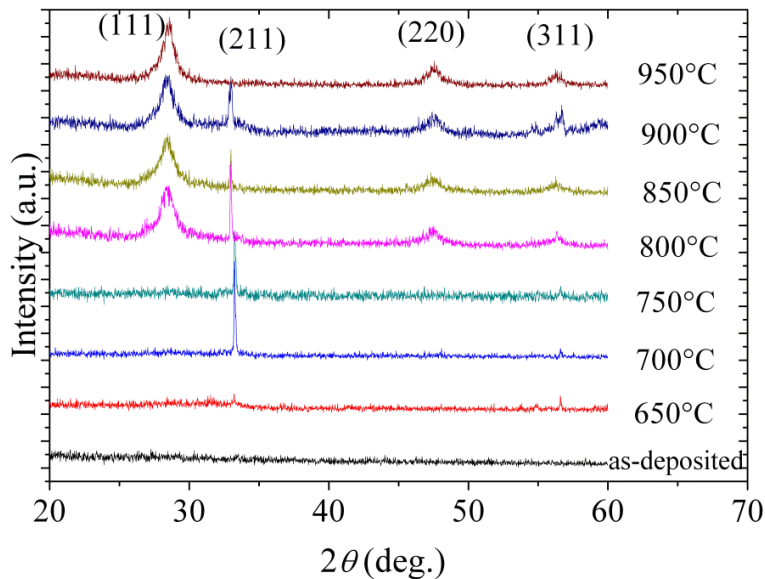
Figure 3-5 XRD data for samples annealed at 650°C to 950°C by RTA.

To obtain qualitative information about crystal planes, diffraction peak width (full width at half maximum, FWHM), and crystallite size, we use the JADE XRD pattern processing software. The experimental data are fitted with the Pseudo-Voigt profile function having a linear background and K-alpha2 emission line contribution. To estimate grain dimensions, we use the Scherrer equation, which is $L=K\lambda/\beta\cos\theta$, where λ is the X-ray wavelength, β is the FWHM, and K is a constant related to crystallite shape with value close to unity [55, 59]. Following Scherrer's formula, we find that, the average nanocrystallite size in the (111) plane is increased from ~13 nm to ~17 nm with temperature. For the (211) crystal plane, size decreases from ~142 nm to ~36 nm as the temperature is increased.
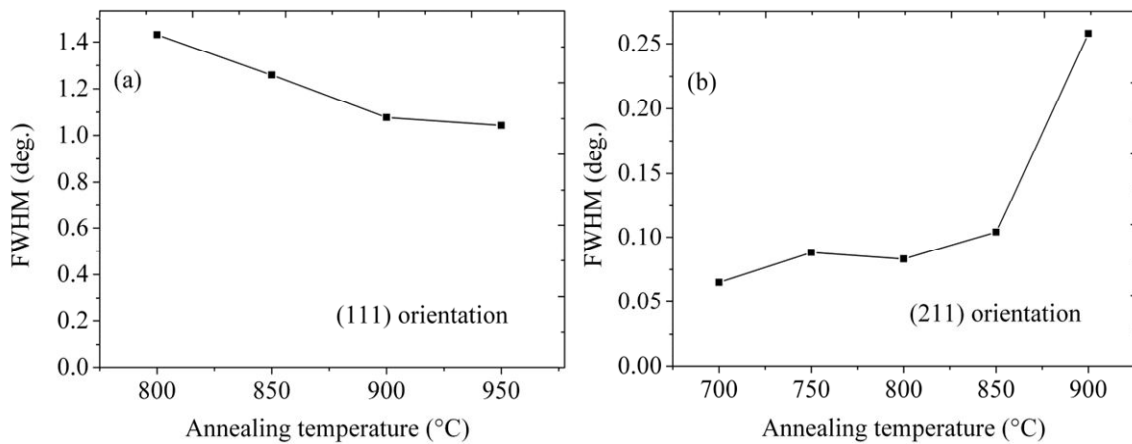
Figure 3-6 FWHM of (a) (111) and (b) (211) peaks as a function of the annealing temperatures.

Figure 3-6 shows the measured FWHMs for the (111) and (211) peaks. Figure 3-6(a) shows that for the (111) orientation, the peak width decreases with temperature, meaning that the crystallite size increases; the reverse occurs for the (211) peak in Figure 3-6(b).

19

We also provide the relative intensity of the (111) peak normalized with the (211) peak in Figure 3-7, which provides a better understanding of the crystal growth independent of the instrument profile variation. The figure suggests that the (211) peak dominates in the lower temperature range and the (111) peak dominates in the higher temperature range. Figures 3-5 and 3-6 indicate that the strongest peak is found in the (211) orientation in the 700°C to 800°C temperature range, but then the crystal growth preference shifts to the (111) orientation as the temperature rises farther.
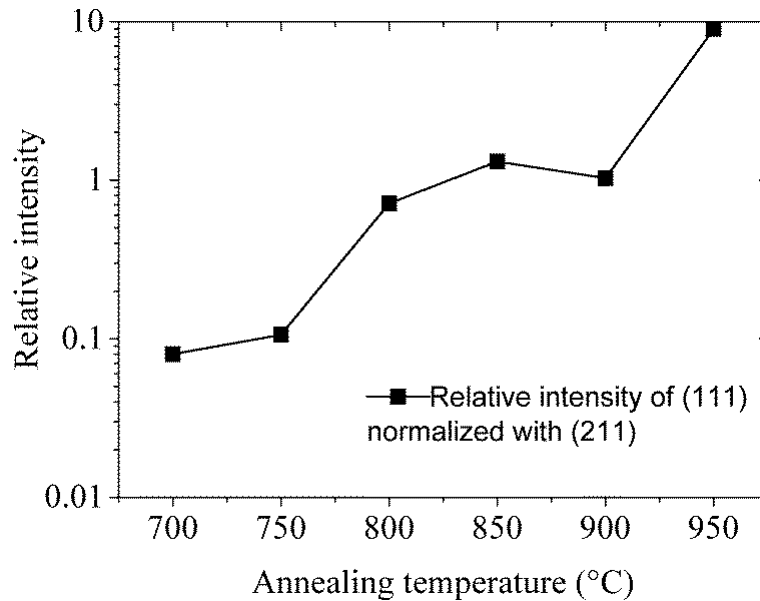
Figure 3-7 Relative intensity of the (111) peak normalized with the (211) peak intensity as a function of the annealing temperature (logarithmic scale).

Data depicted in Figures. 3-3, 3-5, and 3-7 suggest that the evolution of a-Si to poly-Si is not straightforward. To elucidate, the results suggest that for the annealing temperatures below 700°C, the a-Si may go through a condensation phase before the crystallization process occurs. Initially the surface becomes rougher as the temperature increases and then stabilizes. The onset of crystallization occurs around 700°C where the

(211) orientation forms. Crystal growth in this direction dominates up to 800°C; after that the higher annealing temperatures change the dynamics of the grain and crystal formation, resulting in stronger growth in the (111) direction and elimination of the (211) peak at 950°C. Emergence of the various plane orientations is a function of two key factors associated with any specific heat treatment process; these factors are time and temperature. For example, if we conduct the heat treatment in a furnace and provide enough time, even at a relatively low temperature of 550°C, plane orientations of (111), (220), and (311) will emerge, but not (211) as shown in [53]. The fact that the (211) orientation does not appear in the samples treated in [53] but emerges under RTA in our samples suggests an interesting line of future experimentation.
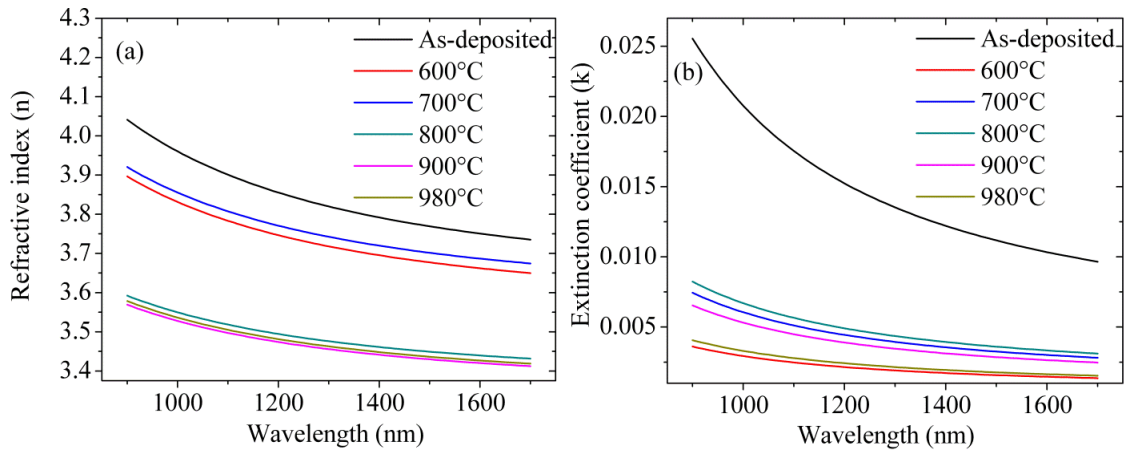
Figure 3-8 Dispersion of (a) refractive index (b) extinction coefficient as functions of annealing temperature from 600°C to 980°C.

Finally, Figure 3-8 shows the optical constants of the film. The as-deposited films (deposition chamber temperature ~25°C) have the highest values of (n, k). Under RTA beginning at 600°C, the graphs show that initially (n, k) both rise and then fall as the

annealing temperature for the entire range of scanning wavelengths increases. The probable explanation is that initially the film goes through a densification stage during which n increases. Subsequently, the decrement of the refractive indices is due to dependence on the crystalline phase amount and the grain size of the film; i.e., a larger grain size presents a smaller effective refractive index [60]. The originally deposited a-Si has a relatively high refractive index, signifying denser as-deposited films. Due to annealing, the initial densification process evolves into a microcrystalline structure formation followed by the formation of dynamic grain boundaries and various orientations that result in silicon films that are more structured. Due to the grains and the grain boundaries, we expect the films to be more porous with respect to the initial state of the a-Si films.
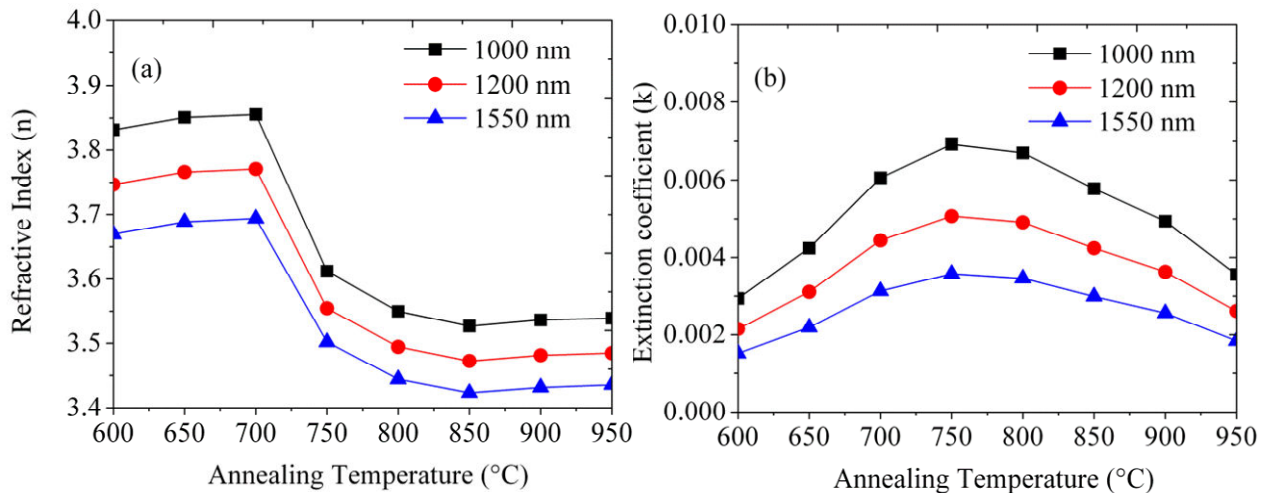
Figure 3-9 (a) Refractive index (n) and (b) extinction coefficient (k) as a function of the annealing temperature at three wavelengths.

Figure 3-9 summarizes these measured data for the range of annealing temperature at three specific wavelengths (1000 nm, 1200 nm, and 1550 nm). Both the n and k coefficients as functions of annealing temperatures correlate well with the

roughness data and crystal formation. The n coefficient increases linearly with the increasing temperature and obtains its maximum values at 700°C. The range of densification is from the starting temperature to this point. It decreases for the higher annealing temperature and stabilizes at ~800°C where the materials become polycrystalline.

The k coefficient increases initially to its maximum value at the temperature range of 700°C–750°C and decreases for higher temperatures, which indicates densification (higher absorption rate) followed by crystal formation and less absorbing films due to poly formation. A closer look at the rise and fall of the extinction coefficient shows that it follows the rise and fall of the (211) orientation intensity, which is the strongest peak. Figure 3-9 provides options for process conditions depending on the criteria for optical device design characteristics. For example, silicon films with high n and low k require an annealing temperature of no more than 600°C, whereas silicon films with lower n and k require annealing temperatures of 900°C and above.

3.4 Conclusion

In conclusion, this chapter reports an economical and efficient way to obtain polycrystalline Si films prepared from sputtered a-Si in conjunction with RTA instead of CVD Si. We demonstrate that the quality of the film can be improved under RTA. We achieve a significant improvement of the extinction coefficient relative to the as-deposited a-Si. We provide a way to engineer the optical constants depending on process-parameter control useful in the design of optoelectronic devices.

Chapter 4

Narrow Band Guided-Mode Resonance Transmission Filters

4.1 Introduction

In this chapter, we develop a theoretical and experimental analysis of narrow band guided-mode resonance (GMR) transmission filters with high transmission efficiency and flat low-transmission sidebands. We also address the challenges and the issues that this experimental verificaion entails which is related to the extinction coefficient and the mode confinement. Here, we propose theoretically optimized GMR narrow band transmission filters with low sidebands for both transverse magnetic (TM) and transverse electric (TE) polarized light. For the TE polarization we designed two transmission filters. One is enabled by the symmetric mode hence operated at normal incidence and the second is enabled by the anti-symmetric mode and is therefore operated at off-normal incidence angles. The transmission filter designed for TM polarization in enabled by the anti-symmetric mode of the grating. All designs have high efficiency and narrow transmission peak at around 1550 nm which is in the communication band. The linewidth of the filters enabled by the anti-symmetric modes depends on the angle of incidence; with lower angle we can have smaller linewidths. We obtained good agreement in the device performance between experiment and theory for the TM design. The TE transmission filter for the symmetric mode is highly sensitive to the structural parameters whereas the design for off-normal operation has significant discrepancy between experiment and theory because of high sensitivity to the extinction coefficient and irregularity defects in the actual device.

Typically to design a transmission filter, the transmission peak (reflection dip) of the characteristically asymmetric Fano resonance profile is used [34] and to lower the

sidebands, thin film layers are added in a high-reflectance design. At off-resonance wavelengths, the spectral response of a GMR element acts like a thin film with refractive index equal to the effective index of the grating. Dielectric thin films are utilized to make the wideband low transmission background (high reflectance) while maintaining the resonance peak at the desired wavelength. Alternatively, single layer grating structures having band-pass filtration characteristics can be found by employing optimization algorithms such as genetic algorithms or particle swarm optimization (PSO) [37]. But these single-layer grating transmission designs are difficult to achieve primarily because guided-mode resonance is fundamentally corresponded to a reflection peak. Also there are limitations in dielectric materials which can provide wide low transmission background with a single homogeneous layer. Such single layer high modulation transmission gratings provide two resonance excitations. One lays the foundation for the low transmission background while the other provides the transmission peak. Typically higher diffracted orders associated with relatively weak coupling constants provide narrow transmission peak and the low sidebands are supported by the lower order diffracted waves with stronger coupling [34]. These couplings can be associated with symmetric or anti-symmetric modes of the grating with respect to the mirror symmetric plane of the device. In the case where the light is coupled with the symmetric mode, resonance can occur at normal incidence because the overall integration of the field amplitude is not zero in the same material; on the other hand, anti-symmetric mode associated with transmission resonance yields vanishingly narrow bandwidth for small incident angles. This type of transmission resonance is generally induced in wideband reflection gratings under off-normal incidence as described by Shokooh-Saremi [61]. Similarly asymmetric grating GMR elements can yield transmission resonance at normal incidence.

25

In this chapter, we design guided-mode resonance (GMR) transmission filters for both transverse magnetic (TM) and transverse electric (TE) polarization by using an inverse numerical technique known as particle swarm optimization (PSO) [37]. We use rigorous coupled-wave analysis (RCWA) [38] for numerical evaluation of GMR filter performance in our PSO code. Also to compute the field excitation and the effects of the extinction coefficienct, we use MCgrating and our own software RMsolver.

4.2 Narrow Band Guided-Mode Resonance Transmission Filters for TE Polarization

In this study we design two transmission filters for TE polarization. The 1st design is a partially etched single layer Si grating on a glass/quartz substrate. This design supports transmission resonance at normal incidence enabled by the symmetric mode of the grating. The 2nd design is a single layer Si grating operated at off normal incidence due to anti-symmetric mode of the grating.

4.2.1 GMR Transmission Filter with Partially Etched 1-D Grating Enabled by Symmetric Mode

4.2.1.1 Design and Analysis

Figure 4-1 shows theoretical performance of the designed transmission filter for TE polarization. As shown in the inset of the figure, the filter consists of, from bottom to top, a silica substrate and a homogeneous film of Si underneath a binary grating layer in Si. Design parameters are homogeneous Si film thickness d_{HL} = 295 nm, grating depth d_g = 330 nm ($d_{total}=d_g+d_{HL}$), fill factor F = 30%, and the grating period Λ = 1010 nm. Here, the refractive index of Si is assumed to be 3.48. This design does not include the extinction coefficient k contributed by the material absorption or scattering loss due surface roughness. With these parameters by the PSO method, we obtain a narrow

transmission peak with low spread out sidebands as shown in Figure 4-1. The linewidth of the zero-order transmission peak is 0.5 nm with an extinction ratio of 534 and Q- factor of 3.1×10^3.
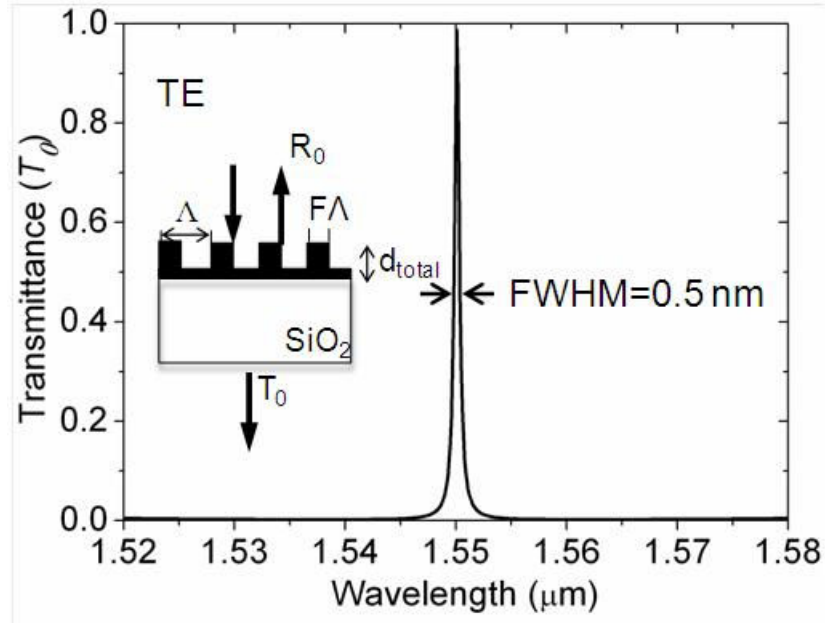
Figure 4-1 Spectral response of optimized GMR transmission filter for TE polarization with parameters $d_{total} = d_g + d_{HL}$, $d_g = 330$ nm $d_{HL} = 295$ nm, $\Lambda = 1010$ nm, F= 0.3, n=3.48, normal incidence. Schematic structure of the device is shown in the inset.

To check the robustness of our design, we calculate the contour map and tolerance matrix of the design considering 3% fabrication error on layer thicknesses (d_g and d_{HL}), fill factor (F), and period (Λ). Figure 4-2(a) shows the effect of variation of the grating thickness of the zero-order transmission efficiency (T_0). Inset of the figure shows magnified response. Figure 4-2(b) shows the spectral response of the device considering 3% fabrication error.

27

Figure 4-2(a) Zero-order transmission contour map showing effects of grating thickness on the resonance spectra. (b) Response with 3% fabrication error in grating thickness.

From the above figure we can conclude that the design is robust against the variation in the grating thickness as the position and the efficiency of the T_0 resonance do not change much. We also see, for the grating thickness of 250 or lower, the spectrum

shows an asymmetric Fano profile but as the thickness is increased the line shape starts to resemble a symmetric Lorentzian profile. To see the effect of variation in the homogeneous layer thickness on the transmission efficiency, we provide Figure 4-3.

Figure 4-3(a) Zero-order transmission contour map showing effects of homogeneous layer thickness on the resonance spectra. (b) Tolerance with 3% fabrication error.

Figure 4-4(a) Zero-order transmission contour map showing effects of fill factor change on the resonance spectra. (b) Tolerance with 3% fabrication error.

From the figures, we see that the position and the efficiency of transmission resonance peak are highly sensitive to the homogeneous layer thickness. With only 3% fabrication error in this parameter, the efficiency can drop from 100% to 30% and even lower. For the thicknesses in between ~302 nm and 308 nm, the spectrum becomes vanishingly narrow. From Figure 4-4 we observe that the effect of fill-factor change on the resonance

profile is also not significant except for the fill factor of more than 0.35 the resonance shows ultra narrow line shape. From Figure 4-5(a) and (b), we confirm that the resonance profile is most susceptible to the variation in grating period. The figure in the inset shows that the transmission resonance becomes almost discrete with the slight variation in the grating period. Figure 4-6 shows the effect of variation in the angle.

Figure 4-5(a) Zero-order transmission contour map showing effects of grating period variation on the resonance spectra. (b) Tolerance with 3% fabrication error.

Figure 4-6 Zero-order transmission contour map showing effects of incidence angle variation on the resonance spectra.

Our single-layer grating design produces strong modulation to support the excitation of two types of GMRs: one provides the low-T_0 sidebands while the other gives the transmission peak. To get a deeper understanding of the coupling, we calculated the field profile at the transmission maxima and at side bands. According to Figures 4-7 and 4-8, this resonance feature is induced by the excitation of TE_0-like mode by the 2nd order diffracted waves whereas resonant excitation of leaky TE_2-like mode by the 1st order coupling contributes to the low-T_0 background. The total internal field plot shown in Figure 4-8 suggests that the fields are more concentrated in the homogeneous layer so any change in this layer significantly affects the coupling conditions. Therefore, the diffraction efficiency at the resonance under a slight change in the grating layer, while keeping the homogeneous layer constant, does not affect the resonance much as shown in the tolerance matrix as well.
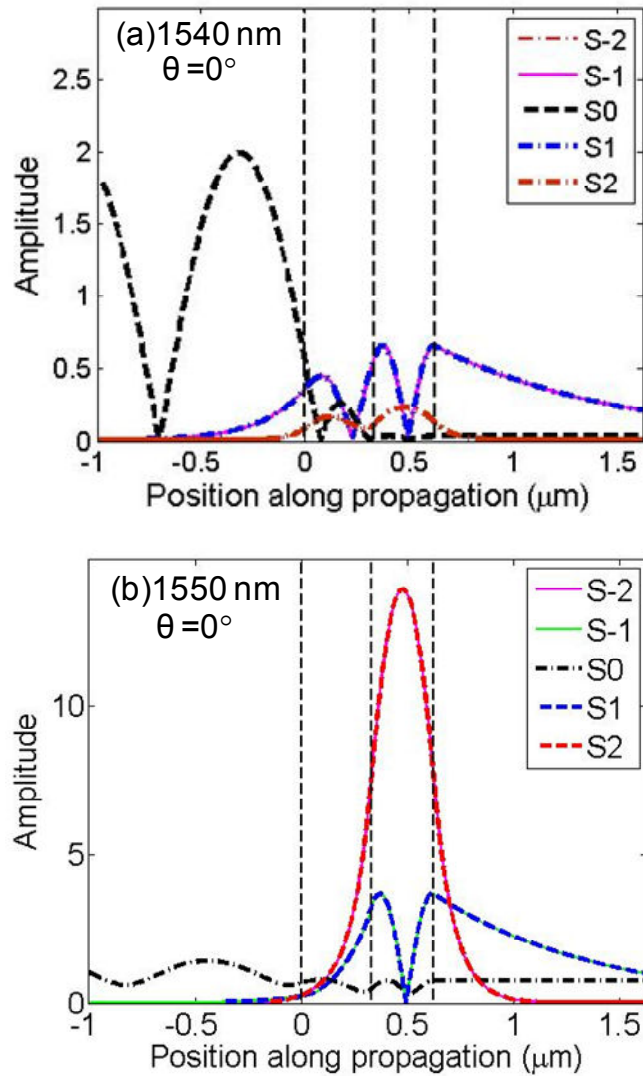
Figure 4-7(a) Coupling orders at the side band (1540 nm) (b) Coupling orders at the

transmission peak resonance wavelength of 1550 nm.

Also looking the field profile we can be sure about the symmetry of the mode with

respect to the mirror symmetry of the device. In this case, diffracted waves generated by

the subwavelength grating structure is phase-matched to the leaky waveguide-mode,

occurring at the resonance at normal incidence because the overall integration of the field amplitude is not zero in the same material.
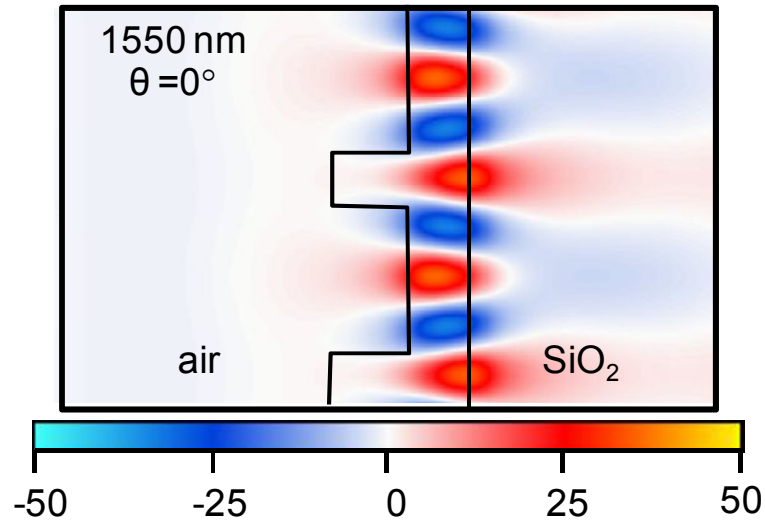
Figure 4-8 Total internal field at the transmission peak resonance wavelength (1550 nm).

Transmission contour maps and the tolerance matrix with the variation of structural parameters shown in Figures 4-2 to 4-6 provide the sensitivity of this design and hence the difficulties associated with the fabrication of this device. So we make other designs for which the devices are fabricatable with standard nanofabrication facilities.

4.2.2. Single Layer 1-D Grating Acting as GMR Transmission Filter Enabled by Anti-Symmetric Mode

4.2.2.1 Design and Analysis

In contrast to the previous design, this TE filter has only a completely etched single Si 1-D grating layer with parameters d_g = 200 nm, fill factor F = 34%, Λ = 947 nm with n of 3.48. We consider the extinction efficient k to be zero. This design also yields a narrow transmission peak at off normal incidence with low spread out sidebands as shown in Figure 4-9. The inset shows schematic diagram of the device. The linewidth of

the zero order transmission peak at the incident angle $\theta = 1°$ is 0.6 nm with a theoretical extinction ratio of ~8400 and Q factor of 2.6×10^3. Linewidth of the transmission peak depends on the incidence angle.
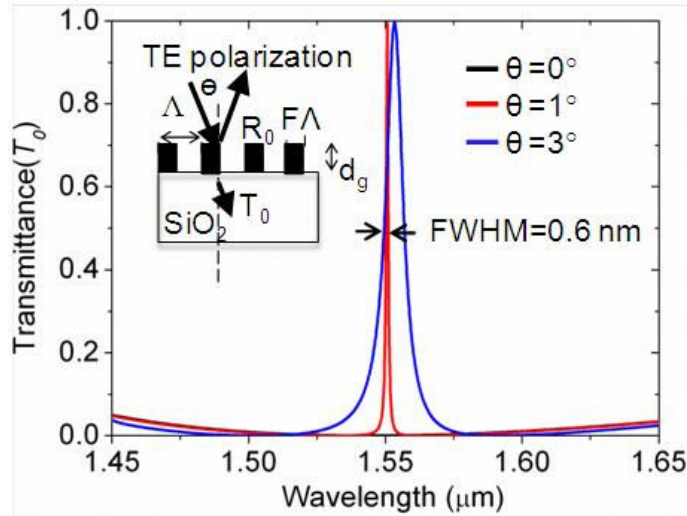
Figure 4-9 Spectral responses of optimized GMR transmission filters for TE polarization with parameters d_g= 200 nm, Λ = 947 nm, F = 0.34, n = 3.48, k = 0. Schematic of the structure is shown in the inset.

To check the robustness of our design, we calculate the contour map and tolerance matrix of the design considering 3% fabrication error in grating layer thickness d_g, fill factor (F), and period (Λ). Here the resonance is associate with incidence angle of $\theta = 3°$. Figure 4-10 shows the effect of variation of the grating period on the zero order transmission efficiency (T_0). From the figure we see that the grating period has minor effect of the FWHM or the transmission efficiency of the resonance peak but strongly affects the resonance wavelength. Figures 4-11 illustrates the resonance spectra as a function of grating thickness. We observe the effect of change in the fill factor in Figure 4-12. Like the other parameters variation in fill factor only shifts the resonance position. Out

of these three structural parameters, the effect of grating thickness is the least prominent

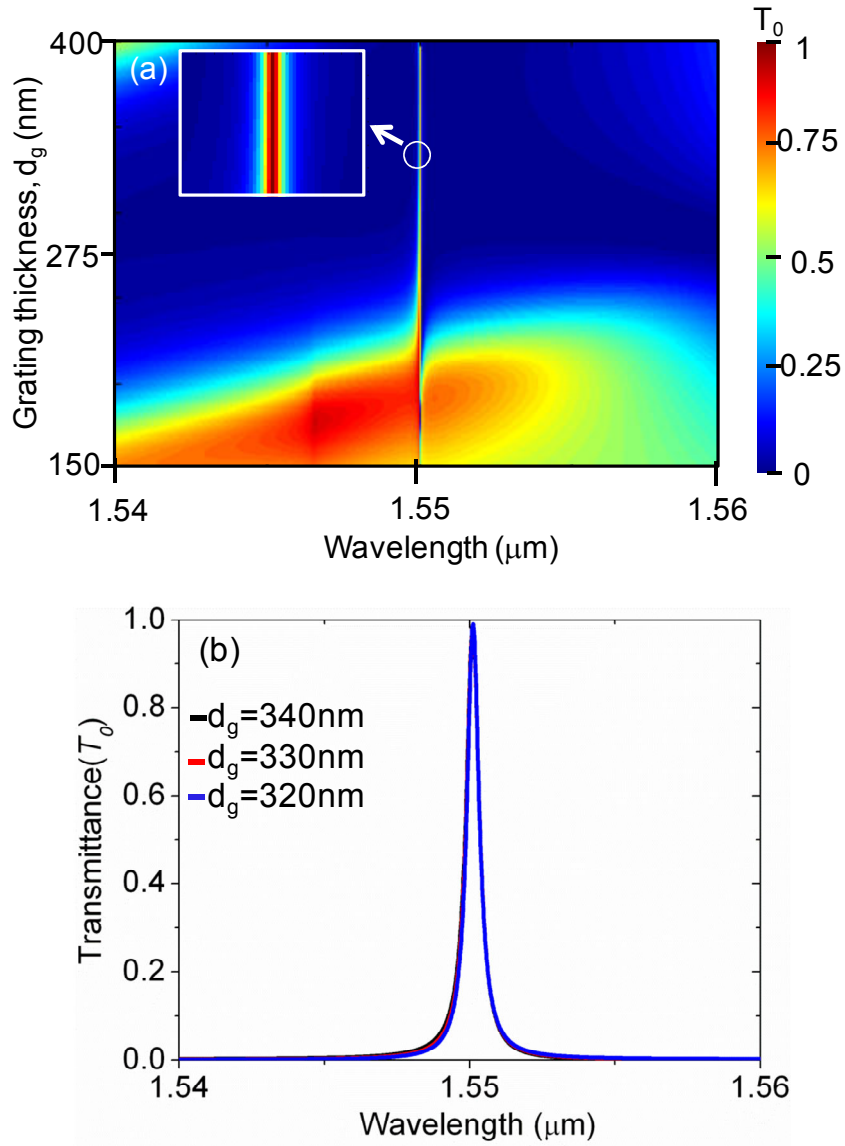on the linewidth, efficiency and the position of the resonance spectra.
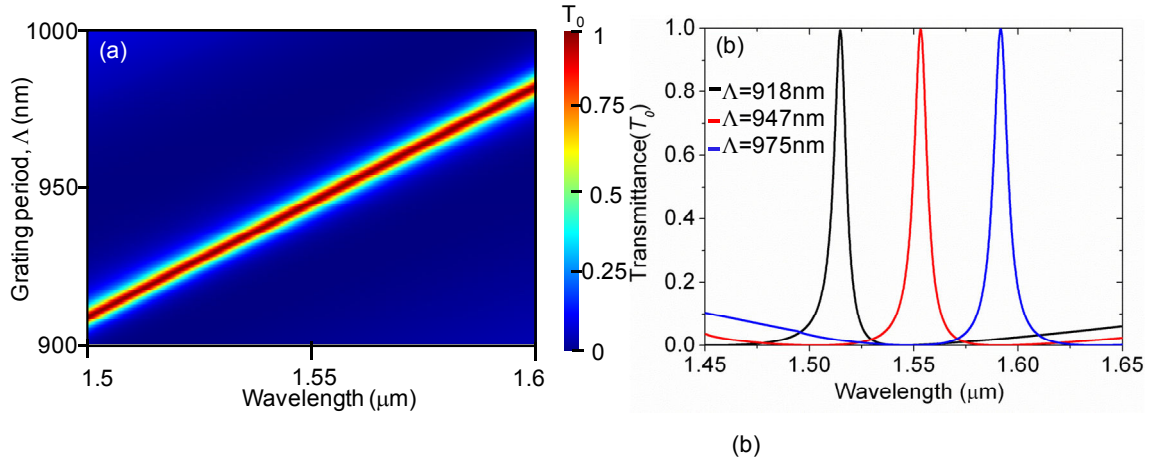
Figure 4-10(a) Zero-order transmission contour map showing effects of grating period on

the resonance spectra. (b) Response with 3% fabrication error in grating period.
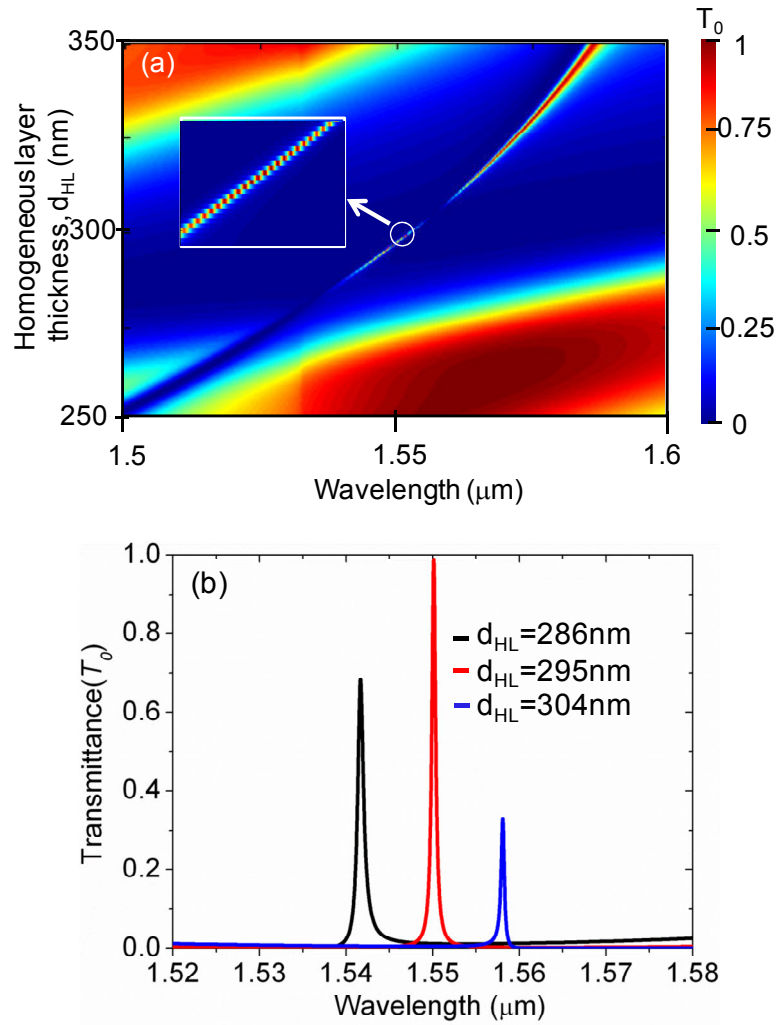
(incidence angle, θ =3°).
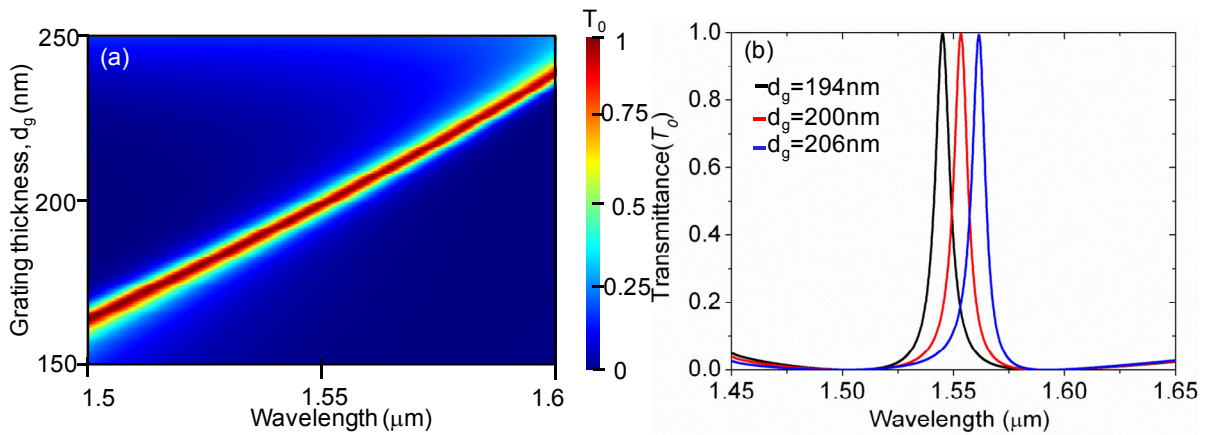
Figure 4-11(a) Zero-order transmission contour map showing effects of grating thickness

on the resonance spectra. (b) Response with 3% fabrication error in grating thickness.
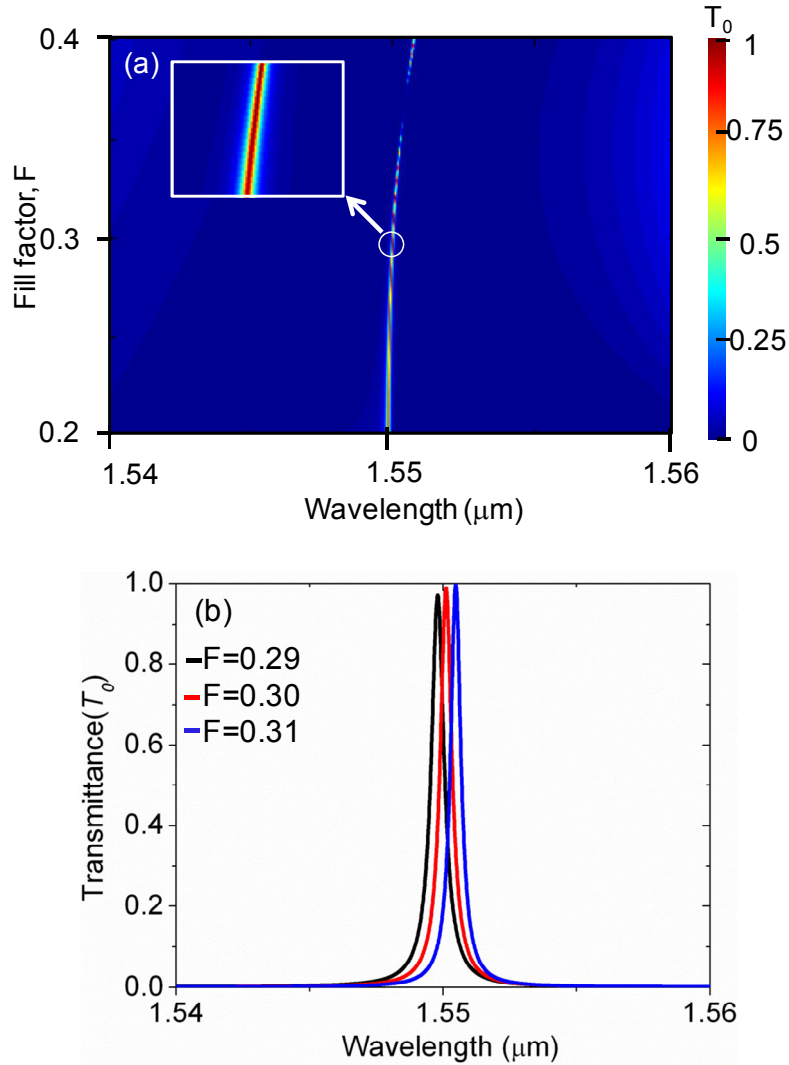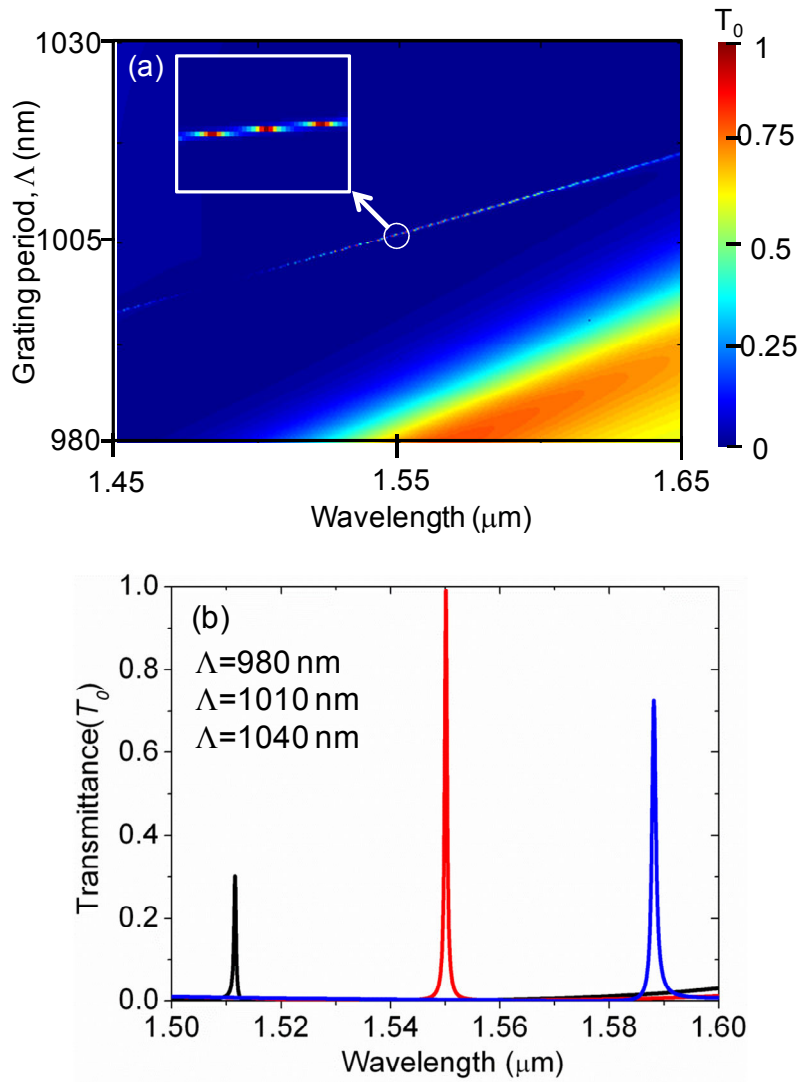
(incidence angle, θ =3°).
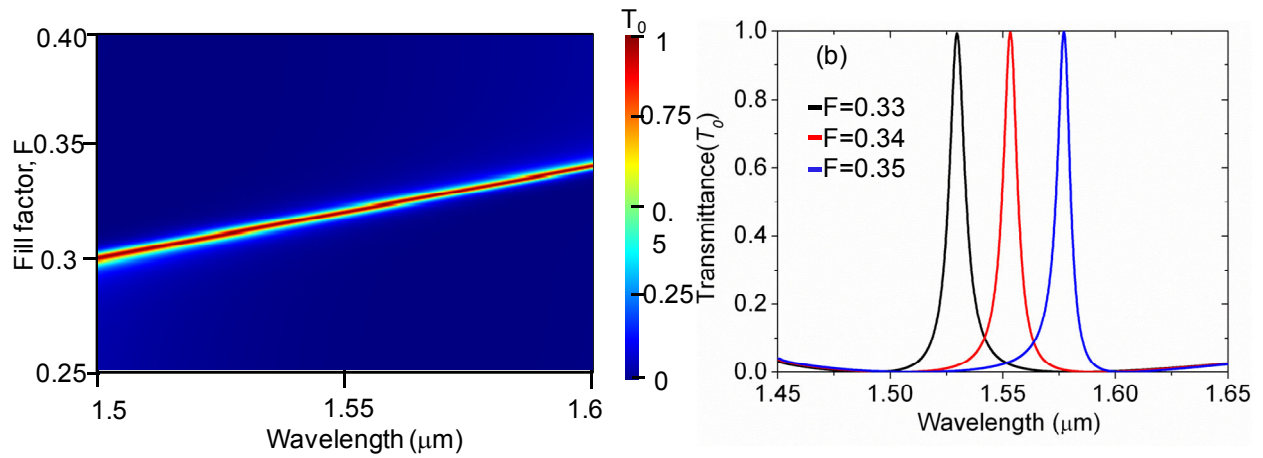
Figure 4-12(a) Zero-order transmission contour map showing effects of grating fill factor on the resonance spectra. (b) Response with 3% fabrication error in grating fill factor (incidence angle, $\theta = 3°$).
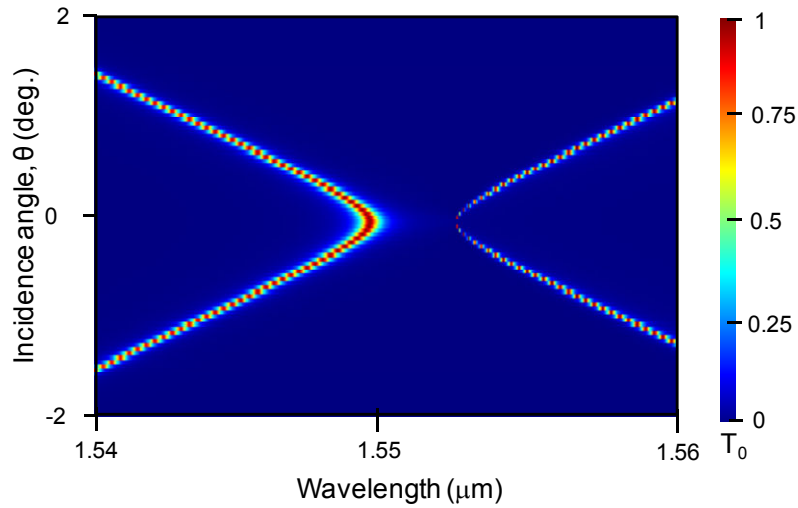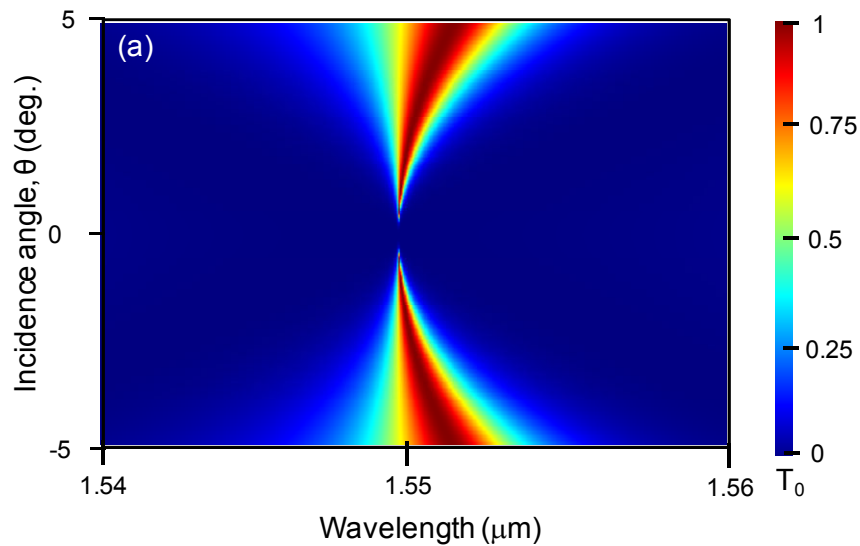

Figure 4-13 Zero-order transmission contour map showing effects of incidence angle on the resonance spectra.

If we look at the angular response of the device in Figure 4-13, we see, at normal incidence there is no resonance. As the angle increases, resonance linewidth starts to increase. This phenomenon can be understood more clearly with the Figures 4-14. Figures 4-14 (a) and (b) show the coupling orders at the low sideband (1562 nm) and at the resonance peak (1550 nm) respectively. Figures 4-14 (c) and (d) show the total internal field corresponds to the low sideband (1562 nm) and transmission peak resonance wavelength (1550 nm). The transmission peak feature is induced by the excitation of anti-symmetric TE_0-like mode by the 1st order diffracted waves at the upper edge of the second stop-band [62] whereas resonant excitation of leaky symmetric TE_0-like mode by the 1st-order coupling contributes to the low-T_0 background. The anti-symmetry of the mode with respect to the mirror symmetry of the device yields vanishingly narrow bandwidth for small incident angles and thereby the mode is extremely sensitive to the material absorption or random scattering by film imperfections. At normal incidence, integration of the overall field amplitude in the same material is zero, so light cannot be coupled to waveguide mode; Creating asymmetry with off normal incidence angle, diffracted waves start to couple to the leaky waveguide modes of the device hence a narrow transmission resonance emerges at a particular wavelength. If we increase the angle more, coupling becomes stronger therefore photon life time in the waveguide becomes smaller which results in a lower Q resonance (broader FWHM).
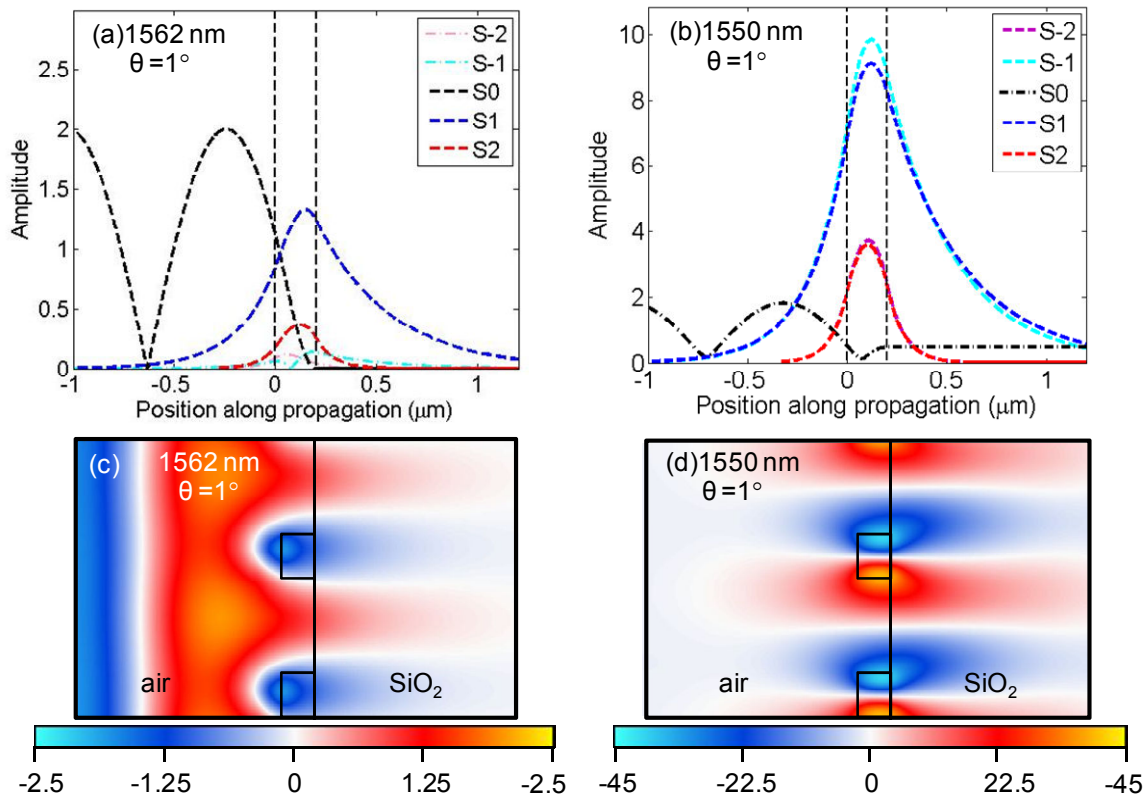
Figure 4-14(a) Coupling orders at the low transmission sideband (1562 nm) and (b) at the

transmission peak resonance wavelength (1550nm). (c) Total internal field at the low

transmission sideband (1562 nm) (d) Total internal field at the transmission peak

resonance wavelength (1550nm).

From the total internal field plot shown in Figure 4-14(d) we find that the resonant

excitation of fields for transmission maxima is concentrated very close to the sidewalls. It

suggests the device should be very sensitive to any irregularity defects on the sidewalls.

4.2.2.2 Fabrication

      The fabrication process of our narrow band GMR transmission filter for TE polarization is presented as follows. First we cut a microscopic slide into 1x1 inch^2 pieces and clean them with acetone, methanol, and IPA for 5 minutes for each solution. Then we remove all the residue by putting the slides in de-ionized (DI) water and finish off by baking to remove any moisture from the surface. Then a layer of amorphous Si is deposited on the substrate with the NanoFab AJA sputtering system at a sputter pressure of 5mT for 14000 s (~ 4 hours). After a-Si layer deposition, we anneal the a-Si layer on a rapid thermal annealing system (Jet First RTA) at 490°C for 10 minutes to improve the optical constants, i.e., lower the extinction coefficient almost an order from the as-deposited a-Si. The effect of annealing is shown by Figure 4-15.
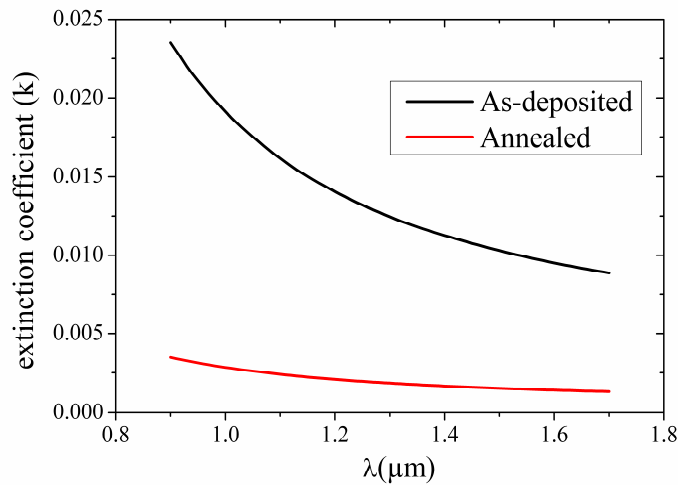
Figure 4-15 Effect of rapid thermal annealing on the extinction coefficient of a-Si.

      The thickness and the optical constants are measured by ellipsometer. For the film thickness of 217 nm, the optical constants are measured as n = 3.61 and k = 0.0013 at 1550nm. To produce the grating pattern, we use a UV holographic lithography system

as shown schematically in Figure 4-16. After spin coating 389 nm positive photoresist coating on the a-Si deposited substrate, we expose it in the interferometric lithography system for a matrix of different exposure times and grating periods
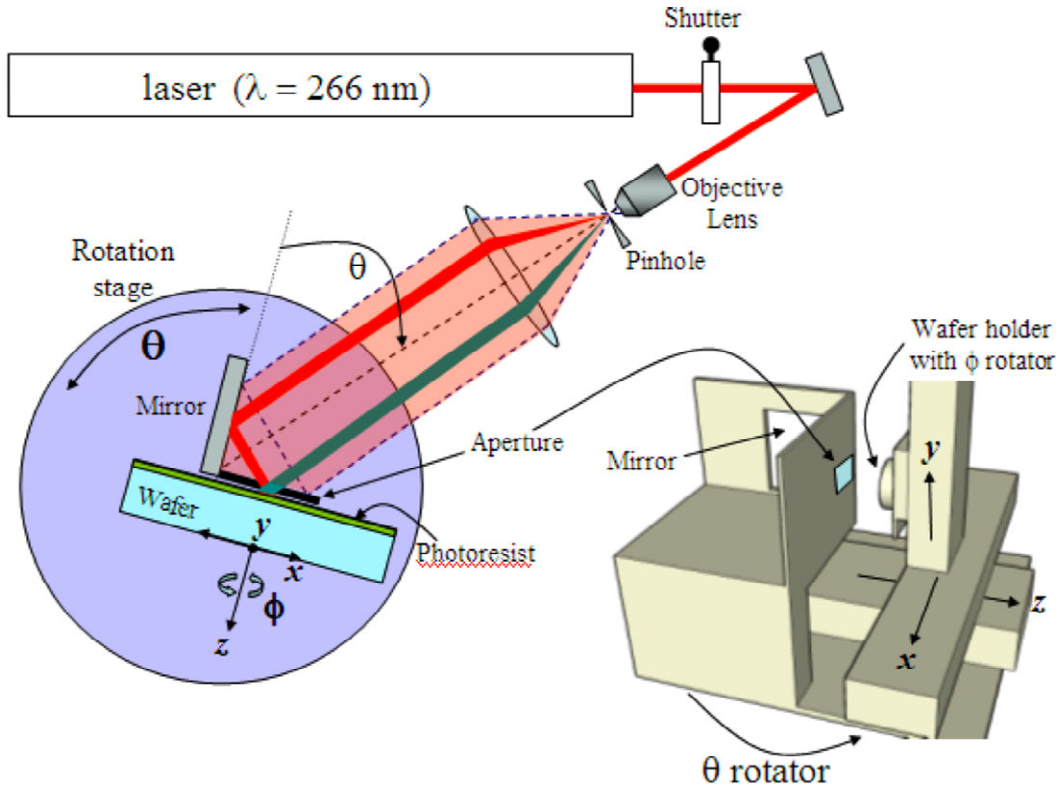
Figure 4-16 Schematic view of laser interferometer with wavelngth 266nm .

Specific fill factor of the grating is achieved by controlling UV exposure time and power. This photoresist grating is then cured at 130°C for 13 minutes as an etch mask for the reactive-ion etch (RIE) through the a-Si layer. The a-Si layer is then etched for 8 minutes with SF_6/CHF_3 gas mixture operated on a RIE system which transfers the photoresist pattern on the a-Si layer. The remaining photoresist mask is removed by ashing with O_2 plasma. To remove the photo resist residue we put the samples in nanostrip for 6 minutes and clean it properly. Finally, the single layer waveguide grating

structure is achieved. Figure 4-17 shows a schematic diagram of the general fabrication steps for these transmission filters
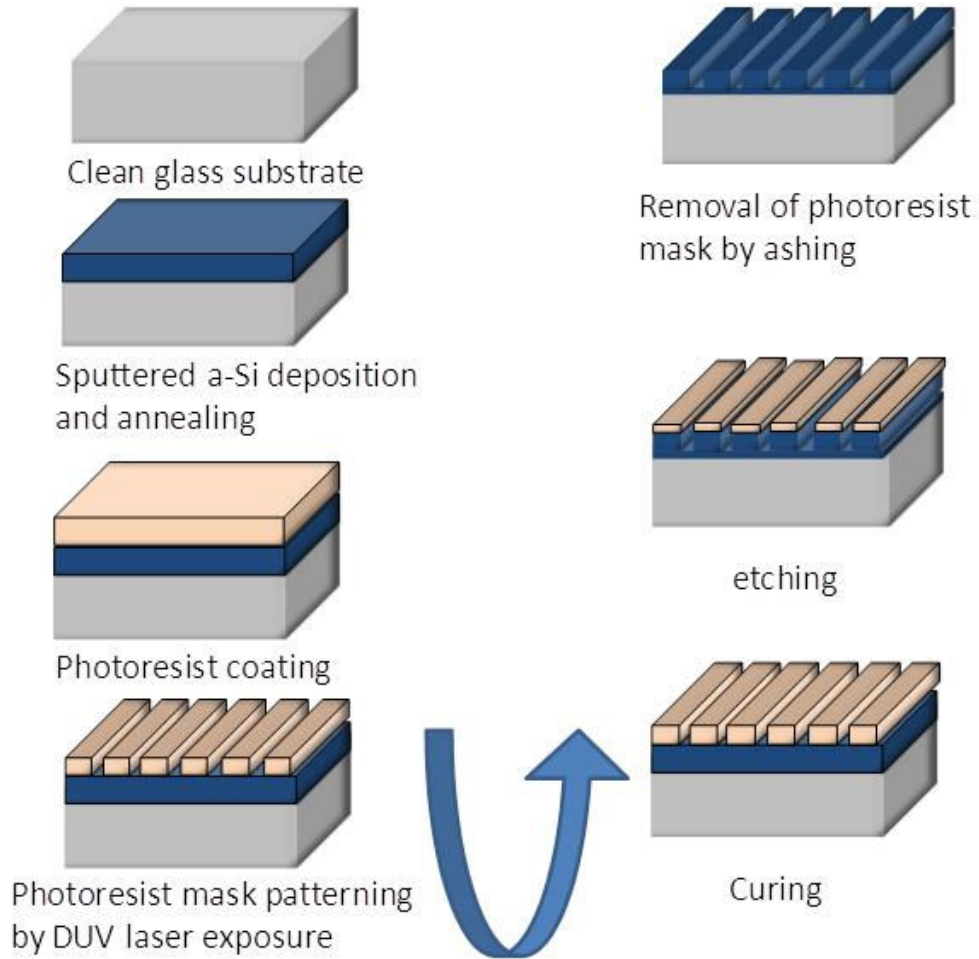
Figure 4-17 Schematic view of the fabrication steps.

4.2.2.3 Characterization

The fabricated devices are characterized with both nondestructive (AFM) and destructive (SEM) method. Figure 4-18 shows the AFM as well as SEM images of the fabricated devices. From the figure, we find that the TE device has grating period of ~

917 nm, the grating layer thickness of 163 nm, and the fill factor of 0.306. Also the SEM images show the top view of the fabricated device to confirm the uniformity of the device and the parameter measurements done with the AFM.
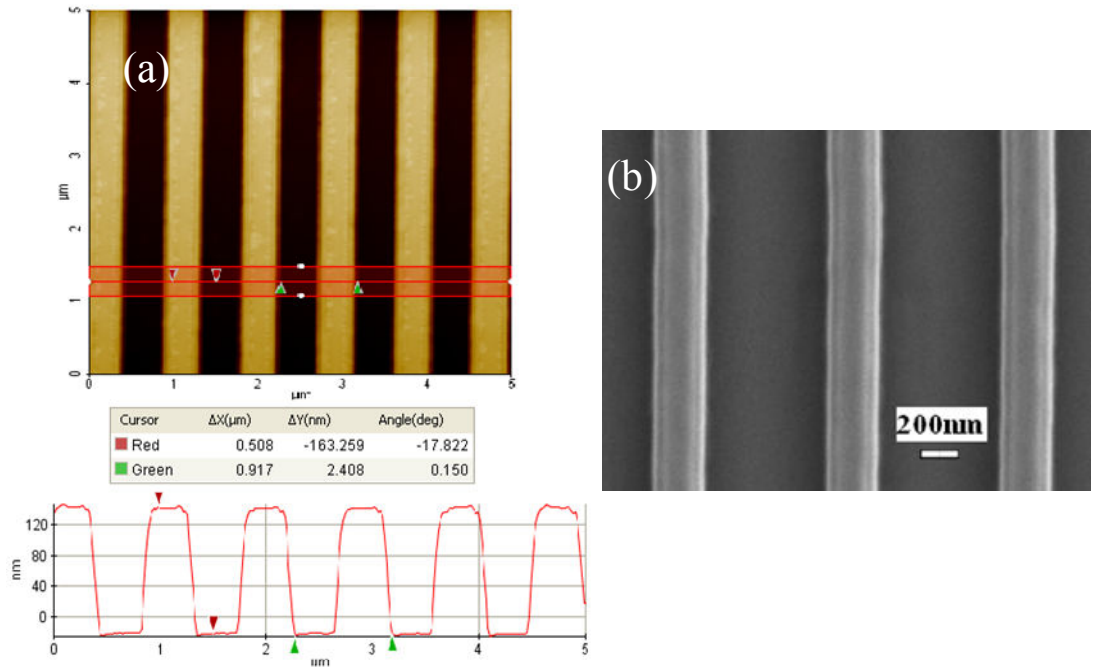
Figure 4-18(a) AFM and (b) SEM image at × 4300 zoom of the fabricated device.

For the measurements of the spectral response of these transmission filters we built a setup schematically illustrated in Figure 4-19. The angle of incidence is controlled by the rotation stage where the sample is placed and the stage is operated by a Labview program. An angular resolution of 0.001 degree can be achieved by this automated system. To set the polarization state, a polarizer is used before the sample stage. The transmitted beam is then measured with an optical spectrum analyzer for a wavelength range of 1400 nm to 2000 nm in 1 nm steps.
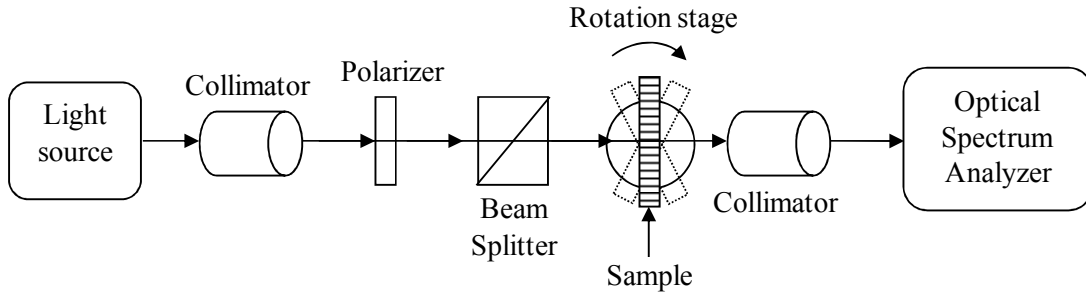
Figure 4-19 Schematic view of the optical measurement setup.

Measured transmission spectra through the fabricated TE device are presented in Figure 4-20(a) with the numerically calculated spectrum as shown in Figure 4-20(b) for comparison. Spectral response of the fabricated TE filter shows significant difference from that due to numerical calculation. From the design contour map and tolerance matrix previously shown, we observe that there should be a resonance even if we consider some parameter shift at the wavelength close to the design at higher incidence angles for 3 degree or more. But the experimental result shows negligible sign of a resonance feature.
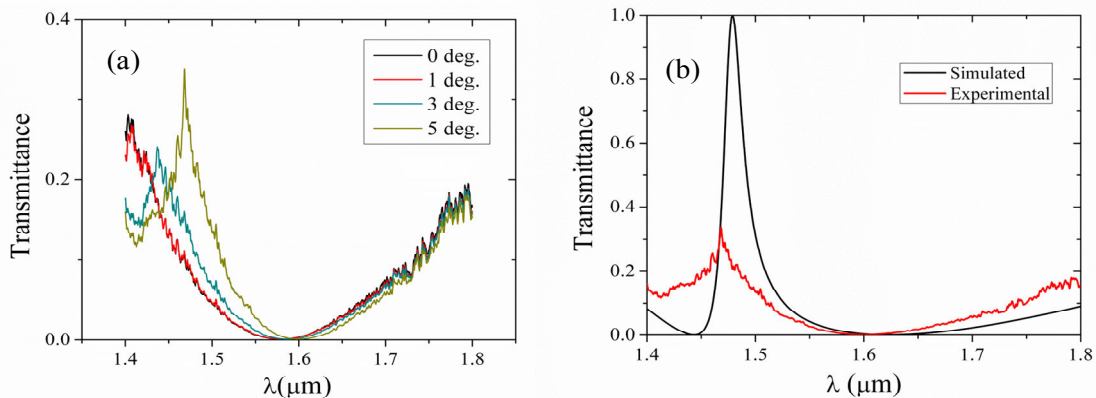
Figure 4-20(a) Spectral response of the fabricated TE device at different incidence angles (b) Comparison with simulation for the incidence angle of 5 degree. Device parameters are Λ =917 nm, d_g = 163 nm, and F = 0.306.

4.2.2.4 Discussion

These differences between the experimental and simulated results are due to the effect of extinction coefficient and the mode confinement. We see the effect of extinction coefficients on resonance peaks in Figure 4-21(a). With k close to 0.001, the transmission efficiency decreases down to 30%. Also the narrower the linewidth, the larger the effect of k. From Figure 4-21(b), we see that the field is strongly confined at the edges of the grating ridge so this TE filter is suspected to be very susceptible to any irregularities on the sidewalls. With our fabricated device we could not observe any resonance even with higher incidence angle which has broader linewidth in theory. So irregularities on the sidewall seem to be the primary reason for suppressing the resonance.
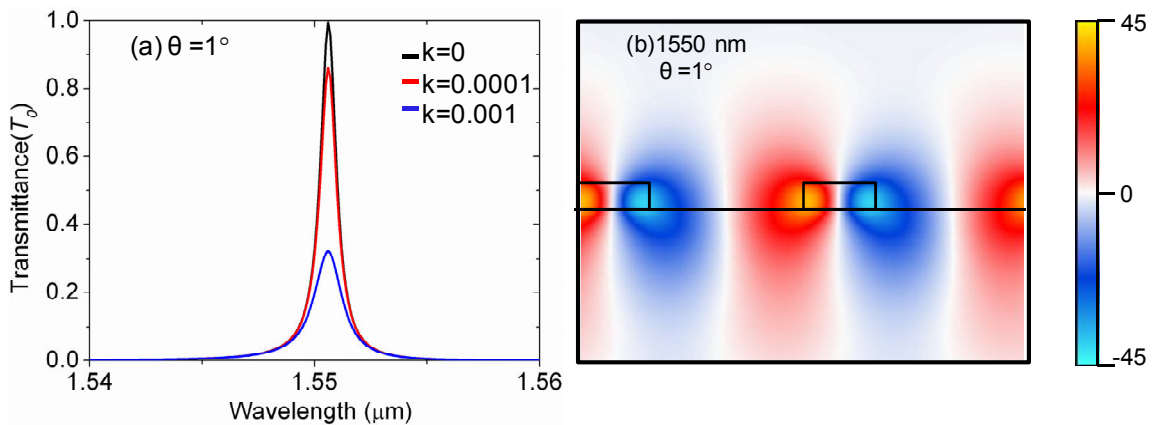
Figure 4-21(a) effect of extinction coefficient on transmission efficiency at the incidence angle of 1 degree. (b) field excitation at the grating ridge at resonance wavelength.

To improve the device performance, we can consider materials with lower extinction coefficient and fabrication processes for roughness-free grating profile. For example, silicon-on-insulator (SOI) can be used for a roughness-free device with chemical etch process as recently introduced in [63]. Silicon on Quartz (SOQ) substrate

has single crystal Si thin film on a quartz substrate. The advantage of this kind of substrate is the single crystal Si which has low extinction coefficient and can be used for anisotropic etching methods with KOH.

4.2.3 GMR Transmission Filters with Trapezoidal Grating by KOH Etching

To counter the effect of sidewall roughness or the irregularities in the sidewalls, we plan to have GMR Transmission filters with trapezoidal gratings. As the etching is going to be done with KOH along with the crystal plane, it is expected to have very smooth structure [64,65]. We have already verified the surface roughness with KOH etching on Silicon on Quartz (SOQ) wafers provided by Shin-Etsu Japan.

4.2.3.1 Experimental steps
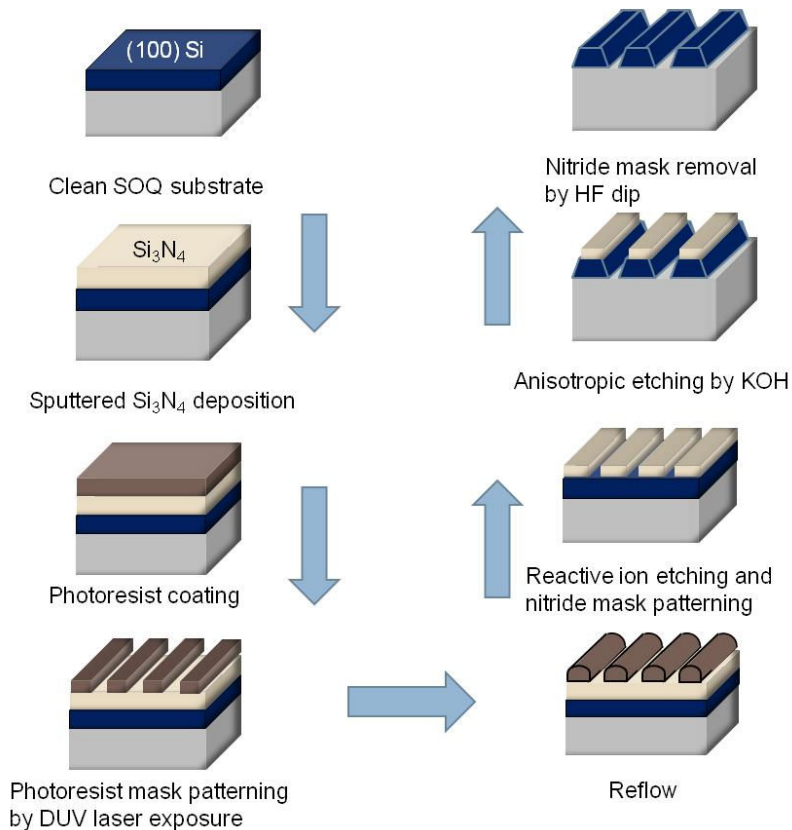
Figure 4-22 Steps by step process of fabricating trapezoidal gratings with KOH etching

Figure 4-22 illustrates the processing steps. These are as follows:

- Step 1:Deposit Si_3N_4 Si wafers (100).

    - Sputtering: 2.8 mT, 150W

        - 60 mins: ~64 nm thick

        - 30 min: ~40 nm thick

- Step 2:1D PR Grating with HMDS

    - Cut wafer after coating with HMDS and PR

    - Align sample according to the crystal plane

    - Period: 1000nm, Exposure time: 80s, Power: 100mW (power meter~58 mW), phi:0 deg

- Step 3: Reflow

    - At 200^0C for 10s

- Step 4: Etch Si_3N_4 with RIE

    - Descum: 20s

    - Etch: 1 min 45s

    - Ash :8 min,

    - AZ stipper: 80^0C for 30 mins (155^0C on the baker)

- Step 5: 50:1 HF dip for 1 min to remove native oxide before KOH etch

- Step 6: KOH etch

    - 22.5% wt KOH

    - ~35^oC (~67^oC on the baker) for 5 min

4.2.3.2 Characterization

We have done the characterization by both non destructive (AFM) and destructive (SEM) methods. Fig. 4-23 show the AFM image of (a) Si_3N_4 grating and (b) Si grating with Si_3N_4 mask.
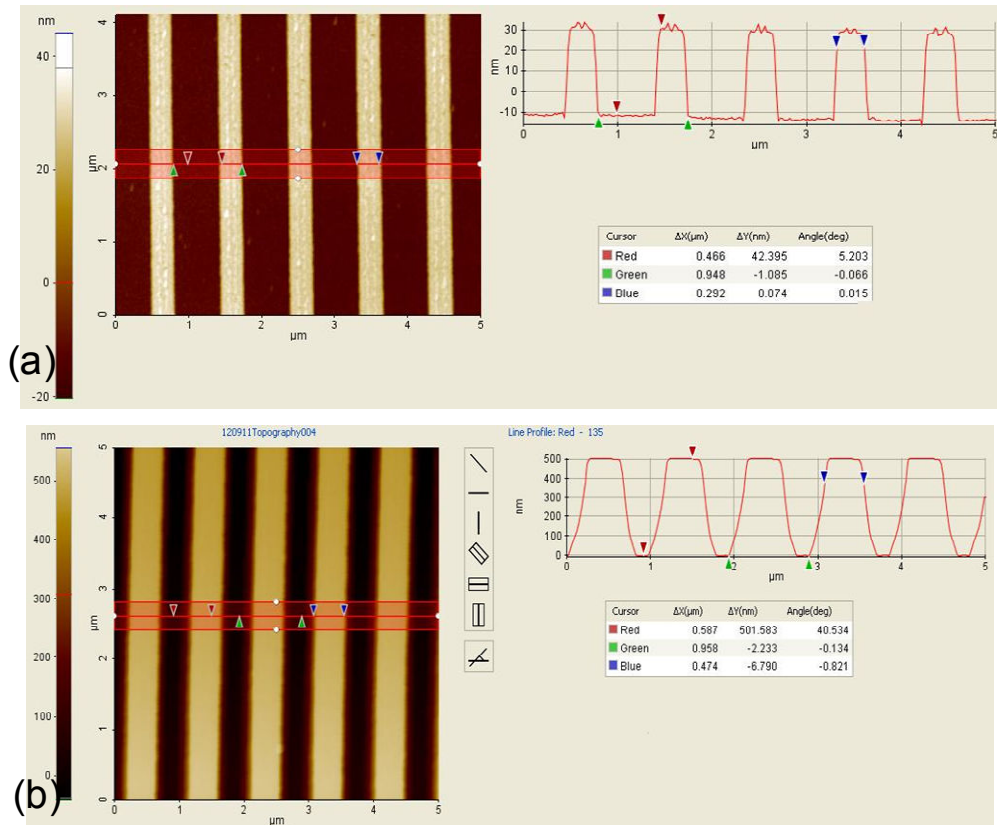
Figure 4-23. AFM images of the (a) 1D Si_3N_4 grating with parameters Λ=948 nm, d_g=42 nm, F_1=0.31 (b) 1D Si grating with Si_3N_4 mask having parameters, Λ=958 nm, d_g=501 nm, F=0.49.

The following Figure 4-24 shows the SEM image of the (a) top view (b) cross sectional view of the grating structure when the gratings are not aligned with the crystal plane.
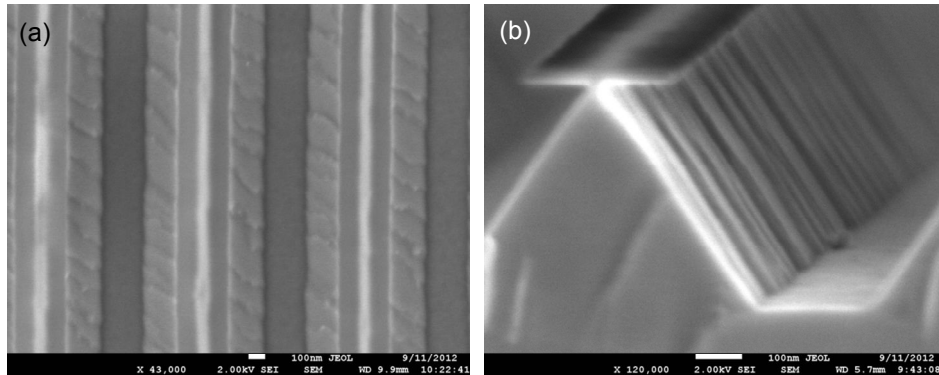
Figure 4-24 SEM images of the (a) top view (b) cross sectional view of the 1D Si grating with Si$_3$N$_4$ mask grating structure, the gratings are not aligned with the crystal plane.

From the figure we see there is a stripe-shaped roughness in the grating ridges. It is because the alignment of Si substrates was not exactly correct, meaning that the crystal plane direction is not perpendicular to the flat side of the SOI wafer. Also the rough sidewall of the mask affects the overall sidewall roughness which can be resolved by reflowing the photoresist mask [66]. Figure 4-25 show the SEM image after correcting the alignment issue; (a) without applying reflow (b) with applying reflow. Figure 4-25 (b) shows the best result for roughness-free gratings with PR reflow.
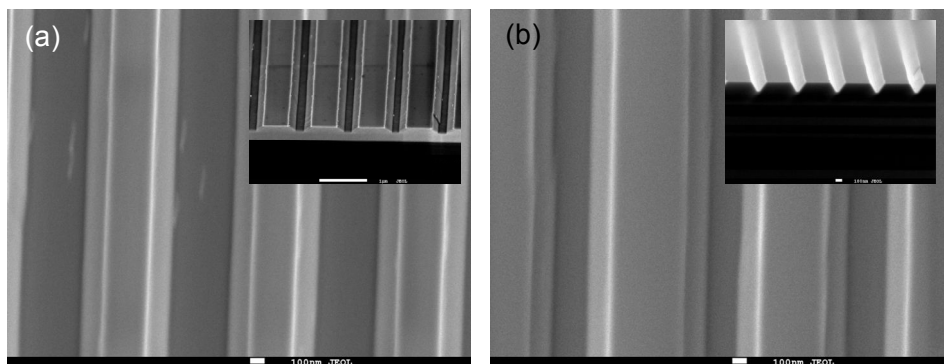
Figure 4-25 SEM image after correcting the alignment issue. (a) Without applying reflow (b) After applying reflow.

4.2.3.3 Initial Design

We have a preliminary design of a GMR transmission filters with trapezoidal structure. But we need to improve the design with symmetric line shape and lower sidebands. The initial design is shown in Figure 4-26
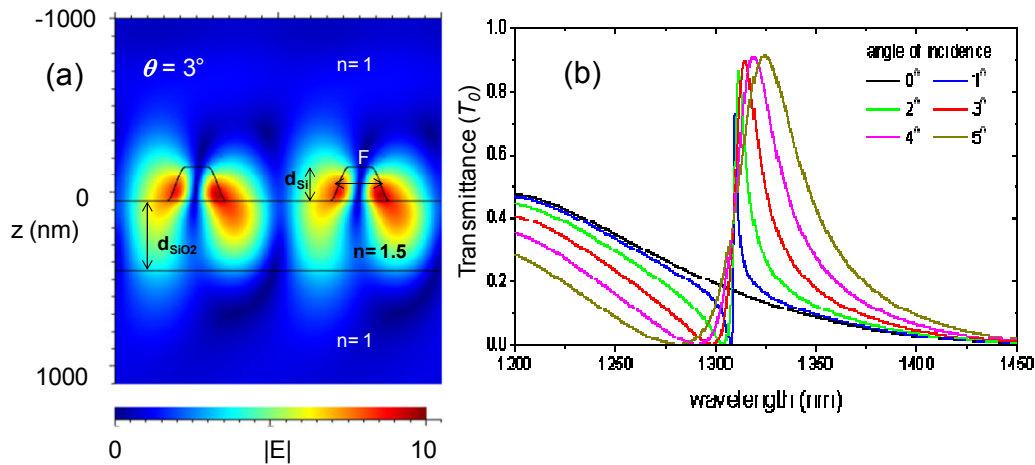
Figure 4-26. Design of the GMR transmission filter with trapezoidal grating structure. (a) field profile at the peak wavelength for θ= 3°. (b) spectral response. Parameters Λ =900 nm, d_{Si}=200 nm, F_{center}= 0.33, d_{SiO2}=400 nm, n= 3.48, and k=0, Angle at base of the trapezoid is 54.7° due to anisotropic etching for (100) Si.

By proper parameter selection we can achieve symmetric shape of a resonance transmission filter with trapezoidal grating structure. That is for future work

4.3 Narrow Band Guided-Mode Resonance Transmission Filters for TM Polarization

In our 2nd TE filter design, field excitations were located very close to the edge of the grating ridge therefore making the design highly susceptible to the irregularities in the sidewalls. A solution to overcome this issue is to design a filter where the modes are confined well inside the grating ridge. The following transmission filter for TM polarization has this characteristic.

4.3.1 Design and Analysis

Figure 4-27 shows theoretical performance of the designed transmission filter. The inset shows the schematic view of the device. The filter consists of a partially etched Si binary grating on top of a silica substrate. Design parameters are homogeneous a-Si film thickness d_{HL} = 170 nm, grating depth d_g = 350 nm ($d_{total}=d_g+d_{HL}$), fill factor F = 0.68, and the grating period Λ = 909 nm. Here, the refractive index of a-Si is assumed to be 3.48 which actually depends on the sputter conditions. With these parameters by our PSO method, we obtain narrow transmission peak with low spread out sidebands as shown in Figure 4-27. The linewidth of the zero order transmission peak at the incident angle θ =1° is 0.5 nm with a theoretical extinction ratio of 17790. Linewidth of the transmission peak depends on the incidence angle as this filter operates at off normal incidence like the 2nd TE design.
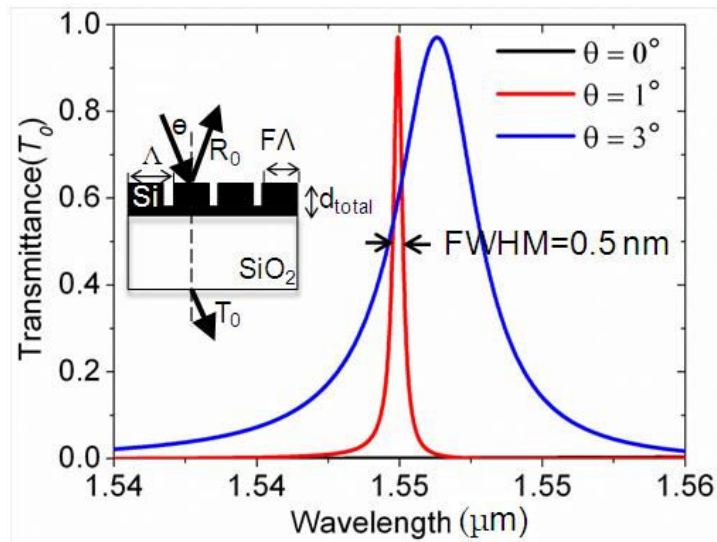
Figure 4-27 Spectral response of optimized GMR transmission filters for TE polarization with parameters d_g= 380 nm, d_{HL}= 170 nm Λ = 909 nm, F = 0.68, n = 3.48, k = 0. Schematic of the structure is shown in the inset.

Like the previously presented designs, we check the robustness of the filter characteristics by calculating the transmission contour map and tolerance matrix considering 3% fabrication error on the structural parameters. Here, the resonance is associate with incidence angle of $\theta = 1°$. Figure 4-28 shows the effect of variation of the layer thicknesses on the zero-order transmission efficiency (T_0).
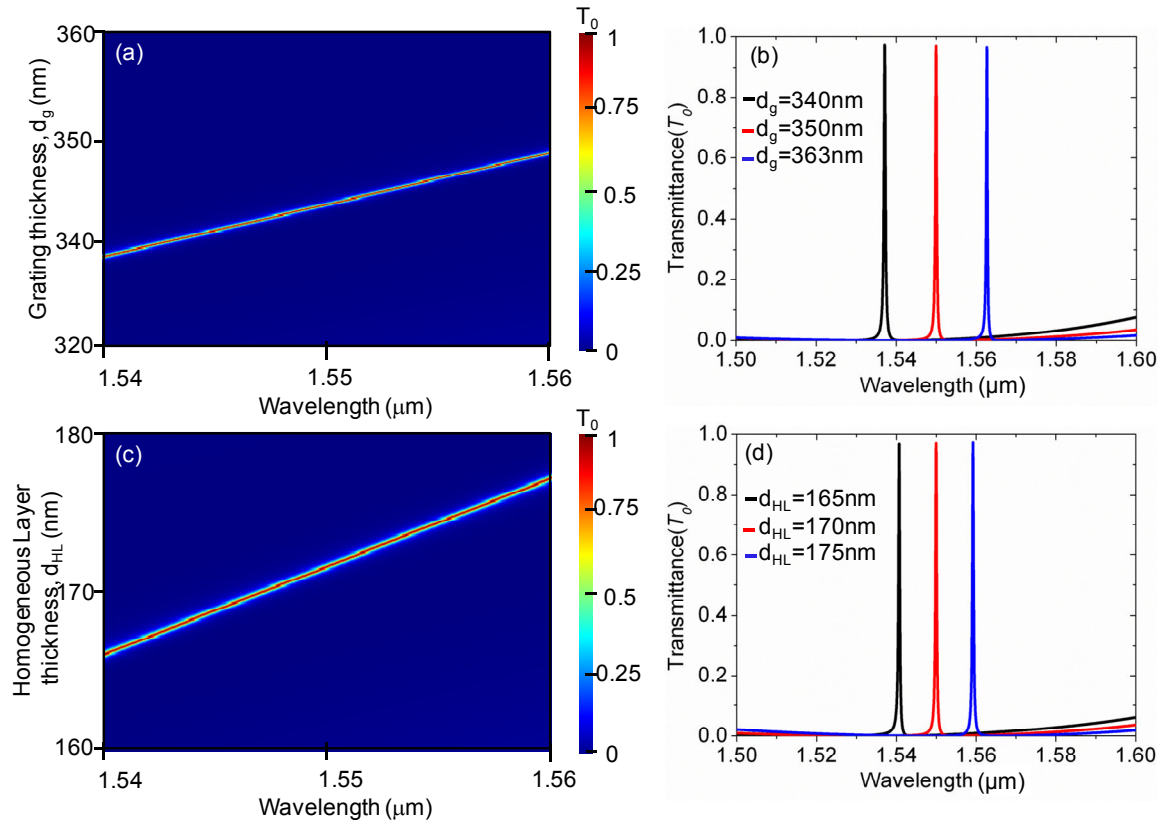
Figure 4-28 (a) Zero-order transmission contour map showing effects of grating thickness (d_g) on the resonance spectra. (b) Response with 3% fabrication error in d_g on the resonance spectra. (c) Zero-order transmission contour map showing effects of homogeneous layer thickness (d_{HL}) on the resonance spectra. (d) Response with 3% fabrication error in d_{HL}.(incidence angle, $\theta = 1°$).

Figure 4-29 shows the effect of variation of the fill factor and grating period resonance spectra. From the figure we see that the grating period has minor effect of the FWHM or the transmission efficiency of the resonance peak but affects the resonance wavelength. From the figures we observe that the resonance linewidth and efficiency are robust against the structural parameters only the position of the resonance peak shifts with the variation of these parameters especially with the grating period.
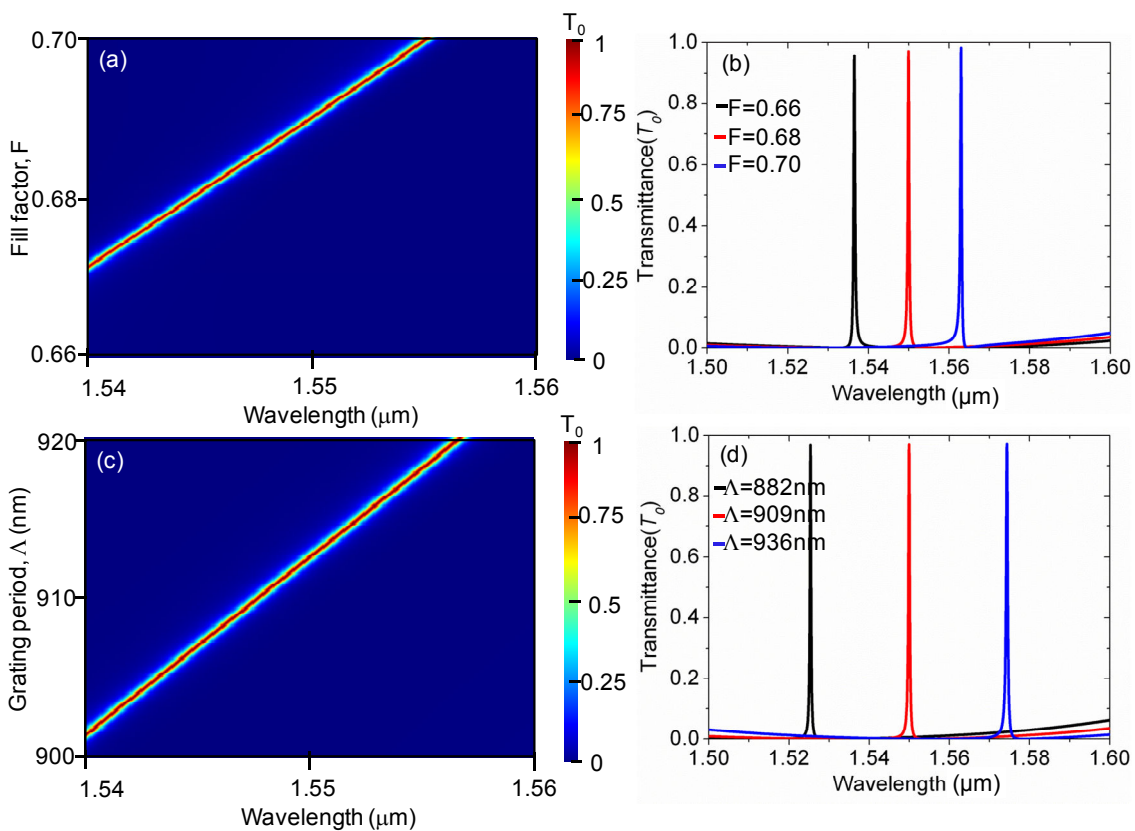
Figure 4-29 (a) Zero-order transmission contour map showing effects of fill factor (F) on the resonance spectra. (b) Response with 3% fabrication error in F (c) Zero-order transmission contour map showing effects of grating period (Λ) on the resonance spectra. (d) Response with 3% fabrication error in Λ (incidence angle, θ =1°).
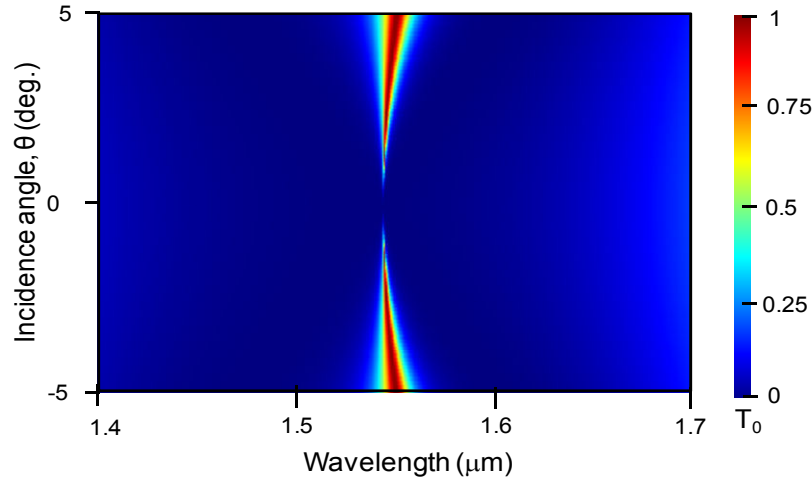
Figure 4-30 Zero-order transmission contour map showing effects of incidence angle on

the resonance spectra.

By observing the angular response of the device in Figure 4-30, we see, at normal incidence there is no resonance. As the angle increases, resonance linewidth starts to increase. The working principle of this filter is same the TE design enabled by the anti-symmetric mode with respect to the mirror symmetry of the device. This phenomenon can be clarified with Figures 4-31. Figures 4-31 (a) shows the coupling orders at the resonance peak (1550 nm) and (b) shows the total internal field corresponds to that transmission peak resonance wavelength of 1550 nm. This resonance is induced by the excitation of a TM_1-like mode at the upper edge of the second stopband [62]. Anti-symmetry of this mode with respect to the mirror symmetry plane of the device yields a vanishingly narrow bandwidth for small incident angles.
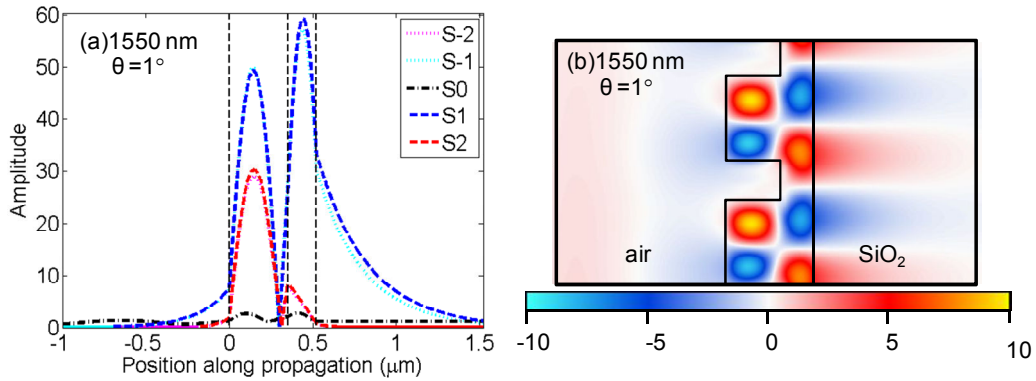
Figure 4-31(a) Coupling orders at the transmission peak resonance wavelength

(1550nm). (b) Total internal field at the same wavelength.

From the total internal field plot shown in Figure 4-31(b) suggests that the resonant excitation of fields for transmission maxima is concentrated well inside the grating ridge making it less sensitive to any irregularity defects on the sidewalls.

4.3.2 Fabrication

The fabrication process of our narrow band GMR transmission filter for TM polarization is the same as presented before for the case of TE design. Similar procedure is maintained starting from depositing a-Si layer of 570 nm on a glass substrate with sputtering system. After annealing, the optical constants of the film are then measured as n = 3.61 and k =0.0013 at 1550 nm by ellipsometer. Next, a ~700-nm-thick negative photoresist layer is spin-coated on the a-Si layer and a UV holographic lithography system is used to pattern a grating of 917 nm period in that photoresist layer. The photoresist layer is then exposed with laser power of 100 mW. After the resist development, curing and descumming, we etch the a-Si layer for 10 minutes 5 seconds in the RIE machine and ash the remaining photoresist mask to get the desired 1D partially

etched Si grating structure. To lower the effect of extinction coefficient we fabricate another device at higher wavelength.

4.3.3 Characterization

The fabricated devices are characterized with both AFM and SEM. Figure 4-32 shows the AFM as well as SEM images of the fabricated devices.
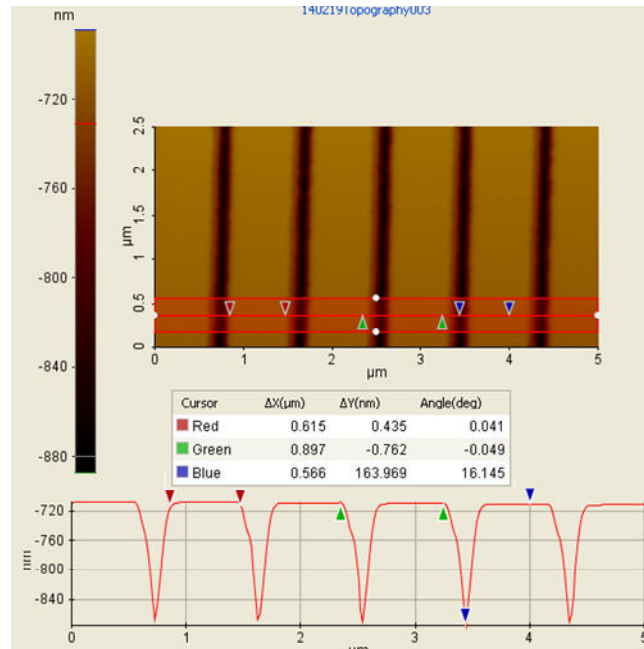
Figure 4-32 AFM image of the fabricated TM device. Parameters: Λ=897 nm, d_g=355 nm; d_{HL}=162 nm, fill factor= 0.685. n= 3.48 at 1550 nm.

From the AFM images of Figure 4-32, we find that the parameters for the TM device. The grating period is ~897 nm. The thickness of the grating layer could not be verified by this image as the AFM tip could not go all the way down to the groove area

due to the high fill factor. The width of the a-Si ridge is ~ 615 nm, therefore the fill factor is ~ 0.685.

For the measurements of the spectral response of these transmission filters we use the same setup used previously described and shown in Figure 4-19. The measured transmission spectra through the TM device show resonance at the incidence angle of 5° and 10°. The device show a qualitative match between the simulation and experimental. We experimentally achieve transmission peak with ~40 nm width and 60% efficiency for the incidence angle of 10°. Even though the position of the resonance peak matches with the fitted simulated result, the efficiency is lower than the theory especially for smaller angles as shown in Figure 4-33.
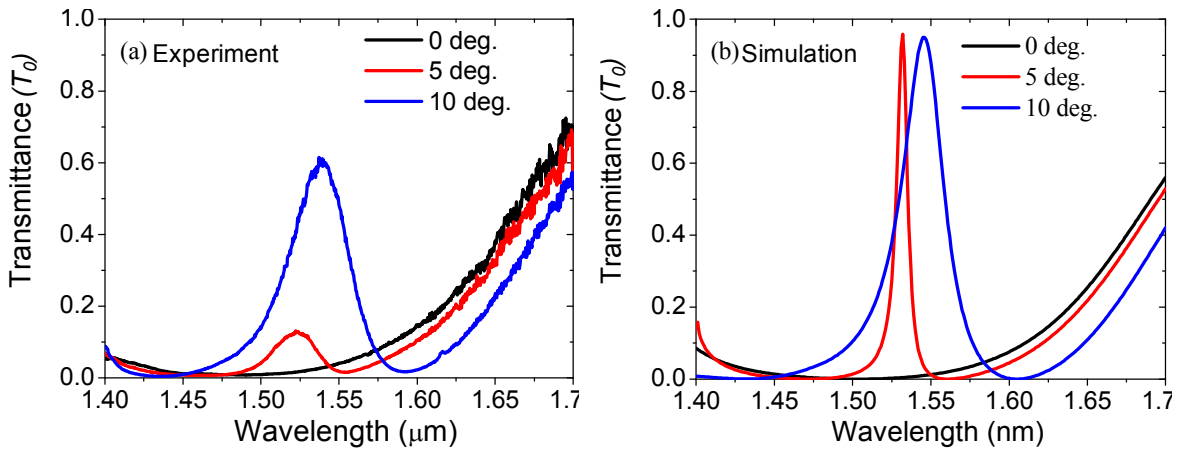
Figure 4-33(a) Spectral response of the fabricated TM device at different incidence angles (b) Simulated response. Simulation parameters are period=897 nm, d_g=355 nm, d_{HL}=162 nm, fill factor= 0.68. We use n= 3.48 at 1550 nm

To have a better spectral response, we fabricated another device with higher grating period so that the resonance operates at higher wavelength thereby affected less by the extinction coefficient. For the 2nd device for Figure 4-34, we find that the grating

period is ~1129 nm, while the thickness of the grating layer could not be verified. The width of the a-Si ridge is ~ 817 nm, therefore the fill factor is ~ 0.73.

Cursor	ΔX(μm)	ΔY(nm)	Angle(deg)
■ Red	1.119	-0.986	-0.050
■ Green	0.817	0.107	0.008
■ Blue	0.405	212.320	27.659
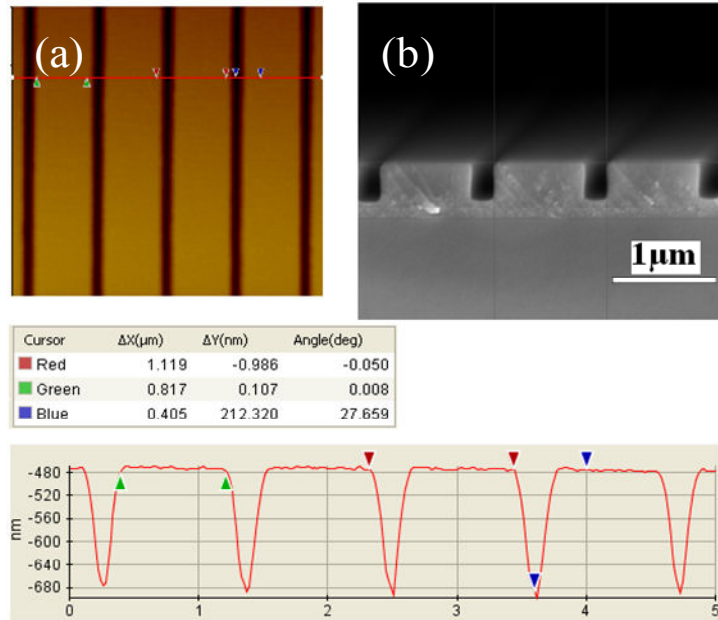
Figure 4-34(a) AFM and (b) SEM images at ×2500 zoom of the fabricated TM device for higher wavelength. Parameters: Λ =1129 nm, d_g=401 nm; d_{HL}=165 nm, fill factor= 0.73.

n= 3.63 at 1550 nm.

The device operating at higher wavelength shows good agreement with numerical calculation because at the higher wavelength the extinction coefficient is lower as shown in Figure 4-35. We have a maximum transmission efficiency of ~85% for the angle of incidence of 10°, but the line-width is close to 80 nm.

We can have smaller line-widths with smaller angle but the transmission efficiency will be lower, since narrower resonance peaks are more susceptible to the extinction coefficient as seen in the case of θ=1°. Here, in Figure 4-35(b) simulated parameters are grating period 1130 nm, grating thickness 405 nm, homogeneous layer

thickness 160 nm, fill factor 0.723. These parameters are based on the AFM and SEM measurements of the fabricated device.
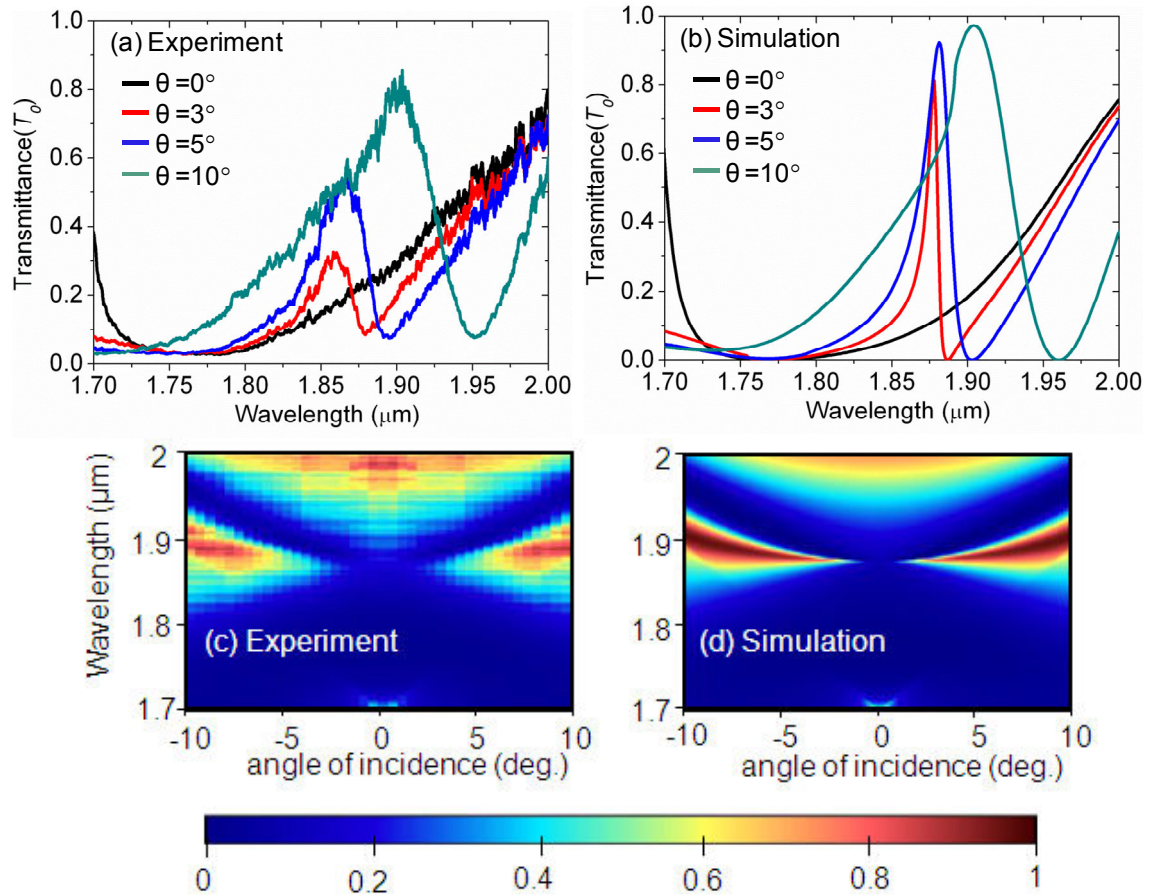
Figure 4-35(a) Spectral response of the fabricated TM device (operating at higher wavelength) at different incidence angles with device parameters Λ=1129 nm, d_g=401 nm, d_{HL}=165 nm, F=0.73 nm, (b) Simulated response with parameters period Λ = 1130, = d_g=405 nm, d_{HL}=162 nm, F= 0.723. n= 3.61 and k= 0.00103 at 1550 nm.(c) Angle-dependent T_0 spectrum in the experiment. (d) Angle-dependent T_0 spectrum found by simulation.
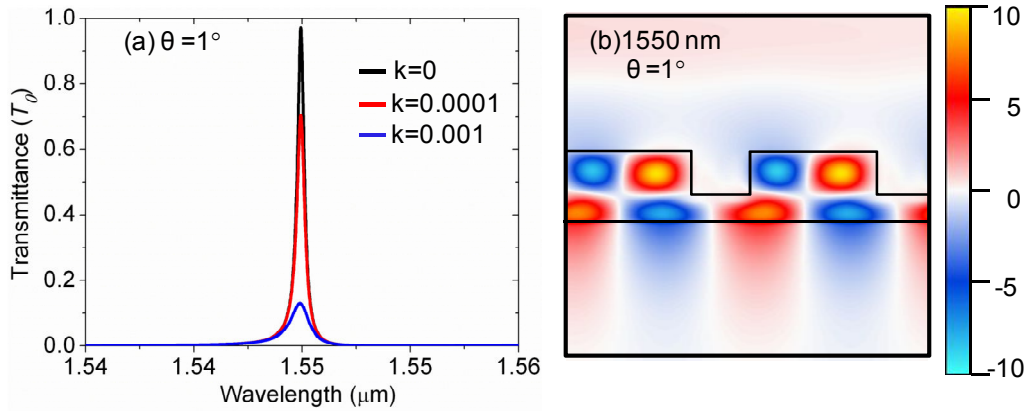
Figure 4-36(a) Effect of extinction coefficient on transmission efficiency at the incidence angle of 1 degree. (b) Field excitation at the grating ridge at resonance wavelength.

From Figure 4-36 we can conclude that the difference in the efficiencies between the experimental and simulated results is mainly due to the effect of extinction coefficient. As the modes at the resonance wavelength reside well inside the grating ridges shown in Figure 4-36(b), the surface roughness should not have much effect on the diffraction efficiency as the extinction coefficient has on it. From Figure 4-36(a), we see with k close to 0.001, the transmission efficiency decreases down to 10%. Also narrower resonances are more susceptible to the k.

4.4 Conclusion

We have designed, fabricated, and tested GMR transmission filters based on Si thin film. Using a powerful optimization method, we have obtained robust design for TE and TM GMR filters against geometrical device parameters. In experimental realization, although we have achieved good agreement of TM devices with theory, but have found that the TE GMR filter enabled by the symmetric mode is highly sensitive to irregularity

defects that degrade resonance shape of the device. Also the efficiency of these narrow band transmission filters is highly affected by the extinction coefficients. To improve the device performance, we must therefore consider material with lower extinction coefficient and fabrication processes for roughness-free grating profile. We show a preliminary result for the roughness-free trapezoidal gratings with chemical etch process with silicon-on-quartz.

Chapter 5

Optical Transmission Filters with Coexisting Guided-Mode Resonance and Rayleigh

Anomaly

5.1 Introduction

In this study, we experimentally demonstrate a GMR transmission filter cooperating with the Rayleigh anomaly in a subwavelength nanograting having a sharp peak and low sidebands. The device consists of a single periodic layer of amorphous Si (a-Si) and operates in the telecommunications band. In our design, the Rayleigh anomaly cooperates with a narrowband GMR to produce extremely sharp profiles in both spectral and angular domains as schematically shown in Figure 5-1. The Rayleigh anomaly with optical resonance effects has been studied in conjunction with surface plasmon resonances [67,68]. Moreover, Magnusson recently proposed a flat-top resonant reflector as a potential application of the Rayleigh anomaly with coexisting GMRs [69]; few other applications of the Rayleigh anomaly are found with the GMR effect. Here, we experimentally realize a GMR-Rayleigh transmission filter and find that the fabricated device shows good agreement with numerical calculations. We provide clear physical explanations of the observed effects.
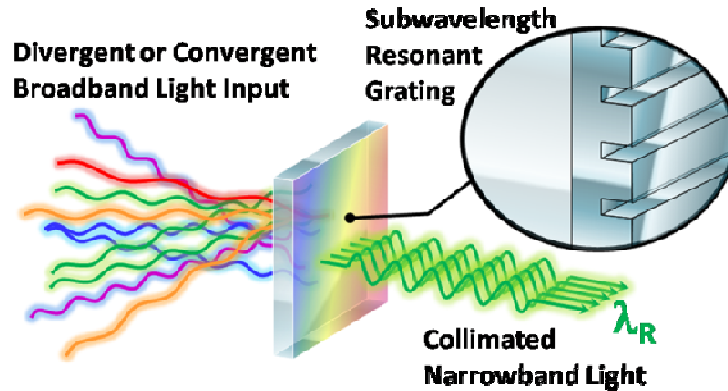
Figure 5-1 Optical transmission filters with coexisting guided-mode resonance and Rayleigh anomaly.

5.2 Design

We design the GMR-Rayleigh transmission filter for transverse magnetic (TM) polarization by using an inverse numerical technique known as particle swarm optimization (PSO) [37]. TM polarization refers to the magnetic field vector normal to the plane of incidence. We use rigorous coupled-wave analysis (RCWA) [38] for numerical evaluation of the GMR filter performance in our PSO algorithm. Figure 5-2(a) shows theoretical performance of the designed filter. The TM filter consists of a silica substrate supporting a partially-etched amorphous Si waveguide grating layer as shown in the inset of Figure 5-2(a). Design parameters are homogeneous a-Si film thickness d_{HL} = 160 nm, grating depth d_g = 405 nm, fill factor F = 0.723, and grating period Λ = 1130 nm. Ellipsometry measurement of our sputtered a-Si films shows the refractive index of a-Si to be 3.61. With these parameters, we obtain a narrow transmission peak at normal incidence. The spectral response at normal incidence for the zero-order transmittance T_0, zero-order reflectance R_0, and first-order transmittance $T_{\pm 1}$ is shown in Figure 5-2(a).

Figure 5-2(b) shows the spectral response for the condition that the GMR and the Rayleigh anomaly are spectrally well-separated.
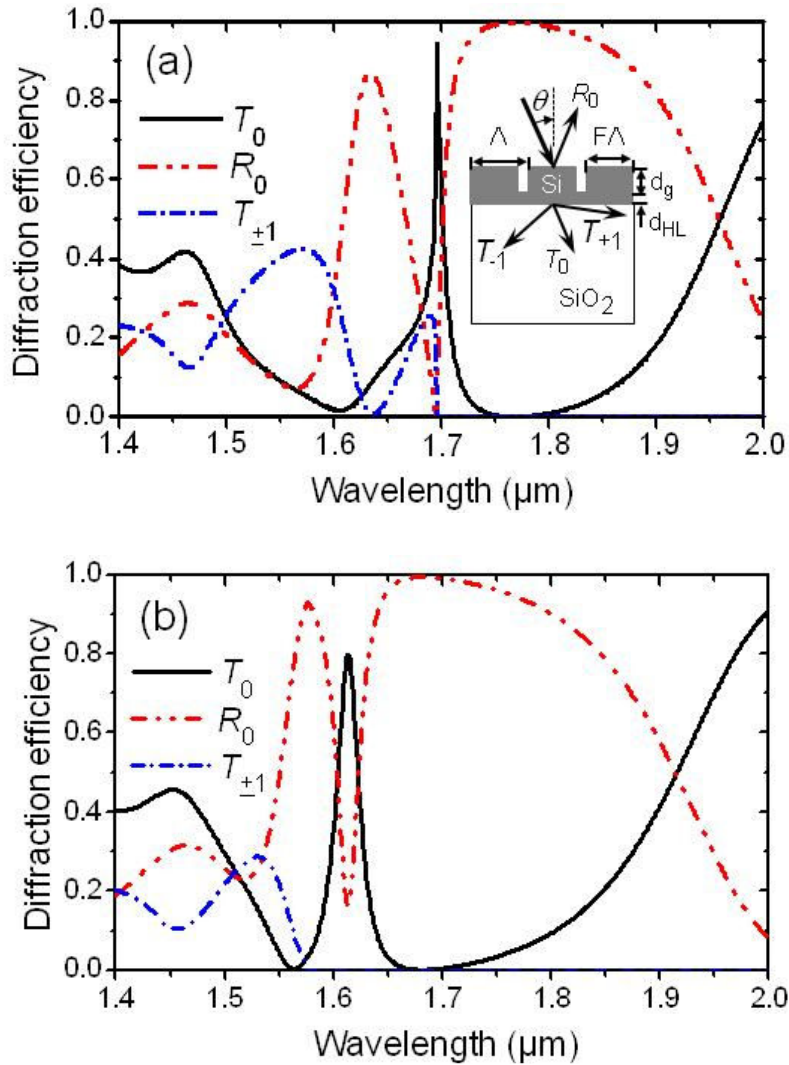
Figure 5-2 (a) Spectral response of the designed filter for TM polarization at normal incidence. Parameters are Λ = 1130 nm, d_g = 405 nm, d_{HL}=160 nm, F=0.723. Inset shows a schematic of the device. (b) Spectral response of the filter when the GMR and the Rayleigh are spectrally separated. Parameters are Λ = 1050 nm, d_g = 405 nm, d_{HL} = 160 nm, F = 0.778.

The sharp transmission peak at the Rayleigh wavelength of 1695 nm in Figure 5-2(a) is induced by a leaky TM_1-like mode as we explain later in this chapter To optimize this design, we can use the period to determine the Rayleigh wavelength and independently tune geometrical parameters such as grating thickness, homogeneous layer thickness, fill factor to establish the GMR wavelength near or at the Rayleigh wavelength. For example, in this design we fix the period to keep the Rayliegh position constant and change the effective index of the waveguide layers (homogeneous layer, grating layer) by changing the layer thicknesses or the grating ridge width. GMR moves to the shorter wavelength as the effective index of the waveguide layer is decreased and vice versa. But the sidebands and the resonance shape will vary as this tuning is very delicate to the design parameters. Figure 5-3(a) shows the effect of change in d_{HL}, d_g and F on the GMR position. We keep the Rayleigh position fixed at 1695 nm determined by the grating period of 1130 nm. As we decrease the effective index of the waveguide layer established by the paramters d_{HL} = 200 nm, d_g = 430 nm, F = 0.78 to d_{HL} = 160 nm, d_g = 405 nm, F = 0.723, the GMR position approaches towards the Rayleigh wavelength. We can also scale these parameters relative to the desired wavelength to design similar devices operating in any wavelength range. Therefore to have the similar GMR-Rayleigh filter functioning at 1550 nm, we first choose the grating period to be 1.034 then we simply scale period, layer thicknesses, and grating ridge width with a factor 1550/1695. . Figure 5-3(b) shows these three examples of GMR-Rayleigh transmission filters operated at 1310 nm, 1550 nm, and 1695 nm. The design parameters enabling a transmission peak at 1310 nm and 1550 nm are given in the Figure 5-3.
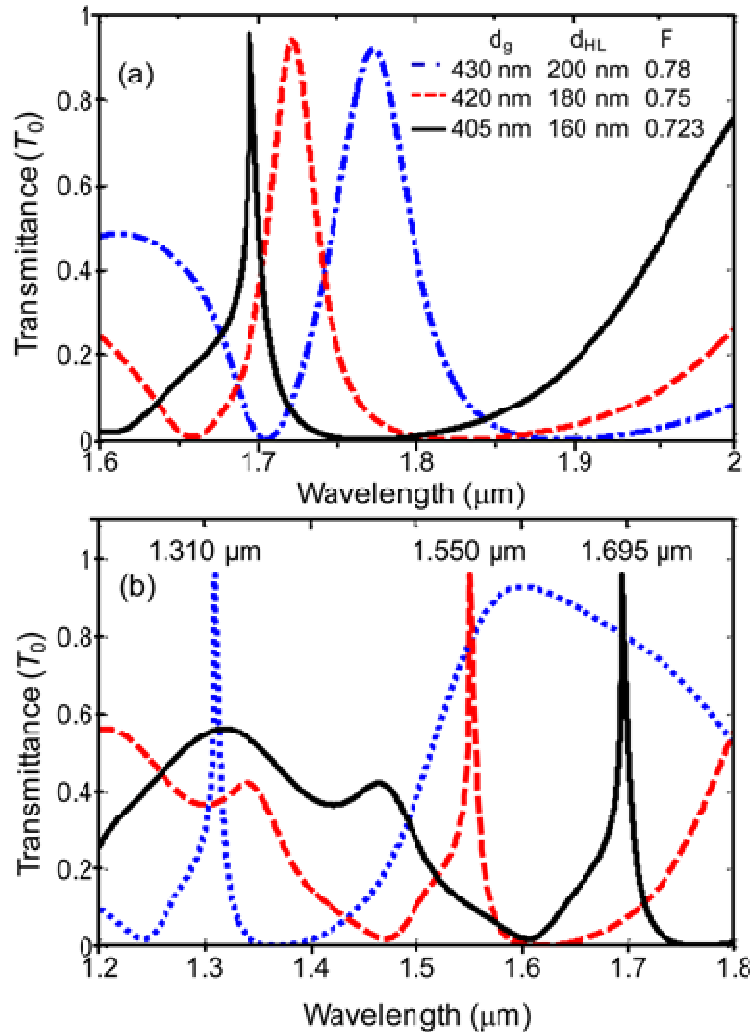
Figure 5-3 (a) Matching GMR and Rayleigh resonances together while keeping the
grating period fixed at 1130 nm. (b) Three examples of the GMR-Rayleigh transmission
filters operated at 1310 nm, 1550 nm, and 1695 nm. Design parameters for transmission
peak at 1695 nm are as shown in Figure 5-2 (a). Design parameters for transmission
peak at 1550 nm are d_{HL} = 146 nm, d_g = 371 nm, F = 0.723, Λ = 1034 nm, n = 3.61, and k
= 0.00103. Parameters for transmission peak operated at 1310 nm are d_{HL} = 124 nm, d_g
= 313 nm, F = 0.723, Λ = 873 nm, n = 3.61, and k = 0.00103.

Our single-layer grating design produces strong modulation to support the excitation of two types of GMRs: one type provides the low-T_0 sidebands while the other type provides the transmission peak. Resonant excitation of a leaky TM_1-like mode by first-order coupling contributes to the low-T_0 background whereas excitation of a leaky TM_2-like mode by second-order coupling produces the transmission peak. This principle based on doubly resonant waveguide gratings was established by Ding and Magnusson [34]. In Figure 5-2(a) regarding the GMR cooperating with the Rayleigh anomaly, the rapid increase in $T_{\pm1}$ induces the sudden decrease of T_0, causing the upper half of the transmission peak at 1.695 μm to be extremely sharp. The Rayleigh anomaly is a salient feature that manifests on periodic surfaces illuminated by incident electromagnetic waves. It refers to the rapid energy redistribution of diffraction orders alternating from evanescent to propagating waves or vice versa [16]. However, in Figure 5-2(b) with a smaller period and the same grating ridge width, the GMR at 1.613 μm is spectrally well-separated from the Rayleigh anomaly at 1.575 μm. The GMR in this case induces a classical Lorentzian line shape with a smooth peak.
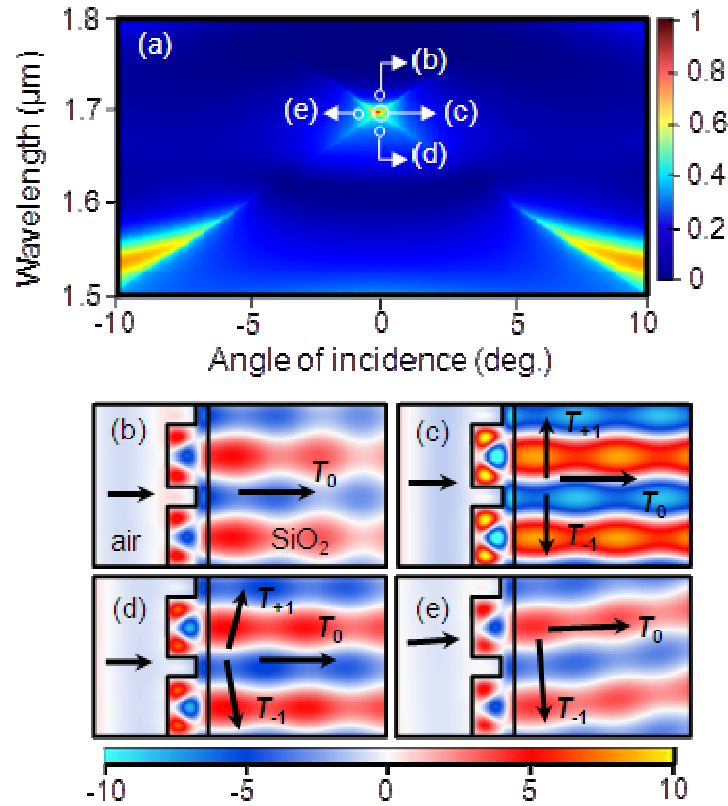
Figure 5-4(a) Experimental angle-dependent T_0 spectrum for cooperating GMR-Rayleigh

(b) Simulated angle-dependent T_0 spectrum for cooperating GMR-Rayleigh. Device

parameters are identical to those of Figure 1(a). (c) Field distributions for several

sampled wavelengths and angles of incidence as indicated in (b).

Figure 5-4(a) shows the angle-dependent T_0 spectrum of the designed GMR-Rayleigh filter. We note that the transmission peak is narrow in both wavelength and angular domains for the latter case. Full-width at half-maximum of the GMR-Rayleigh peak is 10 nm and 0.54° in spectral and angular domains as shown in Figure 5-5(a) and (b), respectively.
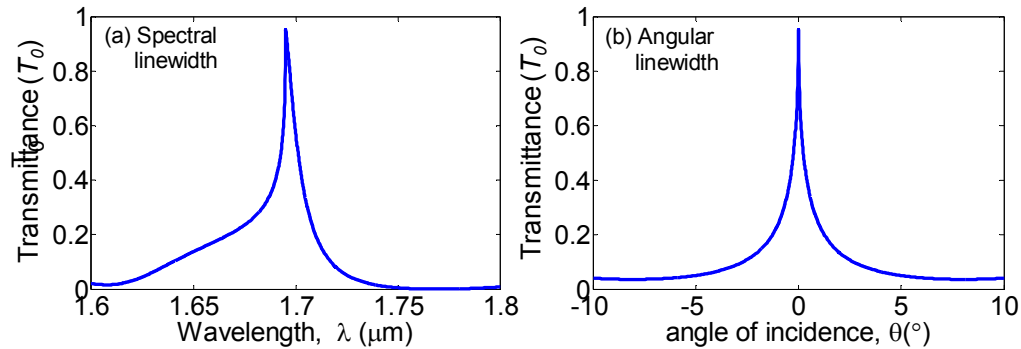
Figure 5-5(a) spectral and (b) angular linewidth of the GMR-Rayleigh device.

The origin of this response with the cooperating GMR and Rayleigh anomaly is understood by strong evanescent near fields and their transition to the propagating diffraction orders. Figures 5-4 from (b) –(d) show magnetic field distributions (normalized by the incident amplitude) at the transmission peak and at slightly detuned conditions as indicated by the arrows in Figure 5-4(a).

In Figure 5-4(b) concerning the longer wavelength vicinity of the transmission peak, there is no higher-order transmission and the tangential standing wave pattern in the SiO_2 substrate is evanescent. Being a part of the excited guided mode, this evanescent tail grows as the wavelength approaches the exact resonance condition as shown in Figure 5-4(c) . The evanescent tail of the guided mode is much stronger than the incident field amplitude, and the Rayleigh anomaly switches it to ±1 propagating orders. Therefore, the ±1 propagating orders abruptly increase as shown in Figure 5-4(a). In Figure 5-4(d) regarding the shorter wavelength vicinity of the transmission peak and in Figure 5-4(e) concerning the non-zero angle of incidence, we notice strong transmitted first-orders ($T_{\pm1}$) that render a rapid decrease in the zero-order transmission; this forms the sharpened T_0 efficiency response.

5.3 Fabrication

We fabricate the designed GMR-Rayleigh transmission filter. Using a radio-frequency sputter system, we first deposit a 570-nm-thick a-Si film on a microscope slide. The deposited a-Si film is annealed at 490°C for 10 min. to lower the extinction coefficient (imaginary part of the refractive index). The extinction coefficient of the a-Si film at wavelength 1.7 μm changes from 1.17×10^{-2} as deposited to 0.94×10^{-4} after annealing. We expect the emergence of nanocrystalline domains to cause the reduction of the extinction coefficient. During annealing, the a-Si thickness also shrinks from 570 nm to 561 nm. Using holographic lithography, we produce grating patterns in a photoresist mask layer on a-Si film. Then by using a deep UV laser at wavelength 266 nm, we achieve the exact fill factor of the grating by finely tuning the exposure energy. This photoresist grating is then cured and used as a mask to etch through the a-Si layer by reactive-ion etching. The a-Si layer is partially etched in a SF_6/CHF_3 gas mixture, and the remaining photoresist mask is removed in O_2 plasma. Finally, the designed waveguide grating structure is experimentally obtained. Figure 5-6 shows schematic diagram of the processing steps involved in the fabrication of this device.
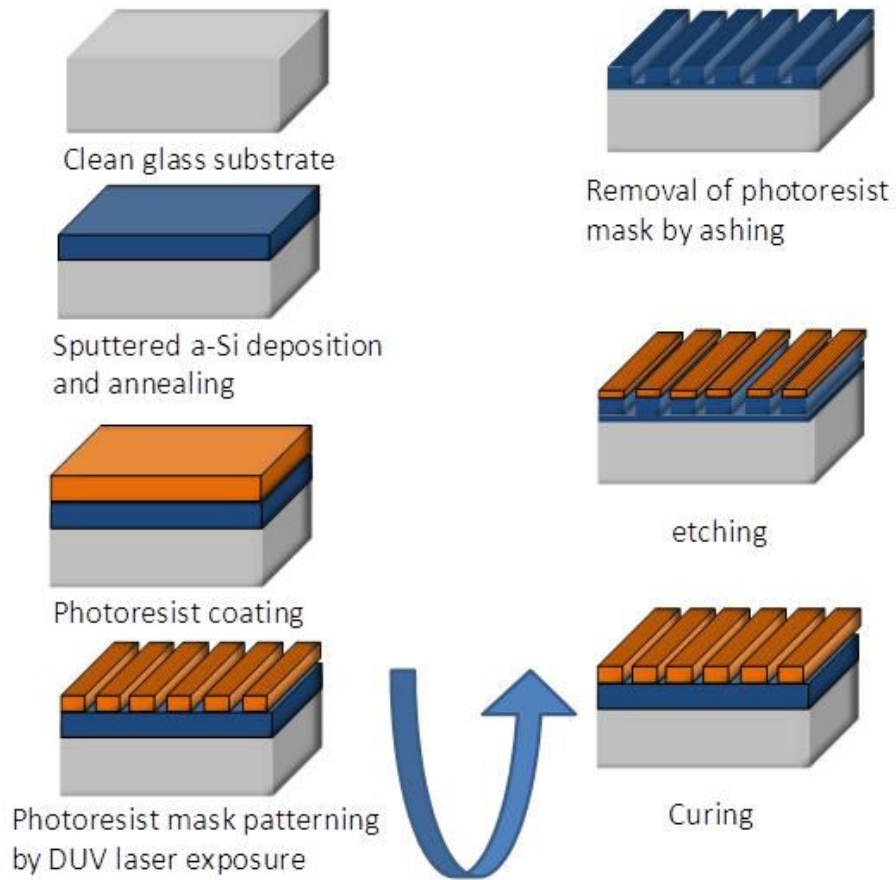
Figure 5-6 Schematic view of the fabrication steps.

The fabricated device is observed with a scanning electron microscope (SEM) as shown in Figure 5-7(a) and (b). From the top-view and cross-sectional SEM image analysis, we confirm that the fabricated device is uniform with the following parameters (including estimated errors): Λ= 1129$\pm$4 nm, d_g = 401$\pm$3 nm, d_{HL} = 160$\pm$3 nm, and F = 0.723$\pm$0.003.
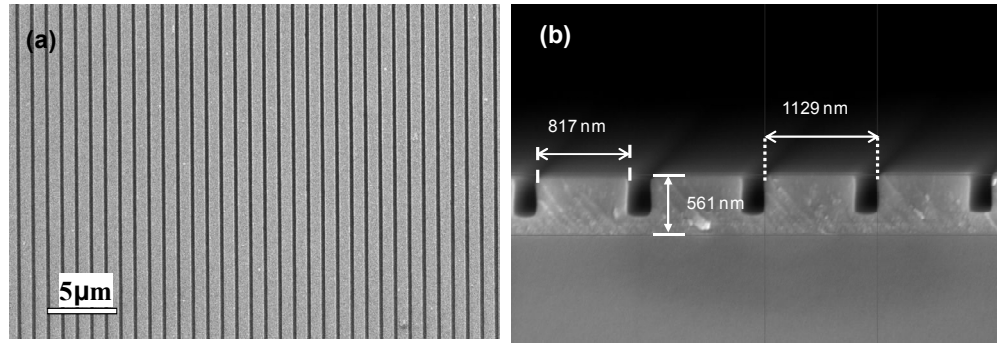
Figure 5-7 (a)Top-view and (b) cross-sectional SEM images of the fabricated device.

5.4 Characterization

Next, we measure the angle-dependent T_0 spectrum. Figures 5-8(a) and 5-8(b) show good agreement between the measurements and numerical results. For the measurements, we use an optical spectrum analyzer covering the 1.2–2.4 μm wavelength range and a super-continuum source for broadband incident light. The incident angle is finely controlled with a motorized rotation stage with resolution of 10^{-3} degrees.
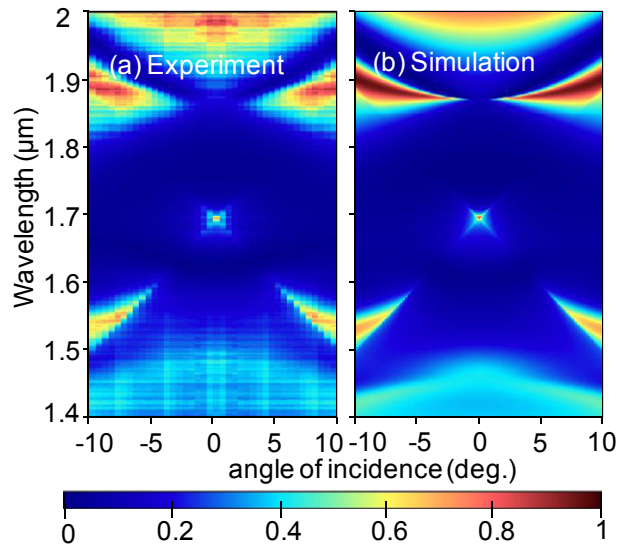
Figure 5-8(a) Angle-dependent T_0 spectrum in the experiment. (b) Angle-dependent T_0 spectrum found by RCWA calculations.

We compare profiles of measured spectra with RCWA calculations for several sampled angles (θ) of incidence in Figure 5-9; two major resonance features at 1.695 μm and 1.88 μm appear in both the experimental Figure 5-9(a) and calculated Figure 5-9(b) results. The sharp feature at 1.695 μm is the cooperating GMR-Rayleigh peak and clearly appears in the experimental profile for θ = 0°. We note that this extremely sharp transmission peak can be fairly tolerant to the material absorption and film imperfections. In general, for a high-Q resonance, the intrinsic material absorption and random scattering caused by rough features and grain boundaries profoundly influence the resonance efficiency since the resonant mode is well-localized and has a long lifetime. In contrast, the sharp feature in this case is not induced by a high-Q resonance excitation; instead, it is formed by the abrupt release of resonant energy to the higher-order diffraction at the Rayleigh condition.
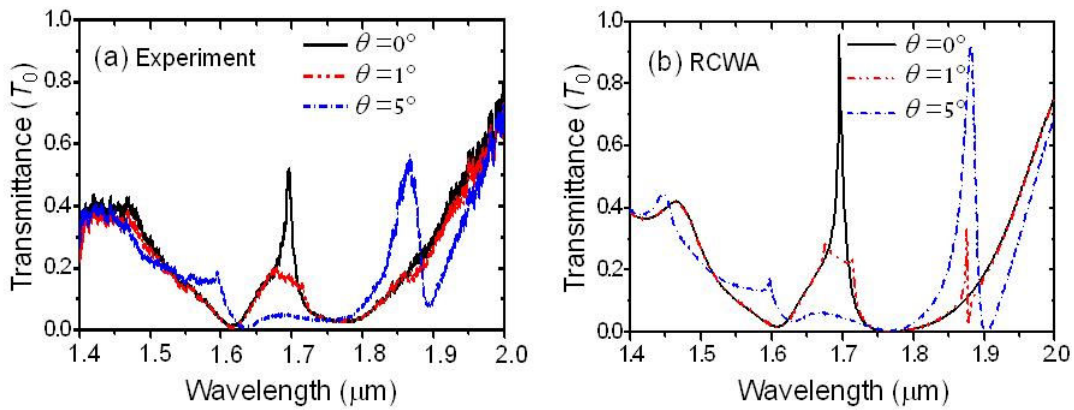
Figure 5-9 Zero-order transmission spectral response of the fabricated TM device due to (a) experiment with device parameters Λ=1129 nm, d_g=401 nm, d_{HL}=160 nm, F=0.723 and (b) simulation with parameters Λ =1130 nm, d_g=405 nm, d_{HL}=160 nm, F=0.723.

The resonance feature at 1.88 μm also shows a very sharp transmission peak for a small non-zero angle of incidence (θ=1°), and the feature gets broader for a larger angle of incidence θ =5°) as shown in Figure 5-9. In the experimental spectra displayed in Figure 5-9(a), however, this sharp resonance feature for θ =1° is unclear while the broader resonant peak for θ =5° is clearly observed. This resonance feature is induced by the excitation of a TM$_1$-like mode at the upper edge of the second stopband [62,70]. Anti-symmetry of this mode with respect to the mirror-symmetry plane of the device yields vanishingly narrow bandwidth for small incident angles; thereby, the mode is extremely sensitive to the material absorption or random scattering resulting from film imperfections. We consider this to be the reason for the difficulty of the experimental demonstration of this GMR transmission peak. This type of transmission resonance is generally induced in wideband reflection gratings under off-normal incidence as described previously [61].

5.5 Conclusion

In summary, we present a comprehensive theoretical and experimental study of GMR transmission filters with coexisting Rayleigh anomaly. Theoretical analysis provides angle-dependent diffraction efficiencies and associated field distributions showing that the guided-mode excitation enhances critically evanescent diffraction orders at the Rayleigh threshold. These diffraction orders abruptly release GMR-confined optical energy to the far field and contribute to the formation of an extremely sharp peak. We precisely fabricate the designed GMR-Rayleigh transmission filter, and the measured spectral and angular responses show good agreement with the numerical calculations. The GMR-Rayleigh transmission peak is fairly tolerant to material absorption and fabrication imperfections as it does not require an extremely narrow resonance bandwidth for a sharp spectral profile.

Chapter 6

Fabry-Perot Based Transmission Filters with Wide Band Guided-Mode Resonant

Reflectors

6.1 Introduction

Periodically patterned subwavelength grating films exhibit strong resonance effects originating in quasi-guided, or leaky, waveguide modes. This resonance provides sharp variations in the intensity reflection or transmission spectra due to the coupling of external radiation to the leaky modes of the grating [1-6]. Much attention has been drawn by these kinds of structures for their interesting physical characteristics, simple structures and associated application possibility such as filters, sensors, polarizers, laser mirrors, as discussed in the literature [1-10]. Most research so far has been done on reflection type filters while transmission type GMR filters are less realized. However, it is generally difficult to realize transmission filters based on GMR. In addition, it is challenging to obtain low transmission background with a single, transparent dielectric layer [34]. In this study we place two broadband GMR reflectors [71, 72] facing each other with an air gap to form a Fabry-Perot cavity and thus show narrow transmission passbands with certain free spectral range depending on the air gap between the two GMR mirrors (cavity length).

Here we design, fabricate and characterize transmission filters based on wideband guided-mode resonance (GMR) reflectors constituting a Fabry-Perot cavity. Fabry-Perot(F-P) cavities consists of two mirrors aligned perfectly parallel to each other and separated by a length specified as cavity length. Lighwave reflections between the two mirrors lead to resonance and narrow transmission peak across the cavity depending on the reflectivity and alignment of those mirrors. Typically these F-P mirrors are

fabricated from thin metallic coatings or Bragg reflectors which provides efficient reflection through a broad spectrum [73, 74]. In this research we use wide band GMR reflectors to design and fabricate these narrow band transmission filters. There have been some theoretical reports on the Fabry-Perot devices incorporating grating structures [75,76,77,78,], but experimental realization of this kind of filter has not been put forward yet.

6.2 Design

The physical basis of a transmission filter incorporating two wide band guided-mode resonant reflectors facing each other is, when the air gap between the two low Q or broadband mirrors becomes greater, the evanescent coupling between the two GMR elements becomes weaker, therefore spectrum becomes immune to the horizontal alignment of the two gratings [77]. The device can work as a Fabry-Perot cavity and provide multiple resonance transmission peaks. By changing the cavity length we can easily tune the spectral position of these transmission peaks. We first design each wide band GMR reflection filters for transverse electric (TE) polarization by using an inverse numerical technique known as particle swarm optimization (PSO) [37]. We use rigorous coupled-wave analysis (RCWA) [38] for numerical evaluation of GMR filter performance in our PSO code. Then we place these reflectors in the simulation facing each other with an air gap of or more than 1μm to form the overall F-P structure. Here in this case, the coupling becomes weak after ~500 nm air gap. Figure 6-1 show the schematic diagram of the F-P based GMR transmission filter and the spectral response of the designed filter for TE polarization at normal incidence.
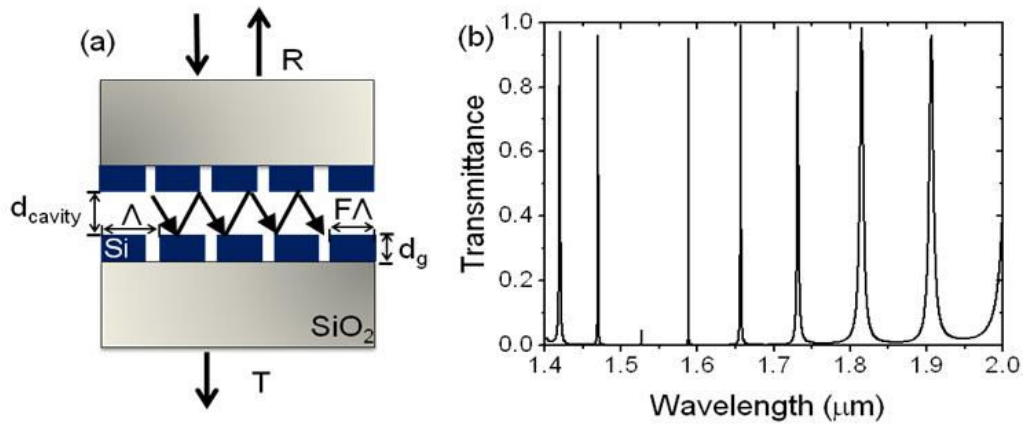
Figure 6-1 (a) Schematic diagram of the F-P based GMR transmission filter. (b) Spectral response of the designed filter for TE polarization at normal incidence. Parameters are Λ = 939 nm, d_g = 200 nm, d_{cavity}=180 μm, F=0.34.

By decreasing the cavity length d_{cavity} and increasing the reflectance, we can easily form a narrow band transmission filter with broad low sidebands. Figure 6-2 shows the spectral response for different cavity lengths of 10 μm and 50 μm. Figure 6-3 shows the zero-order transmission contour map providing the effect of cavity length change on the resonance spectra.
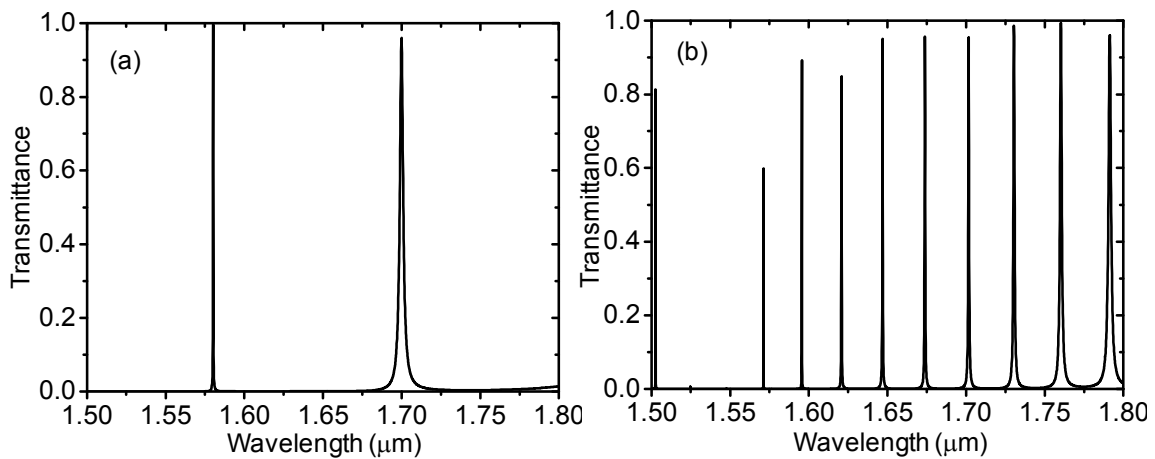
Figure 6-2 Spectral responses of the designed filter for TE polarization at normal incidence for different cavity lengths (a) 10 μm (b) 50 μm.
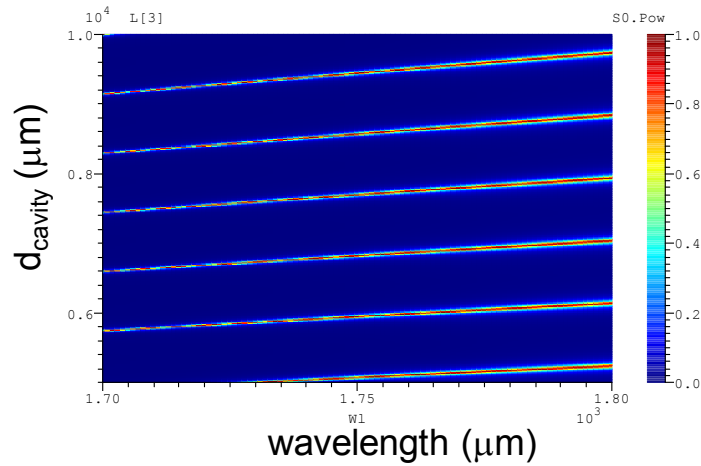
Figure 6-3 Zero-order transmission contour map showing effect of cavity length change on the resonance spectra.

6.3 Fabrication

The fabrication process of our narrow band GMR transmission filter is presented as follows. First a layer of amorphous Si is deposited on a glass substrate with the AJA sputtering system with the sputter pressure of 5mT for 4500 s. After a-Si layer deposition, we anneal the a-Si layer on a rapid thermal annealing system (Jet First RTA) at 490°C for 10 minutes to improve the optical constants, i.e., lower the extinction coefficient almost an order from the As-deposited a-Si. The thickness and the optical constants are measured with an ellipsometer. For the film thickness of 204 and 187 nm for two samples, the optical constants are measured as n = 3.63 and k = 0.001 at 1550nm. To produce a grating pattern, we use UV holographic lithography on 380-nm-thick positive photoresist coated a-Si layer. Specific fill factor of the grating is achieved by controlling UV exposure time. The photoresist layer is exposed for 85 s with laser power of 150 mW. This photoresist grating is then cured at 130°C for 13 minutes as an

etch mask for the reactive ion etch (RIE) through the a-Si layer. The a-Si layer is then etched for 5 minutes and 40 seconds with SF_6/CHF_3 gas mixture operated on a RIE system which transfers the photoresist pattern on the a-Si layer. The remaining photoresist mask is removed by ashing with O_2 plasma. Finally, the single layer waveguide grating structure is achieved. Figure 6-4 shows a schematic diagram of the general fabrication steps for these transmission filters and Figure 6-5 shows the schematic and the actual image of the fabricated device.
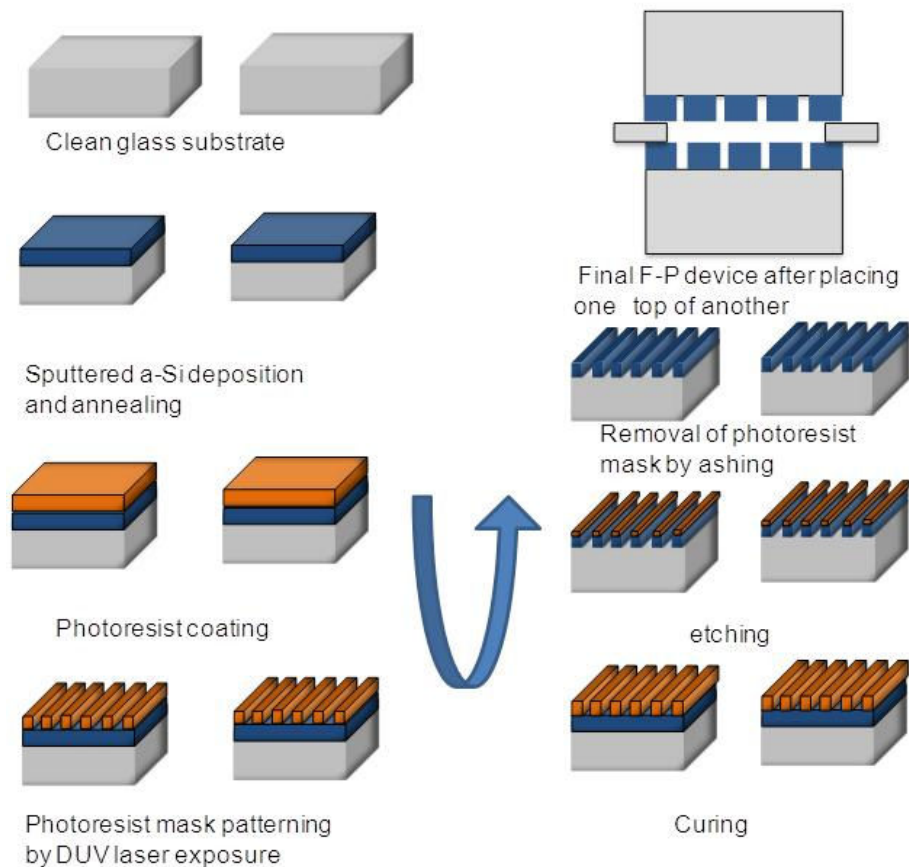
Figure 6-4 Schematic view of the fabrication steps.
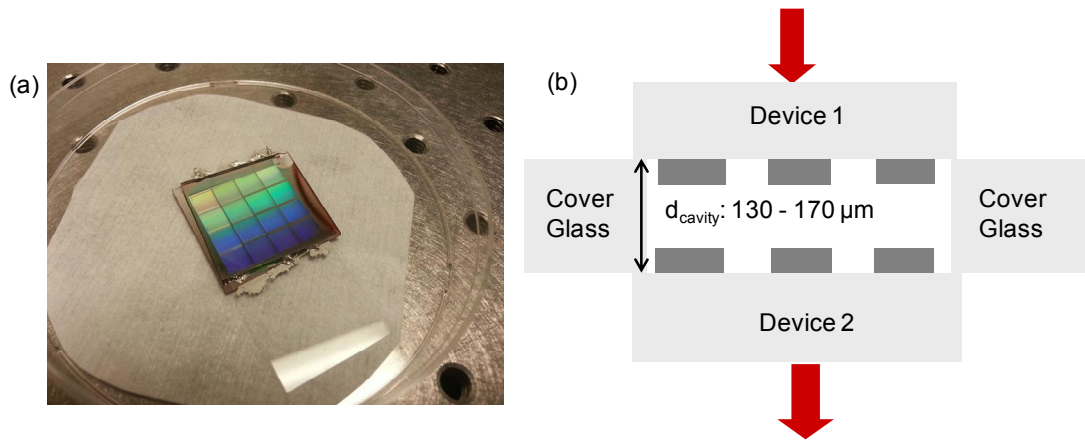
Figure 6-5 (a) Schematic view and (b) actual image of the fabricated device.

6.4 Characterization

The fabricated devices are characterized with atomic force microscopy (AFM). Figures 6-6 and 6-7 shows the AFM images along with the transmission spectral response of the fabricated devices. From the AFM images of Figures 6-6(b) and 6-7(b), we find that the parameters for the TM device are as follows, for the top mirror, grating period, Λ_1 = 927 nm, grating thickness, d_{g1}=187 nm, fill factor, F_1=0.36, n=3.63, k= 0.001. the cavity length , d_{cavity}=220 µm , and for the bottom mirror, grating period Λ_2 = 927 nm, grating thickness d_{g2}=204 nm, fill factor F_2=0.32. From Fig 6-6(a) and 6-7(a), we find that from 1450 nm 1650 nm both mirrors have low transmittance.

(a)

(b)

Figure 6-6 (a) Zero-order transmission spectral response of the fabricated device (b) AFM image with device parameters Λ_1 = 927 nm, d_{g1}=187 nm, F_1=0.36, n=3.63, k= 0.001.

(a)

(b)
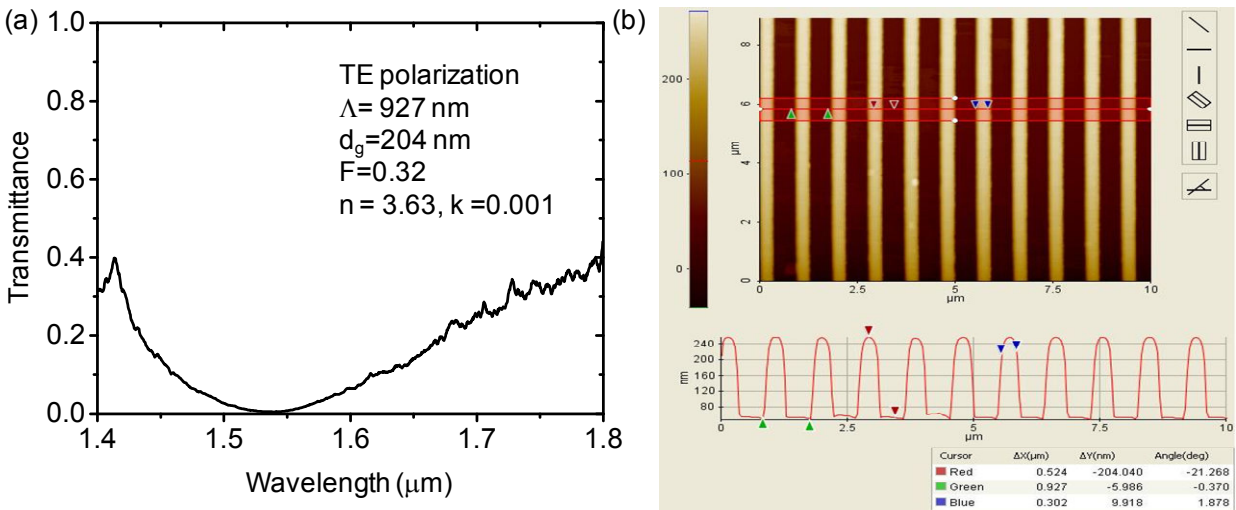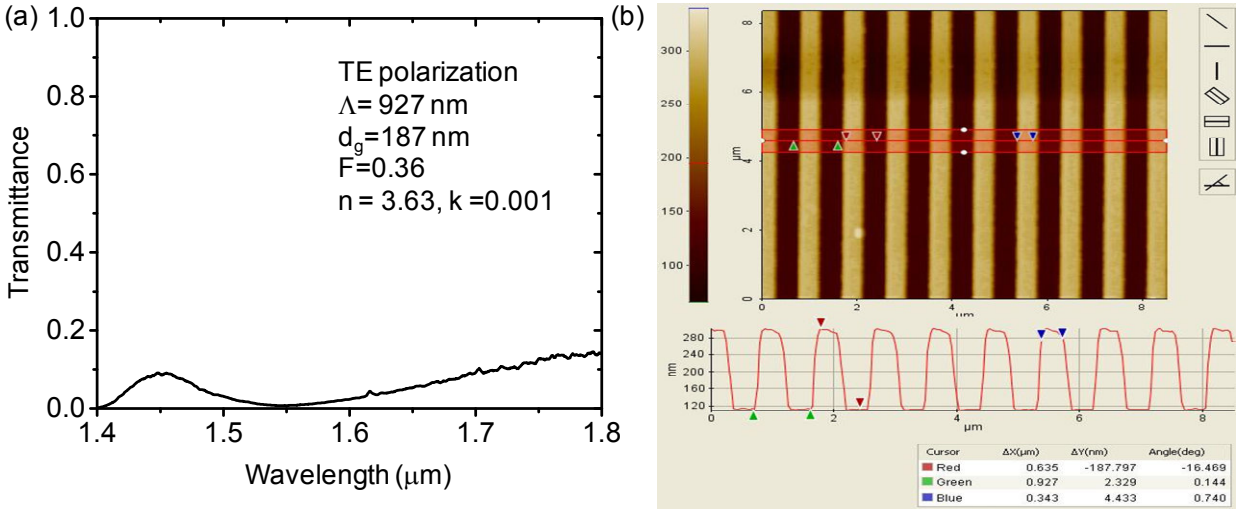
Figure 6-7 a) Zero-order transmission spectral response of the fabricated device (b) AFM image with device parameters Λ_2 = 927 nm, d_{g2}=204 nm, F_2=0.32, n=3.63, k= 0.001.

For the measurements of the spectral response of these transmission filters we built a setup schematically illustrated in Figure 6-8. The angle of incidence is controlled

by the rotation stage where the sample is placed and the stage is operated by a Labview program. An angular resolution of 0.001 degrees can be achieved by this automated system. To set the polarization state, a polarizer is used before the sample stage. The transmitted beam is then measured with an optical spectrum analyzer for a wavelength range of 1400 nm to 2000 nm in 1 nm steps.
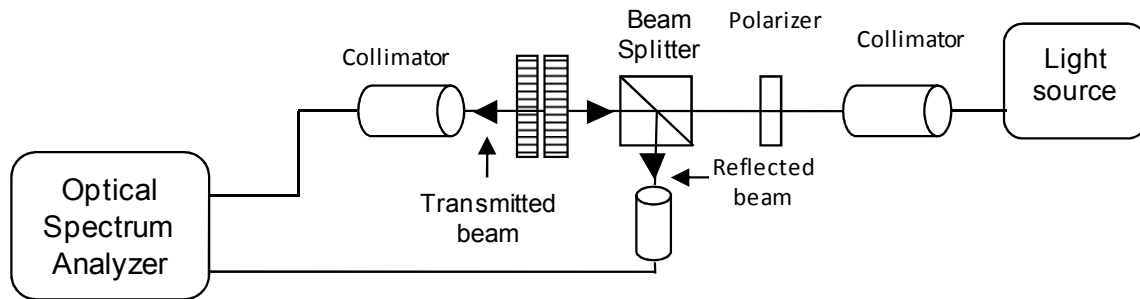
Figure 6-8 Schematic view of the optical measurement setup.

The measured transmission spectra through the TE device along with the simulated results are shown in Figure 6-9 and Figure 6-10. From Figure 6-10, we have a maximum transmission efficiency of ~ 50% at 1765 nm and the line-width is close to ~3 nm. The free spectral range (FSR) is ~7 nm. At around range 1500-1600 nm, we should observe very narrow transmission peaks as that range has very high reflectance but that narrow peak is very susceptible to extinction coefficient, k. Besides that, the F-P device transmission efficiency also depends on the parallelism of the two mirrors. Our cover glass thicknesses vary from 130 μm – 180 μm. So that can also affect the efficiency. We can have transmission peak with broader low sidebands by increasing the FSR which is caused by changing the cavity length. Figure 6-10 shows a qualitative match between the experiment and simulation. Theoretical calculation FSR is ~ $\lambda^2 / 2n_f d$ = $1.5^2/2*0.18$= 6.67 nm which is close to the experimental result. Here, simulated parameters are Λ_1=927 nm,

d_{g1}=187 nm, d_{cavity}=220 µm, F_1=0.36 and $\Lambda 2$=927 nm, d_{g2}=204 nm, F_2=0.32. These parameters are based on the AFM measurement of the fabricated devices.
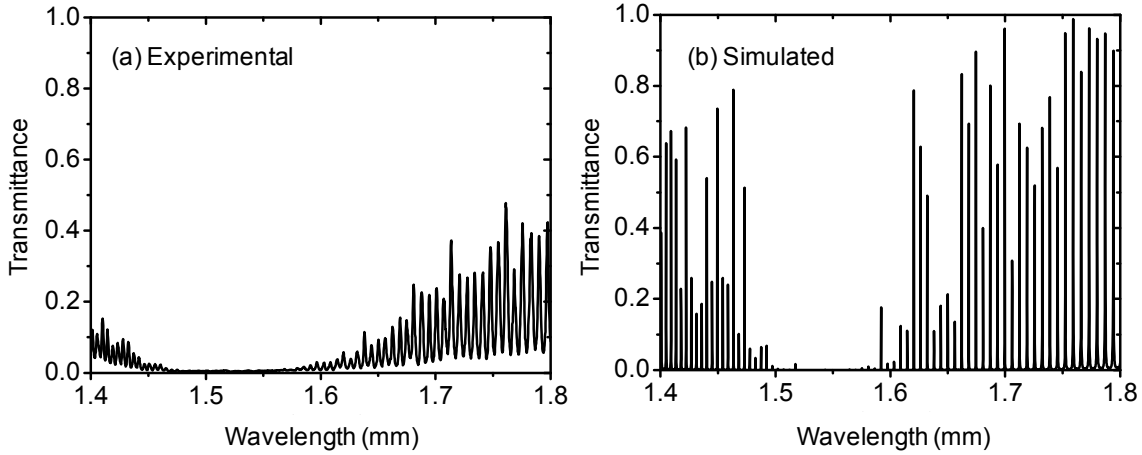
Figure 6-9 Zero-order transmission spectral response of the fabricated device due to (a) experiment with device parameters Λ_1=927 nm, d_{g1}=187 nm, d_{cavity}=170 µm, F_1=0.36 and Λ_2 = 927 nm, d_{g2}=204 nm, F_2=0.32, n=3.63, k= 0.001. (b) simulation with parameters Λ_1=927 nm, d_{g1}=187 nm, d_{cavity}=220 µm, F_1=0.36 and Λ_2 =927 nm, d_{g2}=204 nm, F_2=0.32.
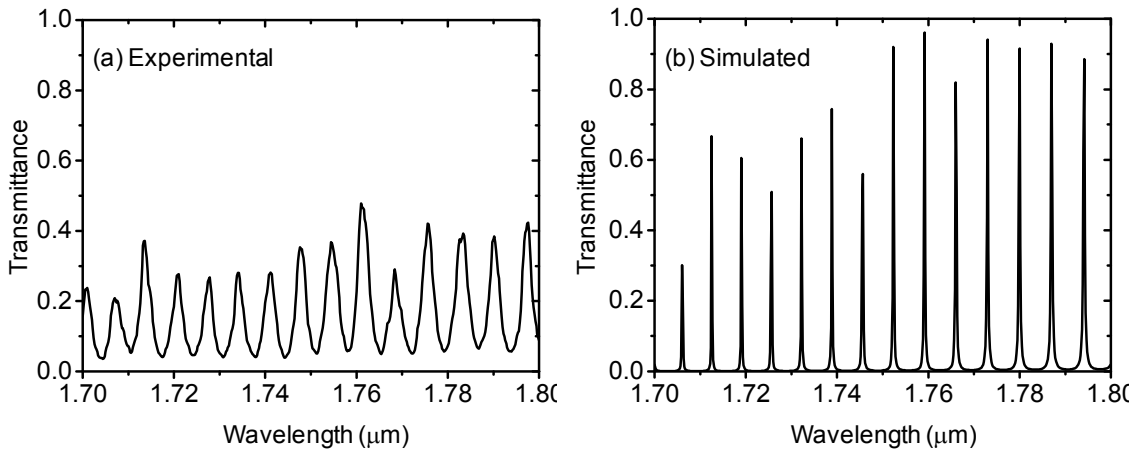
Figure 6-10 Zero-order transmission spectral response of the fabricated device in the range 1700-1800 nm due to (a) experiment with device parameters Λ_1=927 nm, d_{g1}=187 nm, d_{cavity}=170 µm, F_1=0.36 and Λ_2=927 nm, d_{g2}=204 nm, F_2=0.32, n=3.63, k= 0.001 (b)

simulation with parameters Λ_1=927 nm, d_{g1}=187 nm, d_{cavity}=220 μm, F_1=0.36 and $\Lambda2$=927 nm, d_{g2}=204 nm, F_2=0.32.

6.5 Conclusion

In summary we report an experimental analysis of a GMR transmission filter based on a Fabry-Perot cavity. Even though the efficiency of the resonance peak is not high we can improve the result by using a low loss material such as crystalline silicon and fashion broad low sidebands by decreasing the cavity length with a micro-control translation stage.

Chapter 7

Future Directions

Future research in guided-mode resonance transmission filters will be oriented towards realizing experimental results with improved linewidth and efficiency of these filters and practical implementation.

In terms of improving the transmission resonance Q factor, we need to fabricate devices with low extinction coefficient and minimal surface roughness. We already proposed to fabricate trapezoidal gratings with SOQ substrate which has crystalline Si with low extinction coefficient. We can have nearly roughness-free sidewalls by applying wet anisotropic etching to fabricate trapezoidal gratings where grating etch direction depends on the crystal plane of Si.

For mass fabrication we can use nanoimprint lithography so that the filters can be produced at a low cost. Implementing transfer printing by kinetic control of adhesion, we can fabricate these devices on SOI wafers and transfer to glass or quartz substrate [79]. As the resonance shape is highly sensitive to the surface roughness, nanoimprint lithography will be a challenging future research direction for these devices.

For the Fabry-Perot based transmission filter, we plan to design structures which can be tuned by the relative polarization of the two mirrors facing each other. So by rotating one device with respect to the other, we can easily tune the resonance position and width of the transmission filter. Analytical calculations are needed to consider the relative phase change on each cycle

Narrow band transmission filters can be used as color filters in display elements. We can tune the pixels thermally by changing the refractive index or by changing different

structural parameters. If we use F-P based transmission filter, tuning can be done by changing the cavity length.

By utilizing the dispersion properties, these elements can be a potential candidate for slow light applications such as optical buffers, delay lines, switches [12]. Fabricating transmission filters with improved linewidth and efficiency we can practically implement these filters in delay elements. Even with our currently fabricated Fabry-Perot based transmission filter which has 3 nm linewidth we can measure the delay and apply in a delay line for further research.

References

[1]   S. S. Wang and R. Magnusson, "Theory and applications of guided-mode resonance filters," Appl. Opt., vol. 32, no. 14, pp. 2606–2613, (1993).

[2]   Z. S. Liu, S. Tibuleac, D. Shin, P. P. Young, and R. Magnusson, "High-efficiency guided-mode resonance filter," Opt. Lett., vol. 23, no. 19, pp. 1556–1558, (1998).

[3]   R. Magnusson, D. Shin, and Z. S. Liu, "Guided-mode resonance Brewster filter," Opt. Lett. , vol. 23, no. 8, pp. 612–614, (1998).

[4]   L. Mashev and E. Popov, "Zero order anomaly of dielectric coated gratings," Opt. Comm. 55, 377-380 (1985).

[5]   E. Popov, L. Mashev, and D. Maystre, "Theoretical study of anomalies of coated dielectric gratings," Opt. Acta 33, 607-619 (1986)

[6]   R. Magnusson and S. S. Wang, "Transmission bandpass guided-mode resonance filters," Appl. Opt., vol. 34, no. 35, pp. 8106–8109, (1995).

[7]   Y. Kanamori, M. Shimono, and K. Hane, "Fabrication of transmission color filter using subwavelength gratings on quartz substrate," IEEE Photon. Technol. Lett., vol. 18, no. 20, pp. 2126–2128, (2006).

[8]   S. Tibuleac and R. Magnusson, "Diffractive narrow-band transmission filters based on guided-mode resonance effects in thin-film multilayers," Photon. Technol. Lett., vol. 9, pp. 464–466, (1997).

[9]   S.Tibuleac, P. P. Young, R. Magnusson, T. R. Holzheimer, "Experimental verification of waveguide-mode resonant transmission filters," *Microwave and Guided Wave Letters, IEEE* , vol.9, no.1, pp.19-21, (1999).

[10]   Kyu J. Lee, James Curzan, Mehrdad Shokooh-Saremi, and Robert Magnusson, "Resonant wideband polarizer with single silicon layer," Applied Physics Letters, vol. 98, no. 21, pp. 211112-1–211112-3, (2011).

[11]   R. Magnusson, D. Wawro, S. Zimmerman, and Y. Ding, "Resonant Photonic Biosensors with Polarization-based Multiparametric Discrimination in Each Channel," Sensors: Special Issue Optical Resonant Sensors, vol. 11, pp. 1476–1488, (2011).

[12]   M. Shokooh-Saremi, R. Magnusson, and X. Wang. "Dispersion engineering with leaky-mode resonant photonic lattices, "Optics Express, vol. 18, no. 1, pp. 108-116, (2010)

[13]   R. W. Wood, "On a remarkable case of uneven distribution of light in a diffraction grating spectrum," Phil. Mag. 4, 396-408 (1902).

[14]   R. W. Wood, "Diffraction gratings with controlled Groove form and abnormal distribution of light intensity," Phil. Mag. 23, 310-317 (1912).

[15]   R. W. Wood, "Anomalous diffraction gratings," Phys. Rev. 48, 928-936 (1935).

[16]   Lord Rayleigh, "On the dynamic theory of gratings," Proc. Roy. Soc. A 79, 399-416 (1907)

[17]   A. Hessel and A. A. Oliner, "A new theory of Wood's anomalies on optical gratings," Appl. Opt. 4, 1275-1299(1965).

[18]   S. S. Wang, R. Magnusson, J. S. Bagby, and M. G. Moharam, "Guided-mode resonances in planar dielectric-layer diffraction gratings," J. Opt. Soc. Am. 7, 1470-1474 (1990).

[19]   M. G. Moharam and T. K. Gaylord, "Rigorous coupled wave analysis of planar grating diffraction," Journal of the Optical Society of America, vol. 71, pp. 811-818, (1981).

[20]   M. Neviere, R. Petit, M. Cadilhac, "About the theory of optical grating coupler-waveguide systems," Optics Communications, Volume 8, Issue 2, Pages 113-117,(1973).

[21]   S. Zhang, "Spatial modifications of Gaussian beams diffracted by reflection gratings," J. Opt. Soc. Am. A, 6(9):1368-1381, Sep., (1989).

[22]   M. Gale, "Diffraction, beauty and commerce," Physics World, pp. 24-28, Oct., (1989).

[23]   M. T Gale,K Knop, R. H Morf., "Zero-order diffractive microstructures for security applications," SPIE, 1210:83-89, (1990).

[24]   S. Mori, K. Mukai, J. Yamakita, and K. Rokushima, "Analysis of dielectric lamellar gratings coated with anisotropic layers," J. Opt. Soc. Am. A 7, 1661-1665 (1990).

[25]   L. F. DeSandre and J. M. Elson, "Extinction-theorem analysis of diffraction anomalies in overcoated gratings," J. Opt. Soc. Am. A 8, 763-777 (1991).

[26]   D. Rosenblatt, A. Sharon, and A. A. Friesem, "Resonant grating waveguide structure," IEEE J. Quant. Electron. 33, 2038-2058 (1997).

[27]   M. T. Gale, K. Knop, R. H. Morf, "Zero-order diffractive microstructures for security applications," Proc. SPIE 1210, Optical Security and Anticounterfeiting Systems, 83 (April 1, 1990).

[28]   K. J. Lee, R. LaComb, B. Britton, M. Shokooh-Saremi, H. Silva, E. Donkor, Y. Ding, and R. Magnusson, "Silicon-layer guided-mode resonance polarizer with 40-nm bandwidth," IEEE Photon. Technol. Lett. 20, 1857-1859 (2008).

89

[29]   R. Magnusson, P. P. Young and D, Shin, "Vertical-cavity laser and laser array incorporating guided-mode resonance effects and methods for making the same," US Patent No. 6154480 (2000).

[30]   R. Magnusson and Y. Ding, "MEMS tunable leaky mode filters," IEEE Photon. Technol. Lett. 18, 1479-1481(2006).

[31]   M. S. Amin, J. W. Yoon and R. Magnusson, "Optical transmission filters with co-existent guided-mode resonance and Rayleigh anomaly," Appl. Phys. Lett. 103, 131106(2013).

[32]   T. Khaleque, H. G. Svavarsson, and R. Magnusson, "Fabrication of resonant pattern using thermal nano-imprint lithography for thin-film photovoltaic applications," Opt. Express 21, A631-A641(2013).

[33]   M. J. Uddin and R. Magnusson, "Highly efficient color filter array using resonant Si3N4 gratings," Opt. Express. 21, 12495 -12506(2013).

[34]   Y. Ding, R. Magnusson, "Doubly resonant single-layer bandpass optical filters." Opt. Lett., 29, 1135–1137 (2004).

[35]   H. Kogelnik, "Coupled wave theory for thick hologram gratings," Bell Syst. Tech. 48, 2909-2947 (1969).

[36]   R. Magnusson and M. Shokooh-Saremi, "Physical basis for wideband resonant reflector," Opt. Express. 16, 3456-3462 (2008).

[37]   M. Shokooh-Saremi and R. Magnusson,"Particle swarm optimization and its application to the design of diffraction grating filters," Optics Letters, 32, pp. 894–896, (2007).

[38]   T. K. Gaylord and M. G. Moharam, "Analysis and applications of optical diffraction by gratings," Proc. IEEE vol. 73, pp. 894-937, (1985).

[39] T. Noguchi, H. Hayashi, T. Ohshima, "Advanced Superthin Polysilicon Film Obtained by Si+ Implantation and Subsequent Annealing," J. Electrochem. Soc. 134, 1771, (1987).

[40] A. Mimura, N. Konishi, K. Ono, J. Ohwada, Y. Hosokawa, Y. A. Ono, T. Suzuki, K. Miyata, H. Kawakami, "High Performance Low-Temperature Poly-Si n-Channel TFT's for LCD," IEEE Trans. Electron Devices 36, 351. (1989).

[41] I-W Wu, A. Chiang, M. Fuse, L. Öveçoglu, and T. Y. Huang, "Retardation of nucleation rate for grain size enhancement by deep silicon ion implantation of low-pressure chemical vapor deposited amorphous silicon films," J. Appl. Phys. 65 , 4036, (1989).

[42] K. L. Chopra, P. D. Paulson, V. Dutta, "Thin-film solar cells: an overview" Progress in photovoltaics: research and applications 12, 69-92, (2004).

[43] R. M. Jin, D. Li, L. Chen, X. Han, J. Lu., "Solid phase crystallization of a-Si by RTA", Appl. Mech. and Mater. 44-47, 4151, (2010).

[44] M. K. Hatalis, D. W. Greve, "Large grain polycrystalline silicon by low-temperature annealing of low-pressure chemical vapor deposited amorphous silicon films," J. Appl. Phys. 63, 2260, (1988).

[45] T. W. Little, K. I. Takahara, H. Koike, T. Nakazawa, I. Yudasaka, H. Ohshima, "Low temperature poly-Si TFT's using solid phase crystallization of very thin films and an electron cyclotron resonance chemical vapor deposition gate insulator," Jpn. J. Appl. Phys. Pt. 1, 38, 3724, (1991).

[46] E. Korin, R. Reif, B. Mikic, "Crystallization of amorphous silicon films using a multistep thermal annealing process," Thin Solid Films 167, 101, (1988).

[47]   Z. Wan, S. Huang, M. A. Green , G. Conibeer, "Rapid thermal annealing and crystallization mechanisms study of silicon nanocrystal in silicon carbide matrix," Nanoscale Res. Lett. 6,129, (2011).

[48]   L. Haji, P. Joubert, J. Stoemenos, N. A. Economou, "Mode of growth and microstructure of polycrystalline silicon obtained by solid-phase crystallization of an amorphous silicon film," J. Appl. Phys. 75 , 3944, (1994).

[49]   D. Girginoudi, S. Girginoudi, A. Thanailakis, N. Georgoulas, "Deposition and crystallization of a-Si thin films by rapid thermal processing,"Thin Solid Films 268, 1. (1995).

[50]   C. W. Lee, C. Lee, Y. T. Kim, "Fast Solid-Phase crystallization of Amorphous Silicon Films on Glass Using Low-Temperature Multi-Step Rapid Thermal Annealing," J. Appl. Phys. A56 ,123-126, (1993).

[51]   A. Szekeres, M. Gartner, F. Vasiliu, M. Marinov, G. Beshkov, "Crystallization of a-Si:H films by rapid thermal annealing," J. Non Cryst. Solids. 227-230 Part 2, 954-957, (1998).

[52]   B. Roy, H. Mahan, Q. Wang, R. Reedy, D.W. Readey, D.S. Ginley, "Monitoring of crystallization and the effect of the deposition rate, hydrogen content and annealing process on the crystallization of hot wire chemical vapor deposited hydrogenated amorphous silicon (a-Si:H) films," Thin Solid Films 516, 6517-6523, (2008).

[53]   M. Modreanu, N. Tomozeiu, Mariuca Gartner, P. Cosmin, "Microstructural and optical properties of as-deposited LPCVD silicon films," Thin Solid Films 383 , 254-257, (2001).

[54] E. Lioudakis, A. Nassiopoulou, A. Othonos, "Ellipsometric analysis of ion-implanted polycrystalline silicon films before and after annealing," Thin Solid Films 496 , 253-258, (2006).

[55] R. M. A. Azzam, N. M. Bashara, Ellipsometry and Polarized Light, North-Holland, New York, (1977).

[56] H. Fujiwara, Spectroscopic Ellipsometry: Principles and Applications,Wiley, Chichester, West Sussex, (2007).

[57] Guide to Using WVASE32™, J.A. Woollam Col., Inc., Lincoln, NE, (1997).

[58] Y. L. Jiang,Y. C. Chang, "Rapid crystallization of a-Si:H films with various silicon-to-hydrogen bonding configurations using rapid energy transfer annealing'" Thin Solid Films 500, 316-321, (2006).

[59] S. Yerci, U. Serincan, I. Dogan, S. Tokay, M. Genisel, A. Aydinli, R. Turan, J. Appl. Phys. 100, 074301, (2006)

[60] F. Schwidefsky, "Increase of the refractive index of silicon films by dangling bonds," Thin Solid Films 18, 45-52, (1973).

[61] M. Shokooh-Saremi and R. Magnusson, "Wideband leaky-mode resonance reflectors: Influence of grating profile and sublayers," Opt. Express 16, 18249-18263 (2008).

[62] Y. Ding and R. Magnusson, "Use of nondegenerate resonant leaky modes to fashion diverse optical spectra" Opt. Express 12, 1885-1891 (2004).

[63] H. Lee, T. Chen. J. Li, , K. Yang, S. Jeon, O. Painter, and K. J. Vahala, "Chemically etched ultrahigh-Q wedge-resonator on a silicon chip", Nature Photonics, 6, pp. 369-373, (2012).

[64] C. H. Chang, R. K. Heilmann, R. C. Fleming., "Fabrication of sawtooth diffraction gratings using nanoimprint lithography," *Journal of Vacuum Science & Technology B: Microelectronics and Nanometer Structures* , vol.21, no.6, pp.2755-2759, Nov 2003.

[65] Z. Yu, L. Chen, W. Wu, H. Ge, S. Y. Chou, "Fabrication of nanoscale gratings with reduced line edge roughness using nanoimprint lithography," *J of Vac. Sci. & Technol. B*, vol.21, no.5, pp.2089-2092, Sep 2003

[66] K. K. Lee, D. R. Lim, L. C. Kimerling, J. Shin, and F. Cerrina, "Fabrication of ultralow-loss Si/SiO$_2$ waveguides by roughness reduction," Opt. Lett. 26, 1888-1890 (2001).

[67] H. Gao, J. M. McMahon, M. H. Lee, J. Henzie,S. K. Gray, G. C. Schatz,T. W. Odom, "Rayleigh anomaly-surface plasmon polariton resonances in palladium and gold subwavelength hole arrays." Opt. Express, 17, 2334–2340 (2009).

[68] T. M. A Rahman, P. Majewski, K. Vasilev, "Extraordinary optical transmission: coupling of the Wood–Rayleigh anomaly and the Fabry–Perot resonance." Opt. Lett., 37, 1742–1744 (2012)

[69] R. Magnusson, "Flat-top resonant reflectors with sharply delimited angular spectra: an application of the Rayleigh anomaly". Opt. Lett., 38, 989–991 (2013).

[70] P. Vincent, M. Neviere, "Corrugated dielectric waveguides: A numerical study of the second-order stop bands." *Appl. Phys., 20,* 345–351 (1979).

[71] C. F. R.Mateus, M. C. Y.Huang, L.Chen, C. J.Chang-Hasnain, and Y.Suzuki, "Broad-band mirror (1.12-1.62 µm) using a subwavelength grating," IEEE Photon. Technol. Lett. 16, 1676-1678 (2004)

[72]   R. Magnusson and M. Shokooh-Saremi, "Physical basis for wideband resonant reflectors," Opt. Express16, 3456-3462 (2008).

[73]   E. Willner, "Lasers: All mirrors are not created equal," Nature Photonics1, 87-88 (2007).

[74]   Yariv and P.Yeh., Photonics: Optical Electronics in Modern Communications, 6th ed. (Oxford University Press, New York, (2007)

[75]   P. Pottier, L. Shi, and Y. A. Peter, "Evolution of modes of Fabry–Perot cavity based on photonic crystal guided-mode resonance mirrors," J. Opt. Soc. Am. B 29, 2698-2703 (2012).

[76]   Y.Lin, C. P. Ho, K. H. Koh, and C. Lee, "Fabry–Perot filter using grating structures," Opt. Lett.38, 902-904 (2013).

[77]   H. Y. Song, S. Kim, and R. Magnusson, "Tunable guided-mode resonances in coupled gratings," Opt. Express 17, 23544-23555 (2009).

[78]   V. Karagodsky, C. Chase, C.J. Chang-Hasnain, Matrix Fabry–Perot resonance mechanism in high-contrast gratings. Opt. Lett. 36(9), 1704–1706 (2011).

[79]   M. A. Meitl, Z.-T. Zhu, V. Kumar, K. J. Lee, X. F., Yonggang Y. Huang, I. Adesida, R. G. Nuzzo, and J. A.. Rogers, "Transfer printing by kinetic control of adhesion to an elastomeric stamp,"Nature Materials, no. 1. pp. 33–38 (2005).

Biographical Information

Mohammad Shyiq Amin completed his Bachelor of Science and Master of Science. in Applied Physics and Electronics from the University of Dhaka, Bangladesh in 2007 and 2008 respectively. In Fall 2009, he started his PhD program at the department of Electrical Engineering in University of Texas at Arlington. He has done several projects throughout his academic career. His undergraduate research was on Analysis of a Hybrid Fiber Radio (HFR) System Using Orthogonal Frequency Division Multiplexing. In his M.Sc. thesis he worked on OFDM: The Emerging Technology for Wireless Communication. His PhD research is based on the design, fabrication and characterization of different kinds of guided-mode resonant transmission filters which can be applicable in color filters, buffers delay line in optical communication etc. During this program he published several peer reviewed journals in Applied Physics Letters, Thin solid films etc. He also attended several conferences, workshops and seminars throughout his academic career. His research interest includes guided-mode resonance devices and their applications, silicon photonics, photonic crystals, optical communication, opto-electronic devices, nano-photonics, non-linear optics, etc. He recently accepted a position as a senior engineer-Yield analysis at Globalfoundries US Inc.